Research Article

Nature and timing of anatectic event of the Hida Belt (Japan): Constraints from titanite geochemistry and U-Pb age of clinopyroxene-bearing leucogranite

Hironobu Harada [a,*], Tatsuki Tsujimori [a,b], Yoshiaki Kon [c], Shogo Aoki [d,e], Kazumasa Aoki [d]

[a] Graduate School of Science, Tohoku University, Sendai 980-8578, Japan
[b] Center for Northeast Asian Studies, Tohoku University, Sendai 980-8576, Japan
[c] Geological Survey of Japan, National Institute of Advanced Industrial Science and Technology, Tsukuba, Ibaraki 305-8567, Japan
[d] Department of Applied Science, Okayama University of Science, Okayama 700-0005, Japan
[e] Graduate School of International Resource Sciences, Akita University, Akita 010-8502, Japan

ARTICLE INFO

ABSTRACT

The Hida Belt, central Japan, is a continental fragment, which was once a part of the crustal basement of the East Asian continental margin. It consists mainly of Permo-Triassic granite-gneiss complexes with both syn-to-late-metamorphic migmatite or granite bodies. Clinopyroxene-bearing leucogranite, locally called as 'Inishi'-type migmatite, occurs characteristically in the migmatite zone associated with amphibolite and marble. The leucogranite is characterized by the presence of coarse-grained diopside–hedenbergite series clinopyroxene and titanite in plagioclase-dominated matrix. Clinopyroxene contains abundant calcite inclusions. Euhedral titanite with high Th/U ratios (~2.8–7.8) and REE contents (~4514–14,069 µg/g) contains polycrystalline 'granitic' inclusions. Those mineralogical features indicate the involvement of carbonate during anatexis. Considering a nominal pressure of 0.4–0.7 GPa of the Hida gneiss, Zr-in-titanite thermometry yields a temperature of 730–810 °C and 770–850 °C at a_{TiO2} = 0.5 and 1, respectively. The titanites show highly variable U/Pb ($^{238}U/^{206}Pb$ = 15.0–24.0) and Pb ($^{207}Pb/^{206}Pb$ = 0.172–0.419) isotope ratios, and the scattered trend follows a discordia line with a lower intercept at 225.4 ± 1.9 Ma. This titanite age would represent the timing of regional anatexis that have occurred in a later stage of the regional metamorphism of the Hida Belt. A high apparent thermal gradient at middle crustal levels might have been caused by regional extension.

1. Introduction

The Hida Belt of central Japan (Fig. 1) is a continental fragment, which was once a part of the crustal basement of the East Asian continental margin prior to the opening of the Japan Sea in Miocene (e.g., Harada et al., 2021; Hiroi, 1981; Isozaki, 1997; Isozaki et al., 2010). The belt consists mainly of Permo-Triassic granite-gneiss complexes with migmatite, marble, calcareous gneiss, amphibolite, granitic gneiss and minor high aluminous pelitic schist (cf. Ehiro et al., 2016). Based on the lithological similarity and its geographical position, it has been postulated as a fragment of the North China Craton, which was affected by a Permo-Triassic regional metamorphism, coeval with a continental collision between the North China and South China cratons (e.g., Ernst et al., 2007; Isozaki, 1997; Isozaki et al., 2010; Oh et al., 2005). However, geological and tectonic correlation among the Hida Belt and

Permo-Triassic collisional orogenic belts in East Asia remains controversial. After the pioneering SHRIMP (Sensitive High-Resolution Ion Microprobe) work by Sano et al. (2000), ion microprobe and LA-ICPMS zircon U-Pb data have been accumulated in the Hida Belt during the last decade (Cho et al., 2021; Horie et al., 2010, 2018; Takahashi et al., 2010, 2018; Takehara and Horie, 2019; Takeuchi et al., 2019; Yamada et al., 2021). Thus far, regional upper amphibolite- to granulite-facies metamorphism and related igneous activity have been dated as ~260–230 Ma.

In the Hida Belt, the regional anatectic event results in the formation of the clinopyroxene-bearing leucogranite in the migmatite zone, locally called as 'Inishi'-type migmatite (e.g., Kano, 1992; Sakoda et al., 2006). The leucogranite generally occurs in association with amphibolite, orthogneiss, calcareous gneiss and marble and often contains xenolith of those rocks (Kano, 1992). Since the leucogranite occurs closely

associated with marble, it is suggested that marble is involved in their formation (Kunugiza et al., 2010). In any case, cross-cutting field relationships between the gneissose rocks and leucogranites indicate that the anatexis has occurred at a later stage of the regional metamorphism. Although SHRIMP zircon U-Pb dating of the leucogranite yields a concordant age of 234.5 ± 2.1 Ma (Sakoda et al., 2006), the zircon U-Pb ages might be inherited from their protolith prior to the regional anatexis. In fact, U-Pb ages of the zircons show a wide range from 266.4 Ma to 225.8 Ma (Sakoda et al., 2006).

In this study, we focus on titanite of the leucogranite to constrain the nature and timing of the regional anatectic event. We describe inclusion mineralogy and trace-element geochemistry of both titanite and clinopyroxene in the leucogranite, and we also present a titanite U-Pb age that represents the timing of the regional anatexis.

2. Geological background

2.1. Tectonic sketch of East Asia

Continental lithosphere of East Asia, located in eastern part of the Eurasian Continent, was formed after the amalgamation of several continental and micro-continental blocks; major cratonic blocks include the North China Craton (NCC) and the South China Craton (SCC). The convergent plate motion beginning in early-Paleozoic generated a continental arc along the margin of the Cathaysia Block of SCC, and the collision between the NCC and SCC generated the Sulu–Dabie orogen, along the paleo-Pacific edge of cratonal Asia. The Sulu–Dabie orogen of East China has received the most intensive investigations as the UHP terrane since early 90s. Blocks, boudins and layers of eclogite and garnet peridotite occur as enclaves in quartzo-feldspathic gneisses. Ubiquitous
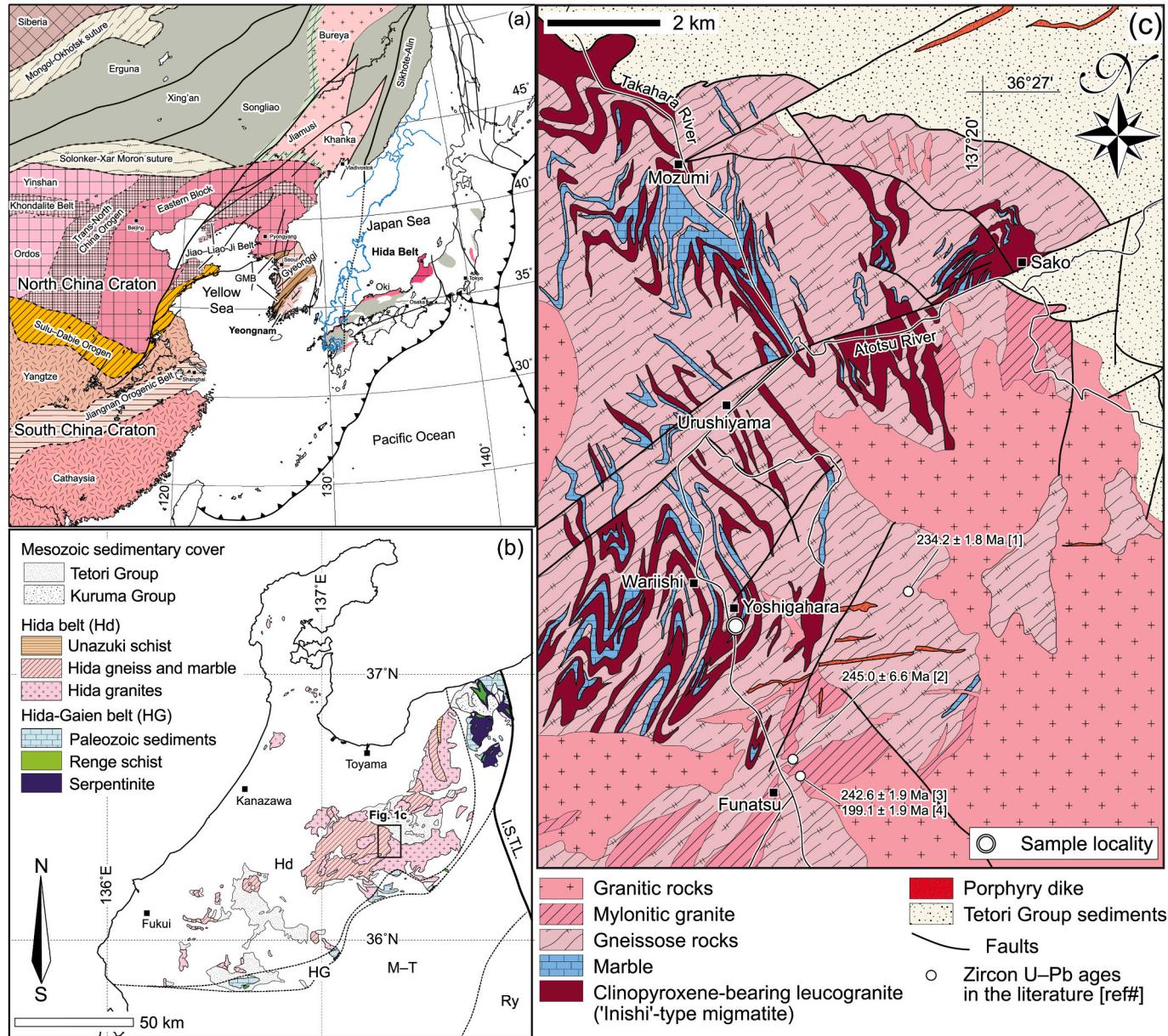
Fig. 1. (a) Tectonic framework of East Asia (modified after Harada et al., 2021). (b) Simplified geological map of the Hokuriku region, showing location of the Kamioka area (modified after Tsujimori, 2002). HG, Hida-Gaien Belt; Hd, Hida Belt; I.S.T.L., Itoigawa–Shizuoka Tectonic Line; M–T, Mino–Tamba Belt; Ry, Ryoke Belt. (c) A geological map of the Kamioka area, showing a sample locality (modified after Harada et al., 2021; Sakurai et al., 1993). Zircon U-Pb ages showing together with references: [1] Clinopyroxene-bearing leucogranite (so-called 'Inishi'-type migmatite) collected from a drill hole of Sakoda et al. (2006), [2] Banded gneiss of Takehara and Horie (2019), [3] Granitic mylonite of Takehara and Horie (2019), and [4] Undeformed granite of Takehara and Horie (2019).

occurrences of coesite inclusions in zircons of felsic gneisses and eclogites indicate that the supracrustal rocks subducted to depths of >100 km (e.g., Liou et al., 2009, 2014). The collisional suture may go to metamorphic complex of the Korean Peninsula (Oh, 2006), which consists of at least three polymetamorphosed Precambrian basement units with Permo-Triassic metamorphic and magmatic records and Barrovian style metamorphic belts (Cho et al., 2007) (Figs. 1 and 2).

It is natural that some geotectonic units of East Asia should connect to the Japanese Islands. The Japanese Islands contain a long active Pacific-type accretionary orogens, that was formed by subduction, oceanward-accretion, and landward-erosion, which began in the early-Paleozoic (e.g., Isozaki, 1997; Isozaki et al., 2010; Pastor-Galán et al., 2021). Pre-Cretaceous geotectonic units of the Japanese Islands have been considered to have grown along the Cathaysia Block of the SCC margin ('Greater South China': e.g., Isozaki, 2019). The Japanese accretionary-related units also correlate to the Far Eastern Russia (e.g., Ishiwatari and Tsujimori, 2003). However, some fragments of 'non-accreted' origin basement rocks exist locally in Japan. The Hida Belt of central Japan is granitic gneiss and granite-dominant low-pressure and high-temperature type metamorphic belt that significantly differs from the other accretionary-related units of Japan (Isozaki, 1997). The gneissose rocks contain abundant ~1.8 Ga magmatic zircons and some Archean zircons (Horie et al., 2010, 2018; Sano et al., 2000). Based on U-Pb ages and Hf isotope compositions of zircons from orthogneiss, Cho et al. (2021) proposed a geotectonic correlation between the Hida Belt and the Yeongnam Massif of the Korean Peninsula.

2.2. Geological setting of the Hida Belt

Major exposures of upper amphibolite- to granulite-facies gneissose rocks of the Hida Belt are located in Kamioka, Odorigawa and Wadagawa areas. Minor pelitic gneiss contains sillimanite, garnet and biotite with very rare staurolite (e.g., Asami and Adachi, 1976; Jin and Ishiwatari, 1997). These gneissose rocks are unconformably covered by the Cretaceous Tetori Group sediments with some clasts derived from the basement (e.g., Sano and Yabe, 2017; Tsujimori, 1995). Geochronological studies revealed that the timing of the regional metamorphic event is ~260–230 Ma (e.g., Cho et al., 2021; Horie et al., 2018; Takahashi et al., 2018).

Granitic rocks (including their metamorphic equivalents) of the Hida Belt have been grouped into two types: older mostly deformed granites of ~260–230 Ma and younger undeformed granites of ~200–180 Ma (Kano, 1990a, 1990b; Takahashi et al., 2010; Yamada et al., 2021). There are two remarkable peaks on the zircon U-Pb concordant age data of igneous and metamorphic rocks from the Hida Belt in the literature (Fig. 2): the Permo-Triassic regional metamorphic event and older granitic activity of ~260–230 Ma, and younger granitic intrusions of ~200–180 Ma.

The Kamioka area (Fig. 1c) is a well-mapped area, where the Pb-Zn ore deposit Kamioka Mine is located. The overall structure shows NS to NE–SW axis fold structure with wavelength of 1–2 km (Kano, 1982; Sohma and Akiyama, 1984). This area consists of granitic and metamorphic rocks such as migmatite, marble, calcareous gneiss and amphibolite. Gneissose and granitic rocks thrust over the Mesozoic Tetori Group sediments at the northern part of the Kamioka area. The eastern and southern parts of the area are mainly composed of granitic rocks. The Funatsu Shear Zone, which consists of mylonitic granite and augen gneiss, is located between the gneissose rocks and granitic rocks (e.g., Kano, 1983; Komatsu et al., 1993). The SHRIMP U-Pb zircon dating of the deformed and undeformed granitic rocks suggests that the mylonitization occurred between 240 Ma and 199 Ma (Takahashi et al., 2010; Takehara and Horie, 2019). The younger granite intruded into the older granite, and a hornfels-like texture of the older granitic rocks at the boundary suggests a contact metamorphism by the younger granitic intrusions (Kano and Watanabe, 1995).

The clinopyroxene-bearing leucogranite occurs characteristically in the migmatite zone and contains coarse-grained clinopyroxene and titanite in a medium to coarse-grained plagioclase-dominated matrix. The leucogranite generally contains amphibolite, orthogneiss, marble and calcareous gneiss xenoliths (Kano, 1992). It is postulated that the leucogranite is formed by the interaction between granitic magma and marble (Kunugiza et al., 2010). The lithology and chemical compositions of the leucogranite are highly heterogeneous; modal compositions of the leucogranite vary from dioritic to granitic or syenitic, mostly dioritic and quartz dioritic compositions (Kano, 1981, 1992). The leucogranite consists mainly of plagioclase, quartz, diopside–hedenbergite series clinopyroxene (Mg# [= Mg/(Mg+Fe)] = 0.40–0.70, mostly 0.50–0.60) and various amount of alkali feldspar, and it characteristically contains coarse-grained titanite (Kano, 1992).

The investigated leucogranite was collected in a river bench of the
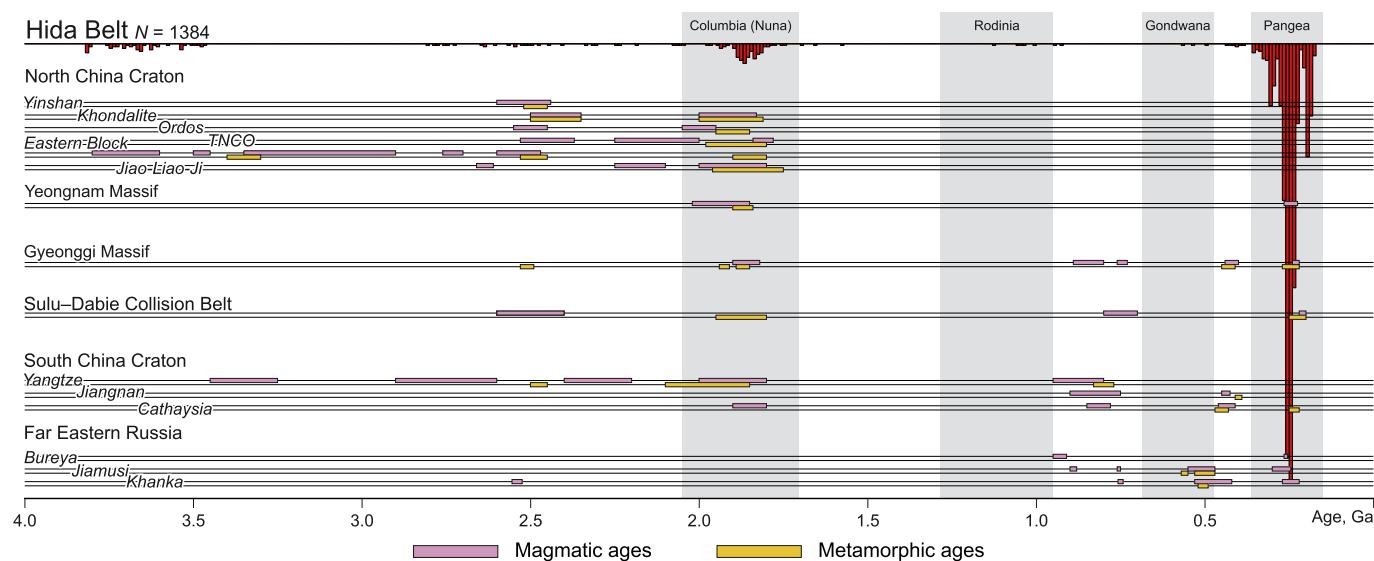
Fig. 2. Summary of geochronological studies of basement rocks of the Hida Belt, North China Craton (Yinshan Block, Ordos Block, Eastern Block, Khondalite Belt, Trans-North China Orogen [TNCO] and Jiao-Liao-Ji Belt), Gyeonggi Massif, Yeongnam Massif, Sulu–Dabie Collision Belt, South China Craton (Yangtze Block, Cathaysia Block and Jiangnan Orogen) and Far Eastern Russia (Bureya, Jiamusi and Khanka terranes). References are shown in Supplementary material 1. A histogram shows SHRIMP and LA-ICPMS U-Pb age data from igneous and metamorphic rocks of the Hida Belt in the literature. Bin width of the histogram is 10 Myr.

Takahara River, Kamioka area, Gifu Prefecture (Fig. 1c). The leucogranite is coarse-grained and contains amphibolite xenoliths (Fig. 3).

3. Petrography and sample description

3.1. Leucogranite

The investigated leucogranite consists mainly of plagioclase (~55 vol%), quartz (~15%), alkali feldspar (~10%), clinopyroxene (~15%), with small amount of titanite (~1%), amphibole and secondary chlorite. Apatite, calcite, prehnite (secondary), allanite, Fe-oxide and Fe-sulfide are accompanied as accessories. Titanite occurs as euhedral crystals up to 1 cm in length (Figs. 3 and 4a,b,d). Titanite crystals contain micrometer-sized polycrystalline 'granitic' inclusions (Fig. 4e,f) which consist of a hypidiomorphic aggregate of quartz, plagioclase, alkali feldspar, epidote, minor allanite, calcite and apatite; chlorite occurs as secondary phase. Clinopyroxene occurs mainly as subhedral to euhedral crystals up to several cm in size (Fig. 4a,c), and it occurs as fine-grained crystals at the contact between the amphibolite xenoliths and leucogranite (Fig. 3c,d). The clinopyroxene contains quartz, plagioclase and titanite inclusions. Very fine-grained mineral inclusions were also identified with a laser Raman spectrometer, HORIBA JOBIN YVON LabRAM300 at Tohoku University, using a 488 nm line of solid-state laser at 25 mW. The Raman analysis found abundant calcite inclusions in clinopyroxene (Fig. 5).

3.2. Amphibolite xenolith

Weakly foliated amphibolite (Fig. 3c) consists mainly of brown amphibole (up to 1.5 mm in size), plagioclase, with small amount of ilmenite and apatite (Fig. 4g). Brown amphibole has tschermakitic and pargasitic compositions with Si = 6.03–6.53 p.f.u. (O = 23), $^{[A]}$(Na+K) = 0.28–0.64 p.f.u. and high K content (0.24–0.32 p.f.u.). Coarse-grained amphibolite (Fig. 3d) consists mainly of coarse-grained brown amphibole (up to 1.5 cm in size), plagioclase, with small amount of ilmenite, magnetite and apatite (Fig. 4h). Brown amphibole has a tschermakitic composition with Si = 6.10–6.26 p.f.u., and it has high Ti content (0.18–0.30 p.f.u.).

4. Trace-element chemistry

In-situ trace elements analysis was carried out with an Agilent 8900cx single-collector quadrupole ICP-MS coupled to a Cyber Laser TiS: femtosecond laser ablation (LA) system at the Geological Survey of Japan. The samples were set in a T201K sample cell of the LA system, and a Shardis static mixer (Y-20A-8E, Younitech Co., Ltd.) was connected between LA system and ICP-MS to stabilize a signal (Kon et al., 2020). The laser ablation was conducted at the condition of wavelength of 260 nm, fluence of 25 J/cm^2 repetition rate of 20 Hz, and ablation time of 20 s. Spot size of an ablation crater was 30 μm by whirlpool rastering of φ10 μm laser probe. On the ICP-MS, 51 nuclides (^{7}Li, ^{23}Na, ^{24}Mg, ^{27}Al, ^{28}Si, ^{31}P, ^{39}K, ^{40}Ca, ^{45}Sc, ^{49}Ti, ^{51}V, ^{52}Cr, ^{55}Mn, ^{56}Fe, ^{59}Co, ^{60}Ni, ^{63}Cu, ^{66}Zn, ^{69}Ga, ^{85}Rb, ^{88}Sr, ^{89}Y, ^{90}Zr, ^{93}Nb, ^{133}Cs, ^{137}Ba, ^{139}La, ^{140}Ce, ^{141}Pr, ^{146}Nd, ^{147}Sm, ^{151}Eu, ^{153}Eu, ^{157}Gd, ^{159}Tb, ^{163}Dy, ^{165}Ho, ^{166}Er, ^{169}Tm, ^{172}Yb, ^{175}Lu, ^{178}Hf, ^{181}Ta, ^{182}W, ^{204}Pb, ^{205}Tl, ^{206}Pb, ^{207}Pb, ^{208}Pb, ^{232}Th, and ^{238}U) were analyzed by H$_2$ reaction mode. The NIST SRM 610 and BCR-2G were analyzed as calibration standards for correcting sensitivity factors (Jochum et al., 2011; Jochum and Nohl,
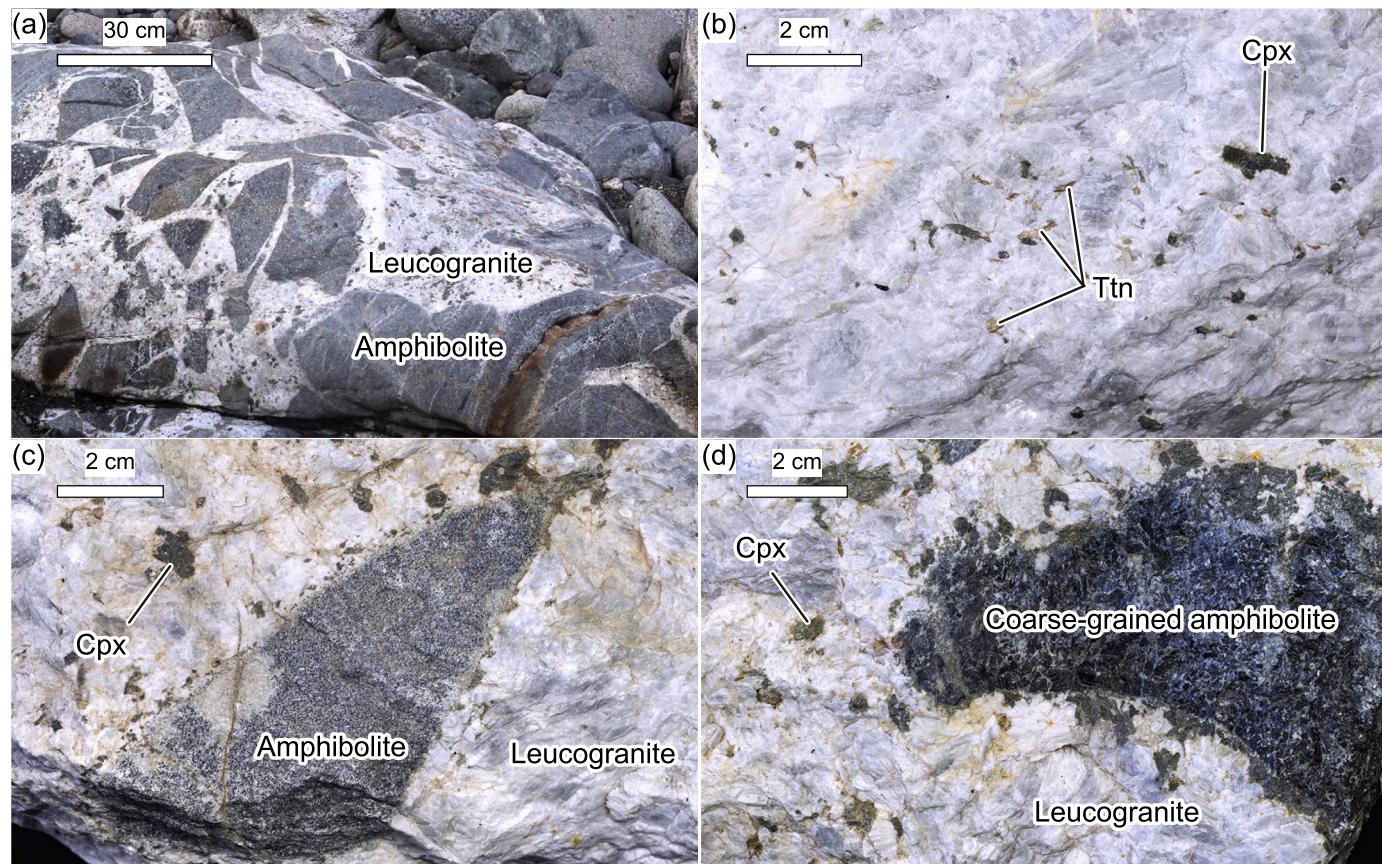
Fig. 3. (a) A photograph showing field view of the migmatite zone in the Kamioka area of the Hida Belt. The clinopyroxene-bearing leucogranite contains amphibolite xenoliths. (b) A typical appearance of the leucogranite. containing coarse-grained clinopyroxene (Cpx) and titanite (Ttn). (c) Weakly foliated amphibolite xenolith in the leucogranite. (d) Coarse-grained amphibolite xenolith in the leucogranite. Abundant greenish clinopyroxene crystals occur near the boundary of two lithologies.
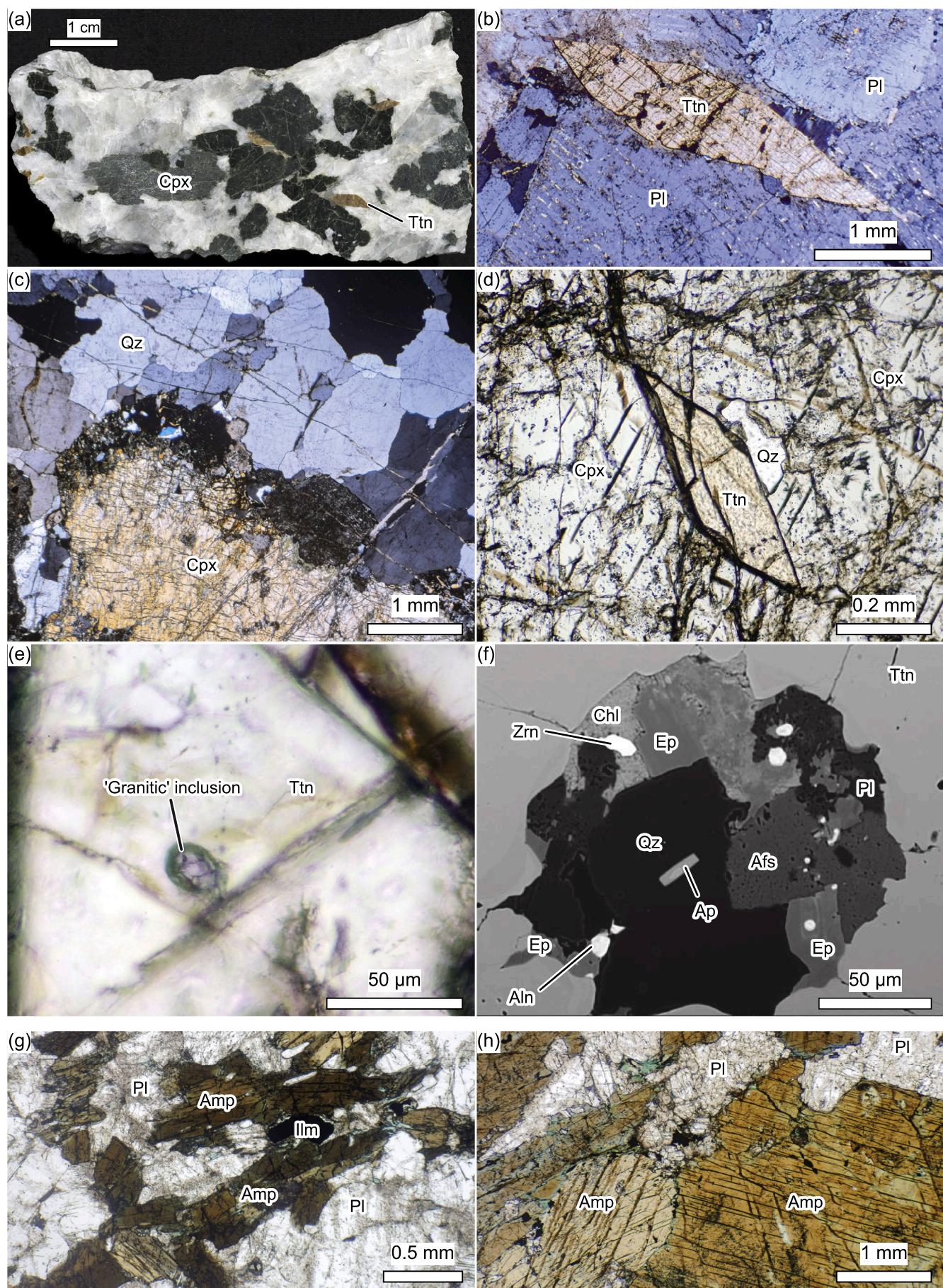
(caption on next page)

Fig. 4. (a) A photograph showing an appearance of studied leucogranite (so-called 'Inishi'-type migmatite). The leucogranite contains coarse-grained clinopyroxene and titanite. (b) Crossed-polarized image (XPL) of coarse-grained euhedral titanite in the leucogranite. (c) XPL image of the leucogranite. (d) Plane–polarized light (PPL) image of titanite in the leucogranite. (e) PPL image of a polycrystalline 'granitic' inclusion in titanite. (f) Back-scattered electron (BSE) image of polycrystalline 'granitic' inclusion in titanite. (g) PPL image of weakly foliated amphibolite xenolith in leucogranite. (h) XPL image of coarse-grained amphibolite xenolith in leucogranite. This amphibolite is characterized by the presence of coarse-grained brown amphibole (up to 1.5 cm in size). Mineral abbreviations: Afs—alkali feldspar, Aln—allanite, Amp—amphibole, Ap—apatite, Chl—chlorite, Cpx—clinopyroxene, Ep—epidote, Ilm—ilmenite, Pl—plagioclase, Qz—quartz, Ttn—titanite, Zrn—zircon. (For interpretation of the references to colour in this figure legend, the reader is referred to the web version of this article.)

2008).

The major and trace element data of the 83 analyzed spots of two titanite crystals, 23 spots of two clinopyroxene crystals, 20 spots of two plagioclase crystals and 20 spots of one alkali feldspar crystal in the leucogranite are shown in Fig. 6a-d and Supplementary Table 1.

Titanite contains ~43–107 µg/g Sr, ~369–1440 µg/g Y, ~26–145 µg/g Th, ~8–27 µg/g U, < ~8 µg/g Pb, ~352–954 µg/g Nb, ~19–60 µg/g Ta and ~537–1130 µg/g Zr. It shows high Th/U ratios (~2.8–7.8). Total REE concentrations (~4514–14,069 µg/g) are two or three orders of magnitude larger than those of clinopyroxene (~6–45 µg/g). Trace element abundances vary one order of magnitude within a grain. Most trace elements do not show clear systematic core-to-rim profiles, whereas HREE is slightly enriched at the rim. The CI-chondrite-normalized REE patterns of titanite (Fig. 6a) show enrichment in LREE with smooth depletion of HREE and negative Eu anomaly.

Clinopyroxene (Mg# = 0.41–0.48) contains ~25–48 µg/g Sr, ~2–8 µg/g Y, ~4–19 µg/g Zr and < ~12.5 µg/g Pb. It has LREE-enriched and flat HREE patterns with negative Eu anomaly (Fig. 6b). Compared to trace element compositions of clinopyroxenes with a similar Mg# from the high-fractionated, plagioclase-clinopyroxene cumulates of the Skaergaard Intrusion (Namur and Humphreys, 2018), clinopyroxenes from our leucogranite are characterized by low REE and high Sr concentrations.

Plagioclase (An$_{27-35}$) has ~1170–1470 µg/g Sr, ~12–659 µg/g Ba, ~0.3–4 µg/g Ce, ~0.2–0.8 µg/g Eu and ~4–18 µg/g Pb. It tends to show lower REE rather than that of similar plagioclase (An$_{\sim 30}$) in the

Skaergaard plagioclase-clinopyroxene cumulates (Namur and Humphreys, 2018). Alkali feldspar contains ~267–299 µg/g Rb, ~891–1270 µg/g Sr, ~5–8 µg/g Cs, ~3150–4370 µg/g Ba, ~0.2–0.8 µg/g Eu and ~ 33–47 µg/g Pb.

5. Titanite U-Pb dating

In-situ titanite U-Pb dating was carried out with a Thermo Fisher Scientific iCAP-RQ single-collector quadrupole coupled to a Teledyne Cetac Technologies Analyte G2 ArF excimer LA system at the Okayama University of Science. The samples were set in a two-volume HelEx2 sample cell of the LA system. The laser ablation was conducted at the condition of laser spot size of 65 µm, fluence of 5 J/cm^2 and repetition rate of 10 Hz. On the ICP-MS, 5 nuclides (^{202}Hg, ^{204}Pb, ^{206}Pb, ^{207}Pb and ^{238}U) were analyzed. The BLR-1 titanite (Aleinikoff et al., 2007) was analyzed as a calibration standard for correcting mass bias of Pb/U ratios, and NIST SRM 612 was analyzed for Pb/Pb isotopic ratios. All uncertainties are quoted at a 2-sigma level to which repeatability of measurements of primary standards are propagated based on quadratic addition. Further details of our titanite U-Pb analysis method are given in Aoki and Aoki (2020). The MKED-1 (Spandler et al., 2016) was analyzed as the secondary standard with the unknown titanites. Weighted mean ^{207}Pb-^{206}Pb, ^{238}U-^{206}Pb and ^{235}U-^{207}Pb ages with 2σ uncertainties of 1523.2 ± 3.3 Ma (MSWD = 1.1), 1523.0 ± 13 Ma (MSWD = 0.11) and 1522.9 ± 7.6 Ma (MSWD = 0.14) were obtained from the MKED-1 (n = 9), which are consistent with the reference ^{207}Pb-^{206}Pb, ^{238}U-^{206}Pb and ^{235}U-^{207}Pb ages of 1521.02 ± 0.55 Ma, 1518.87 ± 0.31 Ma and 1517.32 ± 0.32 Ma by the ID-TIMS (Spandler et al., 2016).

Seventy-four U-Pb analyses were performed on 5 titanite grains. The results of titanite U-Pb data are shown in Table 1 and plotted on a Tera–Wasserburg concordia diagram (Fig. 7). Titanite typically contains a relatively large amount of common lead, but provided there is a sufficient spread in the proportion of radiogenic to common Pb, the lower intercept of the discordia line determines a crystallization age, which is equivalent to a common Pb correction. Analyzed titanites show highly variable ^{238}U/^{206}Pb ratio (15.0–24.0) and ^{207}Pb/^{206}Pb ratio (0.172–0.419). Seventy-four spot isotope analyses define a discordia in the concordia diagram, yielding a lower intercept age of 225.4 ± 1.9 Ma (MSWD = 3, n = 74). Although the MSWD value is high, individual calculations for each sample show low values; MSWD for lower intercept ages of grain-1 (223.9 ± 7.8 Ma), grain-2 (232.4 ± 14.0 Ma), grain-3 (225.3 ± 4.7 Ma), and grain-4 (231.6 ± 4.1 Ma) are 1.9 (n = 15), 1.3 (n = 14), 1.9 (n = 15), 2.3 (n = 15) and 1.6 (n = 15), respectively.

6. Discussion

6.1. Origin of leucogranite

It has been known that amphibolite melting can generate silicic melt to form leucosomes (e.g., Brophy, 2008; Pu et al., 2014). As shown in the geological map (Fig. 1c), the distribution of clinopyroxene-bearing leucogranite is closely associated with marble. Although the investigated leucogranite does not contain xenoliths of marble, the presence of abundant calcite inclusions in clinopyroxene supports carbonate-involved dehydration melting of amphibolite.

As described above, the euhedral shape of titanite crystals and the presence of polycrystalline 'granitic' inclusions (Fig. 4e,f) indicate that
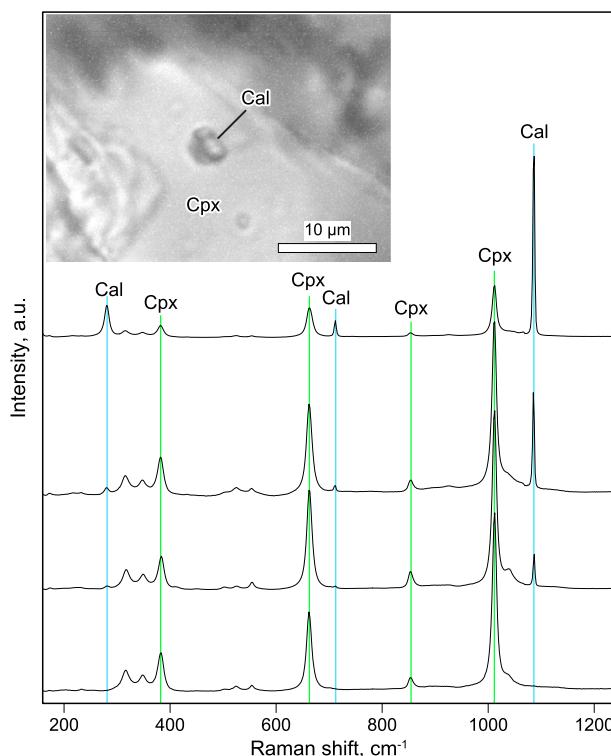
Fig. 5. Optical image of a calcite inclusion in clinopyroxene and Raman spectra of calcite (Cal) inclusions in clinopyroxene (Cpx). A spectrum of host clinopyroxene is also shown for comparison.
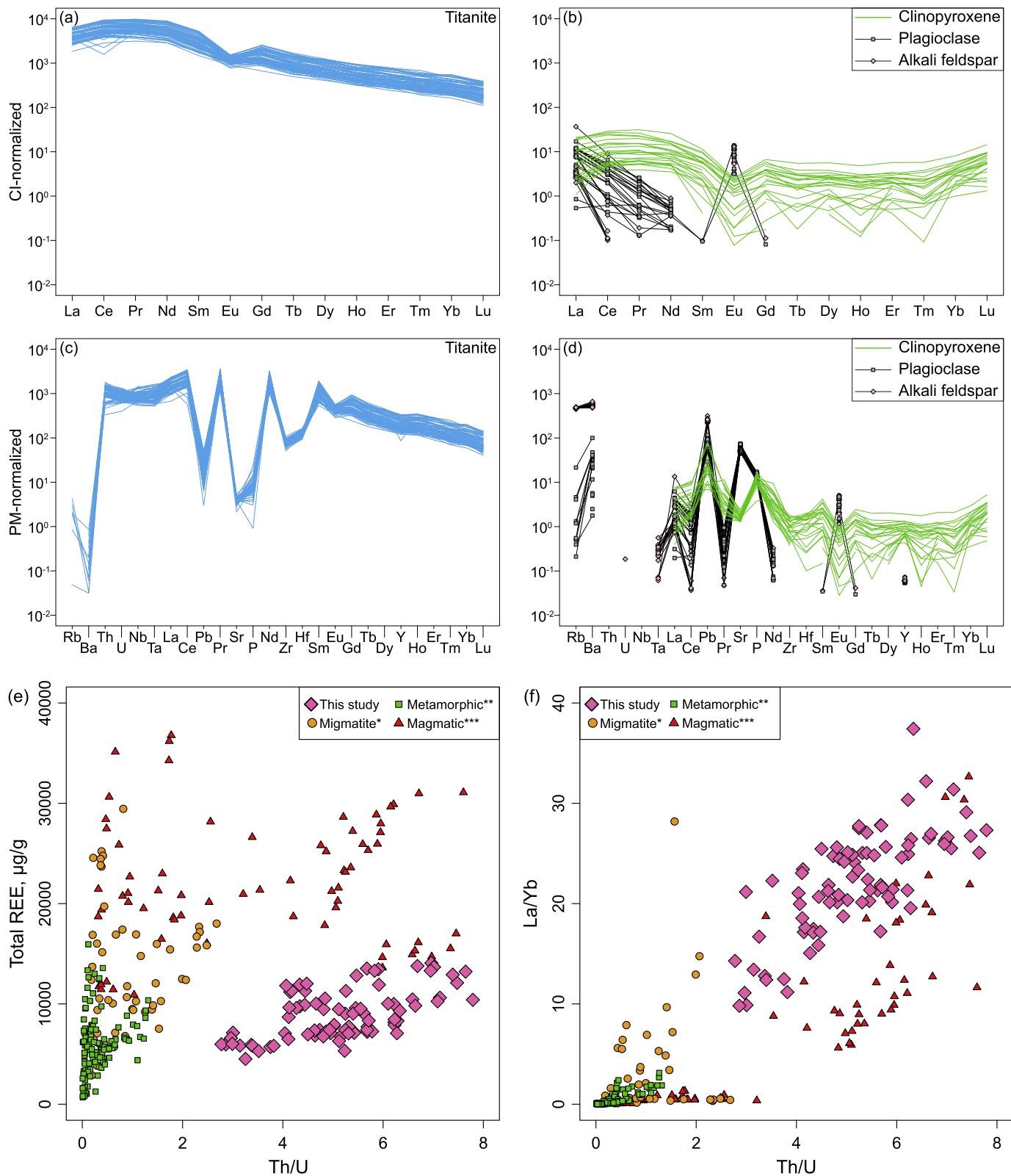
Fig. 6. (a)–(d) CI-chondrite normalized REEs and Primitive Mantle (PM)-normalized trace elements abundances of titanite and clinopyroxene in the leucogranite. (a) REE patterns of titanite. (b) REE patterns of clinopyroxene, plagioclase and alkali feldspar. (c) Trace element patterns of titanite. (d) Trace element patterns of clinopyroxene, plagioclase and alkali feldspar. Both normalization factors are from McDonough and Sun (1995). (e) (f) Trace element characteristics of the analyzed titanites. (e) The Th/U vs. total REE content (μg/g) plot. (f) The Th/U vs. La/Yb plot. Migmatite*—titanite crystalized from anatectic melt (Chen et al., 2016; Chen and Zheng, 2015). Metamorphic**—metamorphic titanite (Chen et al., 2013, 2016; Chen and Zheng, 2015; Gao et al., 2012). Magmatic***—magmatic titanite (Chen et al., 2013; Fu et al., 2018; Gao et al., 2012; Li et al., 2010).

Table 1
LA-ICPMS titanite U-Pb isotope data of titanite from the leucogranite (so-called 'Inishi'-type migmatite) of the Hida Belt.

| Spot ID	$^{207}Pb/^{235}U$	2σ	$^{206}Pb/^{238}U$	2σ	$^{207}Pb/^{206}Pb$	2σ	$^{235}U/^{207}Pb$ age	2σ	$^{238}U/^{206}Pb$ age	2σ	$^{207}Pb/^{206}Pb$ age	2σ
1-2-1	1.16	0.0402	0.0430	0.00140	0.195	0.00239	779.9	18.9	271.7	8.7	2782.4	20.1
1-2-2	1.39	0.0484	0.0451	0.00147	0.224	0.00275	885.5	20.6	284.3	9.1	3009.0	19.7
1-2-3	1.19	0.0413	0.0439	0.00143	0.197	0.00240	795.4	19.2	276.7	8.8	2798.1	20.0
1-2-5	1.30	0.0462	0.0457	0.00149	0.207	0.00285	846.9	20.4	287.8	9.2	2881.7	22.4
1-2-6	1.38	0.0491	0.0454	0.00148	0.221	0.00307	881.8	20.9	286.0	9.1	2988.9	22.3
1-2-7	1.04	0.0361	0.0422	0.00137	0.179	0.00216	724.3	18.0	266.2	8.5	2644.4	20.0
1-2-8	1.29	0.0460	0.0435	0.00142	0.215	0.00306	842.1	20.4	274.5	8.8	2946.1	22.9
1-2-9	1.37	0.0492	0.0461	0.00151	0.215	0.00317	876.3	21.1	290.8	9.3	2946.4	23.8
1-2-10	1.58	0.0564	0.0457	0.00150	0.250	0.00359	961.8	22.2	288.4	9.2	3186.5	22.7
1-2-11	1.38	0.0485	0.0450	0.00147	0.223	0.00290	880.8	20.7	283.5	9.0	3000.6	20.9
1-2-12	1.73	0.0613	0.0479	0.00157	0.262	0.00358	1019.4	22.8	301.4	9.6	3258.9	21.5
1-2-13	1.57	0.0555	0.0466	0.00152	0.244	0.00331	957.9	21.9	293.7	9.4	3146.9	21.6
1-2-14	1.30	0.0463	0.0445	0.00146	0.212	0.00298	846.2	20.4	281.0	9.0	2919.6	22.8
1-2-15	1.52	0.0539	0.0470	0.00154	0.235	0.00320	939.2	21.7	296.0	9.5	3085.5	21.7
1-3-1	1.28	0.0423	0.0447	0.00137	0.207	0.00253	836.1	18.8	281.9	8.5	2885.2	19.8
1-3-2	1.27	0.0418	0.0444	0.00136	0.207	0.00250	831.2	18.7	279.9	8.4	2883.2	19.6
1-3-3	1.90	0.0618	0.0493	0.00151	0.279	0.00306	1079.9	21.7	310.1	9.3	3358.2	17.1
1-3-4	1.52	0.0509	0.0476	0.00147	0.232	0.00301	938.7	20.5	299.6	9.0	3064.4	20.8
1-3-5	1.55	0.0507	0.0469	0.00144	0.240	0.00270	950.9	20.2	295.5	8.9	3119.0	17.9
1-3-6	1.60	0.0524	0.0475	0.00146	0.245	0.00275	970.7	20.4	299.0	9.0	3150.3	17.9
1-3-7	1.67	0.0547	0.0482	0.00148	0.251	0.00288	995.8	20.8	303.2	9.1	3190.7	18.1
1-3-8	3.86	0.124	0.0668	0.00205	0.419	0.00396	1606.1	25.9	417.1	12.4	3979.5	14.1
1-3-9	1.50	0.0493	0.0455	0.00140	0.239	0.00278	930.6	20.0	286.9	8.6	3114.2	18.5
1-3-10	1.11	0.0369	0.0417	0.00128	0.194	0.00242	759.0	17.7	263.2	7.9	2772.2	20.5
1-3-11	1.27	0.0425	0.0448	0.00138	0.205	0.00273	830.4	19.0	282.3	8.5	2866.8	21.7
1-3-12	1.28	0.0428	0.0443	0.00137	0.209	0.00277	835.2	19.1	279.4	8.4	2897.6	21.5
1-3-13	1.24	0.0420	0.0442	0.00136	0.204	0.00283	819.4	19.0	278.8	8.4	2855.4	22.6
1-3-14	2.13	0.0709	0.0504	0.00156	0.306	0.00380	1158.3	23.0	317.2	9.6	3501.9	19.2
1-3-15	1.65	0.0552	0.0484	0.00149	0.247	0.00323	988.3	21.2	304.5	9.2	3165.0	20.8
1-1-1	1.12	0.0252	0.0422	0.00077	0.193	0.00253	764.9	12.0	266.3	4.7	2770.3	21.5
1-1-2	1.29	0.0285	0.0437	0.00079	0.215	0.00268	842.5	12.6	275.6	4.9	2940.9	20.2
1-1-3	1.10	0.0246	0.0431	0.00078	0.186	0.00241	755.4	11.9	272.3	4.8	2703.9	21.4
1-1-4	1.12	0.0248	0.0427	0.00077	0.191	0.00241	765.2	11.9	269.5	4.8	2751.4	20.7
1-1-5	1.19	0.0263	0.0432	0.00078	0.199	0.00253	795.2	12.2	272.8	4.8	2821.3	20.7
1-1-6	1.18	0.0263	0.0433	0.00079	0.198	0.00252	793.5	12.2	273.5	4.9	2811.9	20.8
1-1-7	1.22	0.0273	0.0436	0.00079	0.203	0.00263	810.3	12.5	275.4	4.9	2849.7	21.1
1-1-8	1.28	0.0283	0.0437	0.00079	0.213	0.00267	837.9	12.6	275.8	4.9	2926.6	20.3
1-1-9	1.67	0.0366	0.0477	0.00087	0.254	0.00310	997.2	13.9	300.1	5.3	3210.6	19.3
1-1-10	1.25	0.0270	0.0434	0.00078	0.209	0.00250	822.3	12.2	273.6	4.8	2895.3	19.4
1-1-11	1.57	0.0343	0.0466	0.00085	0.245	0.00296	958.6	13.5	293.5	5.2	3149.5	19.2
1-1-12	1.19	0.0266	0.0431	0.00078	0.200	0.00261	796.8	12.3	272.2	4.8	2829.9	21.2
1-1-13	1.34	0.0300	0.0450	0.00082	0.217	0.00279	864.7	13.0	283.6	5.1	2955.9	20.8
1-1-14	1.15	0.0272	0.0439	0.00081	0.190	0.00282	778.4	12.8	277.2	5.0	2744.0	24.4
1-1-15	1.30	0.0293	0.0443	0.00081	0.212	0.00282	843.8	12.9	279.5	5.0	2921.5	21.5
1-4-1	1.53	0.0396	0.0463	0.00109	0.240	0.00255	942.8	15.9	292.0	6.7	3117.2	16.9
1-4-2	1.18	0.0310	0.0438	0.00103	0.195	0.00228	790.8	14.5	276.1	6.4	2788.1	19.1
1-4-3	1.17	0.0320	0.0447	0.00106	0.191	0.00257	788.0	15.0	281.6	6.5	2746.5	22.2
1-4-4	1.16	0.0314	0.0441	0.00105	0.191	0.00248	783.2	14.7	278.4	6.5	2751.1	21.3
1-4-5	1.17	0.0317	0.0439	0.00104	0.192	0.00255	784.5	14.8	277.1	6.4	2763.0	21.7
1-4-6	1.01	0.0265	0.0423	0.00100	0.172	0.00205	706.6	13.4	267.3	6.2	2579.7	19.8
1-4-7	1.18	0.0312	0.0447	0.00106	0.192	0.00226	792.1	14.5	282.2	6.5	2755.5	19.4
1-4-8	1.20	0.0327	0.0457	0.00108	0.191	0.00253	801.5	15.1	288.0	6.7	2748.8	21.8
1-4-9	1.36	0.0360	0.0469	0.00111	0.210	0.00253	871.3	15.5	295.3	6.8	2907.1	19.5
1-4-10	1.35	0.0349	0.0456	0.00107	0.214	0.00232	866.3	15.1	287.6	6.6	2937.3	17.5
1-4-11	3.03	0.0763	0.0603	0.00142	0.365	0.00327	1416.3	19.2	377.4	8.6	3770.6	13.6
1-4-12	1.60	0.0413	0.0485	0.00114	0.240	0.00251	971.0	16.1	305.4	7.0	3117.0	16.7
1-4-13	1.63	0.0434	0.0489	0.00116	0.242	0.00291	983.3	16.7	307.7	7.1	3135.7	19.1
1-4-14	1.34	0.0364	0.0461	0.00109	0.210	0.00279	861.6	15.8	290.3	6.7	2908.8	21.5
1-4-15	1.36	0.0368	0.0464	0.00110	0.213	0.00276	872.8	15.8	292.6	6.8	2926.7	20.9
1-5-1	1.35	0.0385	0.0456	0.00121	0.214	0.00228	865.9	16.7	287.6	7.5	2936.0	17.2
1-5-2	1.49	0.0425	0.0464	0.00123	0.234	0.00237	928.0	17.3	292.4	7.6	3076.3	16.2
1-5-3	1.52	0.0435	0.0476	0.00127	0.232	0.00245	939.0	17.5	300.1	7.8	3062.8	16.9
1-5-4	1.21	0.0346	0.0439	0.00117	0.199	0.00219	802.9	16.0	276.7	7.2	2820.4	17.9
1-5-5	1.42	0.0407	0.0459	0.00122	0.225	0.00238	897.8	17.1	289.1	7.5	3014.9	17.0
1-5-6	1.29	0.0370	0.0447	0.00119	0.209	0.00230	840.2	16.4	281.7	7.3	2898.4	17.8
1-5-7	1.24	0.0367	0.0448	0.00120	0.201	0.00252	820.3	16.6	282.6	7.4	2835.8	20.4
1-5-8	1.30	0.0384	0.0455	0.00122	0.207	0.00262	844.5	17.0	287.0	7.5	2879.3	20.6
1-5-9	1.22	0.0362	0.0446	0.00119	0.198	0.00258	808.5	16.6	281.5	7.4	2807.6	21.3
1-5-10	1.25	0.0362	0.0444	0.00118	0.204	0.00231	823.7	16.3	279.9	7.3	2861.8	18.4
1-5-11	1.48	0.0425	0.0461	0.00123	0.233	0.00251	921.6	17.4	290.4	7.6	3070.7	17.3
1-5-12	1.77	0.0504	0.0489	0.00130	0.263	0.00262	1036.0	18.4	308.0	8.0	3264.0	15.7
1-5-13	1.33	0.0383	0.0439	0.00117	0.220	0.00241	859.6	16.7	277.0	7.2	2980.7	17.6
1-5-14	2.16	0.0606	0.0532	0.00141	0.294	0.00272	1167.4	19.5	334.3	8.6	3438.8	14.3
1-5-15	3.44	0.0952	0.0631	0.00167	0.395	0.00313	1513.8	21.8	394.5	10.1	3891.7	11.9
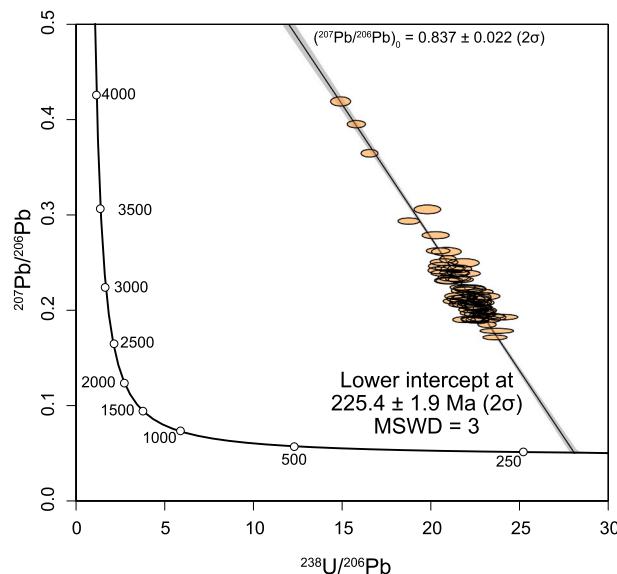
Fig. 7. Tera–Wasserburg concordia diagram showing all titanite U-Pb data. Seventy-four U-Pb isotope analyses define a discordia in the concordia diagram, yielding a lower intercept age of 225.4 ± 1.9 Ma. Data plotting and age calculation were performed using IsoplotR (Vermeesch, 2018).

titanites in the clinopyroxene-bearing leucogranite crystalized from the anatectic melt. The origins of titanite are also distinguished by trace element features. In general, magmatic titanite is characterized commonly by high REE content and Th/U values compared to metamorphic titanite (e.g., Aleinikoff et al., 2002; Gao et al., 2012; Li et al., 2010). By using these features, Chen and Zheng (2015) and Chen et al. (2016) distinguished the anatectic domain from the metamorphic domain, and they showed the anatectic titanite which had grown from hydrous melts showed similar characteristics to the magmatic titanite. Our titanite data show high Th/U ratios (~2.8–7.8), and this feature strongly suggests a melt involved crystallization. Although the REE contents of analyzed titanites overlap to some of the metamorphic titanites found in the literature, they can be distinguished from metamorphic titanite in a Th/U vs. total REE plot (Fig. 6e). The titanites in the leucogranite can be also distinguished from the metamorphic titanite based on their La/Yb ratios (Fig. 6f). In conclusion, trace element compositions of investigated titanites support the crystallization from the anatectic melt.

Polycrystalline 'granitic' inclusions in analyzed titanites contain epidote. In general, the occurrence of magmatic epidote depends on the oxygen fugacity and the chemical compositions of melt (e.g., Schmidt and Thompson, 1996). It is also suggested that magmatic epidote in granitic melt systems tends to have formed at moderate pressure (~0.5–0.8 GPa) conditions (e.g., Masumoto et al., 2014; Naney, 1983; Zen and Hammarstrom, 1984). The presence of epidote in the 'granitic' inclusions in titanite crystals is consistent with the anatexis at mid-crustal conditions.

Using experimentally determined trace-element partition coefficients between silicate melt and titanite and/or diopside, the compositions of the anatectic melt can be estimated. According to Prowatke and Klemme (2005), partitioning of some elements (Nb, Ta, Th, U and REE) depends highly on the compositions of silicate melt, especially the alumina saturation index (ASI: molar ratio $Al_2O_3/(Na_2O + K_2O + CaO)$). Since the leucogranite contains abundant plagioclase, it should have high ASI value (ASI > 0.5: Kano, 1992). Thus, we applied silicate melt–titanite partitioning data for five different melt compositions of Prowatke and Klemme (2005) (ASI > 0.5). In addition, we applied silicate melt–diopside partition coefficients for Na_2O bearing anorthite–diopside–titanite system (Schosnig and Hoffer, 1998). Estimated melt compositions are shown in Fig. 8. Notably the Sr concentrations
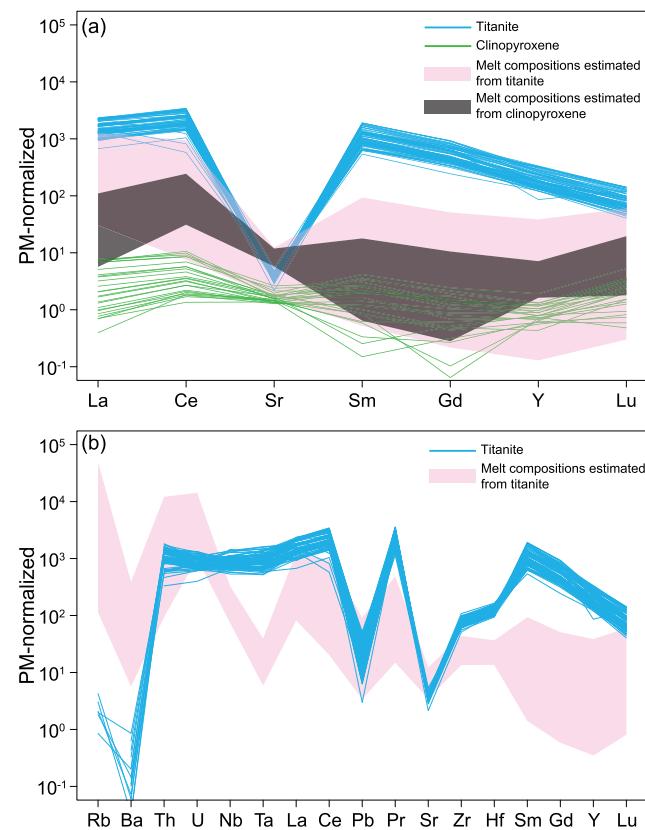

Fig. 8. (a) PM-normalized trace element patterns for titanite and clinopyroxene in the clinopyroxene-bearing leucogranite and inferred melt compositions estimated from titanite (pink domain) and diopside (gray domain). Melt compositions are calculated using silicate melt–diopside partition coefficients for Na_2O bearing anorthite–diopside–titanite system (Schosnig and Hoffer, 1998) and silicate melt–titanite partition coefficients for five different melt compositions of ASI [molar ratio $Al_2O_3/(Na_2O + K_2O + CaO)$] = 0.59*, 0.64, 0.76 and 0.77 (Prowatke and Klemme, 2005). (b) PM-normalized trace element patterns for titanite in the leucogranite and possible titanite-forming melt. Melt compositions are calculated using silicate melt–titanite partitioning data for ASI = 0.59*, 0.64, 0.76 and 0.77 (Prowatke and Klemme, 2005). "*" represents two partition coefficient data. (For interpretation of the references to colour in this figure legend, the reader is referred to the web version of this article.)

estimated from both titanite and diopside overlap with each other. Compared to silicic melt generated by amphibolite melting (Pu et al., 2014), estimated melt compositions are high REE contents, especially LREE. Moreover, the inferred melt compositions are characterized by high U and Th content and Nb/Ta ratio (Fig. 8b). These trace element features of the estimated melt may reflect the involvement of carbonate during anatexis.

6.2. Condition of crustal anatexsis

We estimated the crystallization temperature of titanite using the Zr-in-titanite thermometry (Hayden et al., 2008). The thermometry requires the coexistence of quartz, rutile and zircon. Since rutile was not observed in the leucogranite, the TiO_2 activity cannot be regarded as 1. However, it was suggested that the plausible lower limits of the TiO_2 activity in most igneous and metamorphic rocks is about 0.5 (e.g., Ferry and Watson, 2007; Hayden and Watson, 2007). The pressure condition of the regional metamorphism on the Hida Belt is poorly constrained. The occurrence of the minor pelitic gneiss which contains sillimanite, garnet and biotite with very rare staurolite (Asami and Adachi, 1976) can constrain the stability condition of sillimanite and staurolite. A peak pressure condition of ~0.4–0.7 GPa summarized by Suzuki et al. (1989)
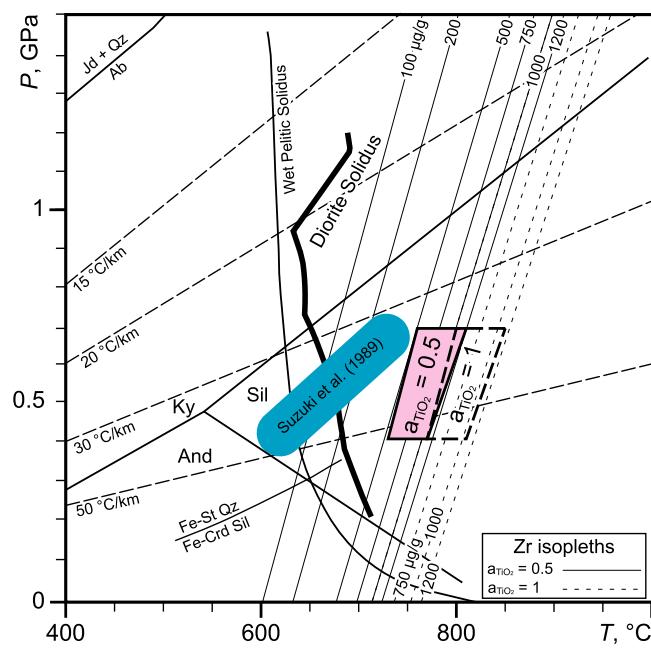
Fig. 9. A pressuretemperature diagram showing estimated titanite formation temperatures and metamorphic condition of the Hida Belt in the literature (Suzuki et al., 1989). This figure also shows titanite isopleths as a function of both temperature and pressure calculated using the experimental calibration of Hayden et al. (2008). The titanite formation temperatures were estimated using Zr-in-titanite thermometry (Hayden et al., 2008) and calculated the TiO$_2$ activity for 0.5 and 1 at nominal pressure conditions of 0.4–0.7 GPa. Wet pelitic solidus, diorite solidus and low-pressure limit of Fe-staurolite are after Thompson (1982), Palin et al. (2016) and Richardson (1968), respectively.

seems to be reasonable and has been widely accepted as a nominal pressure of the regional metamorphism of the Hida Belt. Considering these, we calculated the TiO$_2$ activity for 0.5 and 1 at nominal pressure conditions of 0.4–0.7 GPa. Estimated temperature for a$_{TiO_2}$ = 0.5 and 1 are 730–810 °C and 770–850 °C, respectively (Fig. 9, Supplementary Table 2). Such high temperature crystallization is compatible with the titanite growth from anatectic melt.

6.3. Timing of the anatectic event in the Hida Belt

The U-Pb closure temperature of titanite is still unknown though different studies suggest the temperatures always over 600 °C (e.g., Gao et al., 2012; Scott and St-Onge, 1995; Spear and Parrish, 1996). For example, Scott and St-Onge (1995) suggested > ~680 °C based on the titanite growth temperature. On the other hand, Gao et al. (2012) suggested > ~800 °C from titanite samples which survived 800–850 °C metamorphism. Recent studies rather prefer such a high U-Pb closure temperature of > 830 °C (Hartnady et al., 2019; Kirkland et al., 2020). Even if U-Pb closure temperature of titanite is relatively low, our titanite crystals are large (3–5 mm in length), thus it is unlikely that coarse-grained titanite were influenced by intercrystalline Pb diffusion. Assuming the high closure temperature of titanite, titanite U-Pb age of 225.4 ± 1.9 Ma obtained from this study can be regarded as the timing of formation of the leucogranite, i.e., timing of the regional anatectic event.

Available zircon data suggest that the regional metamorphic event and coeval granitic activity of the Hida Belt was ~260–230 Ma (e.g., Cho et al., 2021; Horie et al., 2018; Sano et al., 2000; Takahashi et al., 2018). Our titanite U-Pb age corresponds to the ending time of an inferred regional metamorphic period of the Hida Belt (~260–230 Ma) (Fig. 10). In other words, the leucogranite-forming anatectic event might have occurred in a later stage of the regional metamorphism of the Hida Belt. However, this anatectic event can be clearly distinguished from the
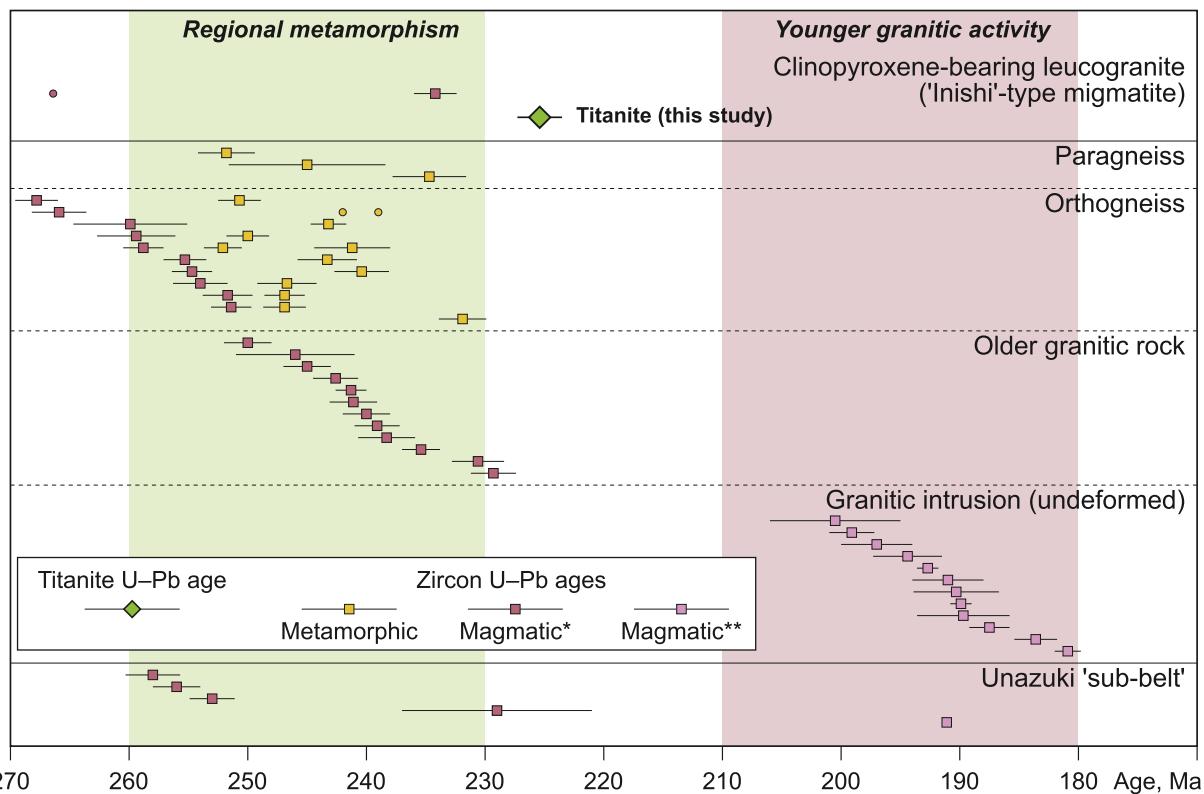
Fig. 10. Summary of geochronological studies in the Hida Belt. Magmatic*—magmatic zircons ages including inherited core, detrital grains and unclear interpretation; Magmatic**—zircon ages of younger granite. References are shown in Supplementary material 1.

intrusion of younger granitic intrusions (~200–180 Ma). Considering new titanite U-Pb age of ~225 Ma and estimated titanite formation temperature of >700 °C at mid-crustal condition, the Hida Belt would have been at a high geothermal gradient in a later stage of the regional metamorphic activity of the Hida Belt. Such a high apparent geothermal gradient may be explained by a regional extension with the high heat flow from the upwelling of asthenospheric mantle (e.g., Sandiford and Powell, 1986; Wickham and Oxburgh, 1985; Zheng and Chen, 2017).

In the regional geotectonic context, it is reasonable to consider that all tectonic events recorded in the Hida Belt connect to its tectonic counterpart of East Asian margin (Fig. 1a). The 225 Ma anatectic event at a high geothermal gradient possibly due to regional extension can be a new key to correlate the Hida Belt to potential western counterparts in the Korean Peninsula. Nevertheless, to further our understanding of the geological correlation of the East Asia continental margin, a more detailed and comprehensive approach is required than that documented in previous studies.

Declaration of Competing Interest

The authors declare that they have no known competing financial interests or personal relationships that could have appeared to influence the work reported in this paper.

Appendix A. Supplementary data

Supplementary data to this article can be found online at https://doi.org/10.1016/j.lithos.2021.106256.

References

Aleinikoff, J.N., Wintsch, R.P., Fannng, C.M., Dorais, M.J., 2002. U-Pb geochronology of zircon and polygenetic titanite from the Glastonbury complex, Connecticut, USA: an integrated SEM, EMPA, TIMS, and SHRIMP study. Chem. Geol. 188, 125–147.

Aleinikoff, J.N., Wintsch, R.P., Tollo, R.P., Unruh, D.M., Fanning, C.M., Schmitz, M.D., 2007. Ages and origins of rocks of the Killingworth dome, south-Central Connecticut: implications for the tectonic evolution of southern New England. Am. J. Sci. 307, 63–118.

Aoki, S., Aoki, K., 2020. In-situ U-Pb age determination of titanite by LA-ICP-MS. Naturalistae 24, 7–12.

Asami, M., Adachi, M., 1976. Staurolite-bearing cordierite-sillimanite gneiss from the Toga area in the Hida metamorphic terrane, Central Japan. J. Geol. Soc. Jpn. 82, 259–271.

Brophy, J.G., 2008. A study of rare earth element (REE)–SiO₂ variations in felsic liquids generated by basalt fractionation and amphibolite melting: a potential test for discriminating between the two different processes. Contrib. Mineral. Petrol. 156, 337–357.

Chen, Y.X., Zheng, Y.F., 2015. Extreme Nb/Ta fractionation in metamorphic titanite from ultrahigh-pressure metagranite. Geochim. Cosmochim. Acta 150, 53–73.

Chen, Y.X., Zheng, Y.F., Hu, Z., 2013. Polyphase growth of accessory minerals during continental collision: geochemical evidence from ultrahigh-pressure metamorphic gneisses in the Sulu orogen. Lithos 177, 245–267.

Chen, Y.X., Zhou, K., Zheng, Y.F., Gao, X.Y., Yang, Y.H., 2016. Polygenetic titanite records the composition of metamorphic fluids during the exhumation of ultrahigh-pressure metagranite in the Sulu orogen. J. Metamorph. Geol. 34, 573–594.

Cho, D.L., Lee, T.H., Takahashi, Y., Kato, T., Yi, K., Lee, S., Cheong, A.C.S., 2021. Zircon U-Pb geochronology and Hf isotope geochemistry of magmatic and metamorphic rocks from the Hida Belt, Southwest Japan. Geosci. Front. 12, 101145.

Cho, M., Kim, Y., Ahn, J., 2007. Metamorphic evolution of the Imjingang belt, Korea: Implications for Permo-Triassic collisional orogeny. Int. Geol. Rev. 49, 30–51.

Ehiro, M., Tsujimori, T., Tsukada, K., Nuramkhaan, M., 2016. Paleozoic basement and associated cover. In: Moreno, T., Wallis, S., Kojima, T., Gibbons, W. (Eds.), The Geology of Japan. Geological Society of London, pp. 25–60.

Ernst, W.G., Tsujimori, T., Zhang, R., Liou, J.G., 2007. Permo-Triassic collision, subduction-zone metamorphism, and tectonic exhumation along the East Asian continental margin. Annu. Rev. Earth Planet. Sci. 35, 73–110.

Ferry, J.M., Watson, E.B., 2007. New thermodynamic models and revised calibrations for the Ti-in-zircon and Zr-in-rutile thermometers. Contrib. Mineral. Petrol. 154, 429–437.

Fu, Y., Sun, X., Hollings, P., Li, D., Yang, T., 2018. Geochronology and trace element geochemistry of titanite in the Machangqing Cu-Mo-dominated polymetallic deposit, Yunnan Province, Southwest China. J. Asian Earth Sci. 158, 398–414.

Gao, X.Y., Zheng, Y.F., Chen, Y.X., Guo, J., 2012. Geochemical and U-Pb age constraints on the occurrence of polygenetic titanites in UHP metagranite in the Dabie orogen. Lithos 136, 93–108.

Harada, H., Tsujimori, T., Kunugiza, K., Yamashita, K., Aoki, S., Aoki, K., Takayanagi, H., Iryu, Y., 2021. The δ¹³C–δ¹⁸O variations in marble in the Hida Belt, Japan. Island Arc 30, e12389.

Hartnady, M.I., Kirkland, C.L., Clark, C., Spaggiari, C.V., Smithies, R.H., Evans, N.J., McDonald, B.J., 2019. Titanite dates crystallization: Slow Pb diffusion during super-solidus re-equilibration. J. Metamorph. Geol. 37, 823–838.

Hayden, L.A., Watson, E.B., 2007. Rutile saturation in hydrous siliceous melts and its bearing on Ti-thermometry of quartz and zircon. Earth Planet. Sci. Lett. 258, 561–568.

Hayden, L.A., Watson, E.B., Wark, D.A., 2008. A thermobarometer for sphene (titanite). Contrib. Mineral. Petrol. 155, 529–540.

Hiroi, Y., 1981. Subdivision of the Hida metamorphic complex, Central Japan, and its bearing on the geology of the Far East in pre-Sea of Japan time. Tectonophysics 76, 317–333.

Horie, K., Yamashita, M., Hayasaka, Y., Katoh, Y., Tsutsumi, Y., Katsube, A., Hidaka, H., Kim, H., Cho, M., 2010. Eoarchean–Paleoproterozoic zircon inheritance in Japanese Permo-Triassic granites (Unazuki area, Hida Metamorphic complex): Unearthing more old crust and identifying source terrnaes. Precambrian Res. 183, 145–157.

Horie, K., Tsutsumi, Y., Takehara, M., Hidaka, H., 2018. Timing and duration of regional metamorphism in the Kagasawa and Unazuki areas, Hida metamorphic complex, Southwest Japan. Chem. Geol. 484, 148–167.

Ishiwatari, A., Tsujimori, T., 2003. Paleozoic ophiolites and blueschists in Japan and Russian Primorye in the tectonic framework of East Asia: a synthesis. Island Arc 12, 190–206.

Isozaki, Y., 1997. Contrasting two types of orogen in Permo-Triassic Japan: accretionary versus collisional. Island Arc 6, 2–24.

Isozaki, Y., 2019. A visage of early Paleozoic Japan: Geotectonic and paleobiogeographical significance of Greater South China. Island Arc 28, e12296.

Isozaki, Y., Aoki, K., Nakama, T., Yanai, S., 2010. New insight into a subduction-related orogen: a reappraisal of the geotectonic framework and evolution of the Japanese Islands. Gondwana Res. 18, 82–105.

Jin, F., Ishiwatari, A., 1997. Petrological and geochemical study on Hida gneisses in the upper reach area of Tetori river: comparative study on the pelitic metamorphic rocks with the other areas of Hida belt, Sino-Korean block and Yangtze block. J. Mineral. Petrol. Econ. Geol. 92, 213–230 (in Japanese with English abstract).

Jochum, K.P., Nohl, U., 2008. Reference materials in geochemistry and environmental research and the GeoReM database. Chem. Geol. 253, 50–53.

Jochum, K.P., Weis, U., Stoll, B., Kuzmin, D., Yang, Q., Raczek, I., Jacob, D.E., Stracke, A., Birbaum, K., Frick, D.A., Günther, D., Enzweiler, J., 2011. Determination of reference values for NIST SRM 610–617 glasses following ISO guidelines. Geostand. Geoanal. Res. 35, 397–429.

Kano, T., 1981. Migmatite structure of the Hida metamorphic region, central Japan. J. Geol. Soc. Jpn. 87, 315–328 (in Japanese with English abstract).

Kano, T., 1982. Tectonic divisions and their development of the Hida metamorphic region, central Japan. Mem. Geol. Soc. Jpn. 21, 9–24 (in Japanese with English abstract).

Kano, T., 1983. Origin of augen gneisses and related mylonitic rocks in the eastern part of the Hida metamorphic region, central Japan. (part 1): mode of occurrences, petrographical and mineralogical properties of rocks and potash-feldspar megacrysts. J. Geol. Soc. Jpn. 89, 375–393 (in Japanese with English abstract).

Kano, T., 1990a. Intrusive relation of the Okumayama Granitic Mass (Shimonomoto type) into the Iori Granitic Mass (Funatsu type) in the Hayatsukigawa area: re-examination of the sub-division for early Mesozoic granites (Funatsu Granites) in the Hida region. J. Geol. Soc. Jpn. 96, 379–388 (in Japanese with English abstract).

Kano, T., 1990b. Granitic rocks in the Hida complex, central Japan. Min. Geol. 40, 397–413 (in Japanese with English abstract).

Kano, T., 1992. Compositional variation of clinopyroxenes in so-called Inishi migmatitie and skarn ore (Mokuji Ore) in and around the Kamioka mining area, Japan. Min. Geol. 42, 379–390.

Kano, T., Watanabe, T., 1995. Geology and structure of the early Mesozoic granitoids in the east of the Kamioka mining area, southern Hida metamorphic region, central Japan. J. Geol. Soc. Jpn. 101, 499–514 (in Japanese with English abstract).

Kirkland, C.L., Yakymchuk, C., Gardiner, N.J., Szilas, K., Hollis, J., Olierook, H., Steenfelt, A., 2020. Titanite petrochronology linked to phase equilibrium modelling constrains tectono-thermal events in the Akia Terrane, West Greenland. Chem. Geol. 536, 119467.

Komatsu, M., Nagase, M., Naito, K., Kanno, T., Ujihara, M., Toyoshima, T., 1993. Structure and tectonics of the Hida massif, central Japan. Mem. Geol. Soc. Jpn. 42, 39–62 (in Japanese with English abstract).

Kon, Y., Yokoyama, T.D., Ohata, M., 2020. Analytical efficacy of gas-mixer and stabilizer for laser ablation-ICP mass spectrometry. ASC Omega 5, 28073–28079.

Kunugiza, K., Shimizu, M., Otoh, S., 2010. U–Th–Pb chronological constraints on the geotectonic history of Central Japan from the Hida metamorphism through the opening of Japan to the present. J. Geol. Soc. Jpn. 116 (Supplement), 83–101 (in Japanese).

Li, J.W., Deng, X.D., Zhou, M.F., Liu, Y.S., Zhao, X.F., Guo, J.L., 2010. Laser ablation ICP-MS titanite U-Th-Pb dating of hydrothermal ore deposits: a case study of the Tonglushan Cu-Fe-Au skarn deposit, SE Hubei Province, China. Chem. Geol. 270, 56–67.

Liou, J.G., Ernst, W.G., Zhang, R.Y., Tsujimori, T., Jahn, B.M., 2009. Ultrahigh-pressure minerals and metamorphic terranes–the view from China. J. Asian Earth Sci. 35, 199–231.

Liou, J.G., Tsujimori, T., Yang, J., Zhang, R.Y., Ernst, W.G., 2014. Recycling of crustal materials through study of ultrahigh-pressure minerals in collisional orogens, ophiolites, and mantle xenoliths: a review. J. Asian Earth Sci. 96, 386–420.

Masumoto, Y., Enami, M., Tsuboi, M., Hong, M., 2014. Magmatic zoisite and epidote in tonalite of the Ryoke belt, central Japan. Eur. J. Mineral. 26, 279–291.

McDonough, W.F., Sun, S.S., 1995. The composition of the Earth. Chem. Geol. 120, 223–253.

Namur, O., Humphreys, M.C.S., 2018. Trace element constraints on the differentiation and crystal mush solidification in the Skaergaard intrusion, Greenland. J. Petrol. 59 (3), 387–418.

Naney, M.T., 1983. Phase equilibria of rock-forming ferromagnesian silicates in granitic systems. Am. J. Sci. 283, 993–1033.

Oh, C.W., 2006. A new concept on tectonic correlation between Korea, China and Japan: histories from the late Proterozoic to cretaceous. Gondwana Res. 9, 47–61.

Oh, C.W., Kim, S.W., Choi, S.G., Zhai, M., Guo, J., Krishnan, S., 2005. First finding of eclogite facies metamorphic event in South Korea and its correlation with the Dabie-Sulu collision belt in China. J. Geol. 113, 226–232.

Palin, R.M., White, R.W., Green, E.C., Diener, J.F., Powell, R., Holland, T.J., 2016. High-grade metamorphism and partial melting of basic and intermediate rocks. J. Metamorph. Geol. 34, 871–892.

Pastor-Galán, D., Spencer, C.J., Furukawa, T., Tsujimori, T., 2021. Evidence for crustal removal, tectonic erosion and flare-ups from the Japanese evolving forearc sediment provenance. Earth Planet. Sci. Lett. 564, 116893.

Prowatke, S., Klemme, S., 2005. Effect of melt composition on the partitioning of trace elements between titanite and silicate melt. Geochim. Cosmochim. Acta 69, 695–709.

Pu, X., Brophy, J.G., Tsujimori, T., 2014. Rare earth element–SiO$_2$ systematics of island arc crustal amphibolite migmatites from the Asago body of the Yakuno Ophiolite, Japan: a field evaluation of some model predictions. Contrib. Mineral. Petrol. 168, 1060.

Richardson, S.W., 1968. Staurolite stability in a part of the system Fe-Al-Si-OH. J. Petrol. 9, 467–488.

Sakoda, M., Kano, T., Fanning, C.M., Sakaguchi, T., 2006. SHRIMP U-Pb zircon age of the Inishi migmatite around the Kamioka mining area, Hida metamorphic complex, Central Japan. Resour. Geol. 56, 17–26.

Sakurai, W., Okada, Y., Mizuyachi, O., 1993. On the exploration of the Atotsugawa district in the Kamioka mining area, central Japan. Resour. Geol. 43, 79–91 (in Japanese with English abstract).

Sandiford, M., Powell, R., 1986. Deep crustal metamorphism during continental extension: modern and ancient examples. Earth Planet. Sci. Lett. 79, 151–158.

Sano, S.I., Yabe, A., 2017. Fauna and flora of early cretaceous Tetori Group in Central Japan: the clues to revealing the evolution of cretaceous terrestrial ecosystem in East Asia. Palaeoworld 26, 253–267.

Sano, Y., Hidaka, H., Terada, K., Shimizu, H., Suzuki, M., 2000. Ion microprobe U-Pb zircon geochronology of the Hida gneiss: finding of the oldest minerals in Japan. Geochem. J. 34, 135–153.

Schmidt, M.W., Thompson, A.B., 1996. Epidote in calc-alkaline magmas: an experimental study of stability, phase relationships, and the role of epidote in magmatic evolution. Am. Mineral. 81, 462–474.

Schosnig, M., Hoffer, E., 1998. Compositional dependence of REE partitioning between diopside and melt at 1 atmosphere. Contrib. Mineral. Petrol. 133, 205–216.

Scott, D.J., St-Onge, M.R., 1995. Constraints on Pb closure temperature in titanite based on rocks from the Ungava orogen, Canada: implications for U-Pb geochronology and P-T-t path determinations. Geology 23, 1123–1126.

Sohma, T., Akiyama, S., 1984. Geological structure and lithofacies in the central part of the Hida metamorphic belt. J. Geol. Soc. Jpn. 90, 609–628 (in Japanese with English abstract).

Spandler, C., Hammerli, J., Sha, P., Hilbert-Wolf, H., Hu, Y., Roberts, E., Schmitz, M., 2016. MKED1: a new titanite standard for *in situ* analysis of Sm-Nd isotopes and U-Pb geochronology. Chem. Geol. 425, 110–126.

Spear, F.S., Parrish, R.R., 1996. Petrology and cooling rates of the Valhalla complex, British Columbia, Canada. J. Petrol. 37, 733–765.

Suzuki, M., Nakazawa, S., Osakabe, T., 1989. Tectonic development of the Hida Belt –with special reference to its metamorphic history and late Carboniferous to Triassic orogenies. Mem. Geol. Soc. Jpn. 33, 1–10 (in Japanese with English abstract).

Takahashi, Y., Cho, D.L., Kee, W.S., 2010. Timing of mylonitization in the Funatsu shear zone within Hida Belt of Southwest Japan: Implications for correlation with the shear zones around the Ogcheon Belt in the Korean Peninsula. Gondwana Res. 17, 102–115.

Takahashi, Y., Cho, D.L., Mao, J., Zhao, X., Yi, K., 2018. SHRIMP U-Pb zircon ages of the Hida metamorphic and plutonic rocks, Japan: Implications for late Paleozoic to Mesozoic tectonics around the Korean Peninsula. Island Arc 27, e12220.

Takehara, M., Horie, K., 2019. U-Pb zircon geochronology of the Hida gneiss and granites in the Kamioka area, Hida Belt. Island Arc 28, e12303.

Takeuchi, M., Shibata, K., Jia, S., Yamamoto, K., 2019. U-Pb zircon ages of granitic rocks from Kagasawa, Hida Mountains. J. Geol. Soc. Jpn. 125, 453–459 (in Japanese with English abstract).

Thompson, A.B., 1982. Dehydration melting of pelitic rocks and the generation of H$_2$O-undersaturated granitic liquids. Am. J. Sci. 282, 1567–1595.

Tsujimori, T., 1995. Staurolite-bearing sillimanite schist cobble from the Upper Jurassic Tetori Group in the Kuzuryu area, Hida Mountains, central Japan. J. Geol. Soc. Jpn. 101, 971–977.

Tsujimori, T., 2002. Prograde and retrograde P-T paths of the late Paleozoic glaucophane eclogite from the Renge metamorphic belt, Hida Mountains, southwestern Japan. Int. Geol. Rev. 44, 797–818.

Vermeesch, P., 2018. IsoplotR: a free and open toolbox for geochronology. Geosci. Front. 9, 1479–1493.

Wickham, S.M., Oxburgh, E.R., 1985. Continental rifts as a setting for regional metamorphism. Nature 318, 330–333.

Yamada, R., Sawada, H., Aoyama, S., Ouchi, W., Niki, S., Nagata, M., Takahashi, T., Hirata, T., 2021. Zircon U-Pb ages and whole–rock geochemistry from the Hida granites: implications for the geotectonic history and the origin of Mesozoic granites in the Hida belt, Japan. J. Mineral. Petrol. Sci. 116, 61–66.

Zen, E.A., Hammarstrom, J.M., 1984. Magmatic epidote and its petrologic significance. Geology 12, 515–518.

Zheng, Y.F., Chen, R.X., 2017. Regional metamorphism at extreme conditions: Implications for orogeny at convergent plate margins. J. Asian Earth Sci. 145, 46–73.

Table S1: Major and trace element compositions of titanite. Oxides are in wt%, trace elements are in μg/g.

	TtnA-01	TtnA-03	TtnA-04	TtnA-05	TtnA-06	TtnA-07	TtnA-08	TtnA-09	TtnA-10	TtnA-11	TtnA-12	TtnA-13	TtnA-14	TtnA-15	TtnA-16	TtnA-18
SiO_2	29.44	29.59	30.04	29.29	29.21	29.63	29.16	29.34	29.26	29.55	28.90	29.52	28.76	29.71	29.16	28.90
TiO_2	37.61	37.79	38.05	38.44	38.46	38.12	38.23	38.18	37.49	37.38	38.38	38.62	38.33	37.43	38.61	38.57
Al_2O_3	2.13	2.31	2.04	1.87	1.88	2.05	2.51	2.32	2.24	2.46	2.15	2.07	2.01	2.09	1.85	1.83
FeO	0.58	0.53	0.48	0.52	0.55	0.57	0.43	0.56	0.68	0.70	0.63	0.65	0.58	0.59	0.51	0.78
MnO	0.04	0.04	0.04	0.03	0.04	0.04	0.03	0.04	0.04	0.04	0.04	0.04	0.04	0.04	0.04	0.04
MgO	0.01	0.04	0.01	0.01	0.01	0.00	0.01	0.01	0.01	0.01	0.01	0.01	0.01	0.01	0.01	0.08
CaO	28.02	28.39	27.68	28.16	28.29	28.22	28.49	28.24	28.90	28.57	28.36	27.57	28.81	28.66	28.22	27.92
Na_2O	0.01	0.01	0.01	0.02	0.00	—	0.02	—	0.01	—	0.01	—	0.01	—	0.02	0.01
K_2O	0.00	0.01	—	0.00	—	—	—	0.01	0.00	—	—	0.00	0.00	—	—	0.01
P_2O_5	0.16	0.16	0.13	0.12	0.17	0.16	0.28	0.17	0.17	0.14	0.30	0.21	0.18	0.23	0.17	0.13
Li	—	—	—	—	—	—	—	—	—	—	—	—	—	—	—	—
Sc	—	—	6.59	5.04	4.04	—	6.43	19.5	12.9	—	16.3	18.3	—	—	6.06	4.53
V	209	210	318	277	226	212	255	290	227	247	226	239	251	241	218	231
Cr	1.94	1.90	11.9	12.9	17.1	—	4.63	11.0	—	—	—	—	—	—	7.01	—
Co	—	—	—	—	—	—	—	0.272	—	—	—	—	—	—	—	0.121
Ni	—	—	—	—	—	—	—	—	—	—	—	—	—	—	—	0.299
Cu	—	—	—	—	—	250	—	38.4	254	—	186	449	—	—	—	1360
Zn	17.9	2.03	—	13.0	23.3	—	16.0	—	71.6	3.41	—	—	—	—	—	—
Ga	3.96	3.83	3.61	2.41	3.04	3.78	3.11	3.45	3.44	4.21	2.28	3.39	3.64	3.52	4.18	2.86
Rb	1.31	0.511	—	0.852	—	5.63	—	—	—	2.68	—	—	—	3.77	—	1.18
Sr	72.1	73.9	79.7	79.3	85.8	83.4	65.5	88.1	78.1	73.5	75.7	79.2	78.3	75.2	73.5	84.0
Y	1290	558	1080	1040	770	565	521	640	586	563	574	598	634	629	704	736
Zr	656	940	674	639	645	808	821	832	678	781	772	799	720	790	816	686
Nb	531	648	451	478	474	588	449	382	476	352	494	541	519	475	618	534
Cs	0.815	0.0909	0.192	1.05	0.978	0.712	—	—	—	—	—	—	1.61	0.871	—	0.651
Ba	—	1.32	0.736	—	—	—	—	—	—	—	—	—	—	—	—	—
La	1380	885	1090	1100	1000	899	435	772	852	834	881	926	942	968	1060	1130
Ce	5350	3080	4010	4060	3620	2950	1750	2800	3090	3040	3190	3290	3420	3280	3850	4350
Pr	864	417	627	617	585	499	292	447	464	457	471	488	526	509	582	673
Nd	3940	1650	2550	2740	2560	2080	1310	1900	1950	1910	1990	2110	2280	2170	2460	3030
Sm	770	285	533	513	501	337	268	345	310	341	345	361	391	380	421	536
Eu	84.2	43.8	75.9	72.1	73.7	60.1	55.1	62.7	61.1	59.9	57.0	57.0	65.6	59.7	65.5	77.7
Gd	505	179	374	333	321	207	184	222	220	207	217	223	249	236	270	317
Tb	60.5	20.5	44.5	43.7	34.9	22.8	21.4	26.2	24.9	24.7	24.8	26.0	27.8	24.1	30.6	36.1
Dy	307	113	248	220	178	132	105	142	127	124	117	131	140	138	156	172
Ho	48.3	18.8	39.9	36.7	29.3	21.0	17.2	22.2	19.9	20.2	18.8	21.1	22.9	20.3	24.2	26.8
Er	118	48.5	88.1	90.5	74.2	43.0	45.2	57.0	51.9	51.1	50.6	53.0	52.9	54.8	62.6	62.6
Tm	12.8	5.56	12.4	10.5	10.6	6.06	4.75	5.96	5.33	5.43	6.24	5.52	6.34	5.65	7.45	6.99
Yb	79.9	36.7	62.5	69.1	46.9	33.2	26.1	35.3	30.6	37.3	35.6	37.0	31.0	38.8	38.6	34.9
Lu	8.76	4.28	8.00	7.43	5.64	2.96	2.73	4.48	3.52	3.59	4.28	4.23	4.15	4.43	4.90	3.88
Hf	33.6	42.0	33.6	27.3	28.4	33.8	31.4	36.6	30.1	37.2	35.8	36.8	35.1	33.2	39.7	32.7
Ta	34.3	38.7	24.9	32.2	35.6	37.1	21.7	19.2	24.3	19.6	24.9	28.4	29.9	29.1	34.0	33.2
W	1.33	2.48	1.52	1.83	1.40	1.63	2.30	1.24	1.21	1.00	1.32	1.44	1.06	1.26	3.01	1.04
Tl	—	—	0.349	—	—	0.250	—	—	—	—	—	—	0.0531	—	—	—
Pb	2.85	2.02	3.64	6.06	6.43	4.90	2.84	1.37	3.41	1.56	1.17	2.05	1.42	—	6.39	4.19
Th	120	87.8	107	108	103	74.8	26.3	66.1	78.1	75.0	75.2	87.1	82.6	86.3	102	106
U	21.2	17.0	24.6	24.3	18.4	13.9	8.09	14.3	13.7	13.8	15.9	16.4	13.3	13.8	19.4	16.1

1

Table S2: Major and trace element compositions of titanite. Oxides are in wt%, trace elements are in $\mu g/g$.

	TtnA-19	TtnA-20	TtnA-21	TtnA-22	TtnA-23	TtnA-24	TtnA-25	TtnA-26	TtnA-27	TtnA-28	TtnA-29	TtnA-30	TtnA-31	TtnA-32	TtnA-33	TtnA-34
SiO_2	29.00	28.97	29.13	28.97	28.95	28.98	29.25	28.86	29.03	28.98	29.58	29.06	29.14	28.75	29.06	28.94
TiO_2	38.43	38.93	38.63	38.51	38.62	38.43	38.25	37.73	38.00	38.37	38.01	37.16	38.33	38.18	38.38	38.76
Al_2O_3	1.82	1.72	1.75	1.87	1.83	1.87	2.00	2.09	2.10	1.93	2.02	2.06	1.78	1.86	1.99	1.81
FeO	0.56	0.54	0.56	0.51	0.55	0.61	0.59	0.63	0.62	0.54	0.53	0.52	0.74	0.57	0.53	0.56
MnO	0.05	0.05	0.04	0.04	0.04	0.04	0.04	0.04	0.04	0.04	0.04	0.05	0.03	0.04	0.04	0.04
MgO	0.02	0.01	0.01	0.01	0.01	0.01	0.01	0.01	0.01	0.01	0.01	0.01	0.00	0.01	0.01	0.01
CaO	28.35	28.04	28.31	28.46	28.10	27.82	27.71	28.41	28.01	28.12	27.67	29.23	28.59	28.93	28.42	28.19
Na_2O	0.02	—	—	0.01	0.05	0.01	0.01	0.01	0.02	0.01	0.01	0.03	0.02	0.01	0.03	0.01
K_2O	0.00	0.01	—	—	—	0.01	0.01	0.01	—	—	0.01	—	0.00	0.00	—	0.00
P_2O_5	0.16	0.11	—	0.14	0.02	0.18	0.13	0.12	0.21	0.14	0.13	0.19	0.16	0.17	0.17	0.12
Li	—	—	—	—	—	—	—	—	—	—	—	—	—	—	—	—
Sc	9.18	—	—	11.5	1.91	5.77	—	—	—	—	3.75	—	4.55	5.57	6.54	—
V	249	264	266	262	193	196	213	178	189	191	190	213	214	175	203	179
Cr	6.40	3.98	22.2	6.29	3.68	8.25	10.3	—	3.10	13.2	—	9.69	12.1	—	—	15.5
Co	0.0281	—	—	0.0171	—	—	—	—	—	—	—	—	—	—	—	—
Ni	—	—	—	—	—	—	—	—	—	—	—	—	—	—	0.30	—
Cu	—	398	—	—	237	—	—	801	41.9	51.7	69.3	1450	—	—	279	188
Zn	—	—	8.69	—	7.45	2.71	8.11	—	5.83	—	—	25.7	3.60	—	6.82	28.8
Ga	2.75	2.78	3.31	3.01	2.97	3.71	4.02	3.60	3.96	3.35	4.07	3.07	4.34	3.17	3.49	3.69
Rb	0.555	1.83	0.186	4.77	—	—	0.514	4.05	0.323	—	—	—	—	0.749	—	—
Sr	86.6	85.3	82.3	79.8	76.2	74.8	74.1	70.1	70.8	62.3	69.5	71.5	42.8	71.3	71.4	73.1
Y	773	775	805	739	944	1140	1110	984	1050	1130	1230	1170	929	746	637	793
Zr	719	733	735	746	698	628	633	687	674	993	669	651	537	906	1010	844
Nb	457	536	577	509	737	633	637	718	659	727	577	533	699	905	903	887
Cs	0.142	—	0.485	—	2.73	—	—	—	0.87	0.51	—	—	—	1.13	3.02	—
Ba	—	0.216	—	—	—	—	—	—	—	—	—	2.16	—	—	0.717	—
La	1110	1160	1130	1060	1350	1470	1440	1500	1440	1320	1420	1300	597	1170	977	1200
Ce	4410	4360	4250	4130	5120	5710	5610	5760	5440	4850	5410	2320	2770	4000	3440	4170
Pr	680	687	663	638	789	914	895	889	881	755	843	802	467	564	490	591
Nd	3070	2970	2930	2770	3350	4090	3980	3830	3790	3370	3870	3450	2120	2290	2000	2450
Sm	566	481	513	494	605	773	772	695	720	641	738	640	413	373	303	405
Eu	82.8	79.4	78.6	76.0	73.6	84.3	86.9	77.2	77.1	70.8	83.6	70.8	55.0	53.1	46.0	54.7
Gd	344	329	335	304	387	492	497	439	464	414	503	452	295	252	205	254
Tb	37.9	32.4	36.3	34.3	43.2	56.4	56.3	49.0	51.2	47.2	57.9	50.9	33.4	30.0	24.6	32.1
Dy	183	167	182	170	212	273	250	244	245	243	283	276	182	157	129	165
Ho	28.3	26.4	27.5	26.3	31.7	42.2	37.4	37.7	38.5	39.5	44.1	41.7	33.0	23.9	22.9	27.4
Er	64.7	59.4	65.7	62.7	71.5	90.1	87.2	87.1	87.2	91.0	107	102	80.0	66.7	51.0	68.8
Tm	6.38	7.00	7.62	7.16	8.17	10.0	10.2	8.92	10.8	10.5	13.0	12.7	10.4	8.00	6.16	8.59
Yb	35.4	42.4	44.3	40.1	50.7	56.0	53.4	56.4	55.7	61.6	70.4	64.0	60.5	46.6	35.2	48.1
Lu	3.85	4.71	4.44	4.55	5.75	6.66	6.60	6.19	6.47	7.47	7.98	8.83	7.82	5.01	3.79	5.49
Hf	30.1	29.7	31.2	35.1	35.7	32.8	32.8	35.7	34.7	41.2	35.7	30.0	31.8	44.4	44.5	35.8
Ta	35.1	36.3	38.5	33.0	49.6	48.9	45.1	51.5	45.5	51.3	40.6	35.1	44.1	59.8	53.8	58.1
W	1.00	1.20	1.21	1.29	1.53	1.76	1.34	1.40	1.52	3.21	2.02	1.33	6.92	2.95	2.81	2.71
Tl	—	—	—	—	—	—	—	—	—	—	—	—	—	—	—	0.0808
Pb	1.09	2.22	—	3.30	4.78	2.98	4.64	6.50	3.70	6.29	2.71	4.92	2.84	3.15	1.95	2.65
Th	115	116	114	113	127	128	130	145	139	115	122	119	64.2	116	99.4	113
U	16.1	14.9	16.0	17.0	17.0	18.3	19.4	20.6	20.1	19.4	20.6	21.8	21.4	21.4	17.5	22.1

Table S3: Major and trace element compositions of titanite. Oxides are in wt%, trace elements are in $\mu g/g$.

	TtnA-35	TtnA-36	TtnA-37	TtnA-38	TtnA-39	TtnA-40	TtnA-41	TtnA-42	TtnA-43	TtnA-44	TtnA-45	TtnA-46	TtnA-47	TtnA-48	TtnA-49	TtnA-52
SiO_2	28.73	29.08	29.03	29.36	32.93	33.93	28.68	28.91	28.79	29.31	28.78	29.18	29.11	29.76	28.73	28.88
TiO_2	38.70	38.50	37.97	37.94	44.44	44.13	38.51	38.67	38.86	37.66	38.25	37.95	38.15	37.39	38.58	38.68
Al_2O_3	1.90	1.84	1.96	1.95	2.09	2.30	1.94	1.97	2.22	2.21	2.09	2.12	2.18	2.37	1.77	1.97
FeO	0.55	0.56	0.50	0.56	0.60	0.69	0.51	0.58	0.63	0.63	0.60	0.55	0.57	0.60	0.57	0.46
MnO	0.04	0.04	0.04	0.04	0.05	0.05	0.04	0.03	0.04	0.04	0.04	0.03	0.04	0.04	0.04	0.04
MgO	0.02	0.01	0.01	0.02	0.01	0.03	0.01	0.01	0.01	0.01	0.01	0.01	—	0.01	0.01	0.01
CaO	28.42	28.31	29.05	28.75	18.09	17.53	28.87	28.44	28.29	28.79	28.81	28.77	28.60	28.48	28.69	28.52
Na_2O	0.02	—	—	0.01	—	0.02	0.01	0.01	0.02	0.01	—	0.04	0.02	0.01	0.01	0.01
K_2O	0.00	—	—	0.02	—	0.00	—	0.00	—	0.00	—	—	—	0.00	—	0.00
P_2O_5	0.08	0.07	0.18	0.13	0.39	0.15	0.20	0.15	0.16	0.13	0.19	0.16	0.18	0.17	0.17	0.18
Li	—	—	—	—	—	—	—	—	—	—	—	—	—	—	—	—
Sc	2.86	—	—	6.83	46.5	5.37	—	2.97	3.82	5.76	—	15.9	3.83	4.18	2.43	12.9
V	197	222	256	267	287	267	249	263	277	289	285	290	274	280	185	187
Cr	9.96	2.93	—	—	65.7	—	—	16.4	5.60	11.0	21.1	14.1	13.5	3.03	3.67	2.97
Co	—	—	—	—	—	0.05	—	—	—	—	—	—	—	—	—	—
Ni	—	—	—	—	—	10.20	—	—	—	—	—	—	—	—	—	—
Cu	—	282	—	—	—	—	145	136	22.7	—	—	—	5.81	2.08	—	111
Zn	1.36	7.23	—	6.54	29.5	18.8	—	—	4.92	—	—	—	—	—	—	—
Ga	2.92	3.42	2.72	3.69	3.89	4.09	3.17	2.86	3.43	3.38	3.30	3.01	3.39	4.26	2.64	2.09
Rb	1.11	—	—	—	4.78	1.19	—	—	0.504	1.12	1.10	—	—	—	—	0.362
Sr	72.7	78.9	81.3	82.3	92.1	86.1	79.0	88.6	89.6	90.5	91.1	86.6	82.8	96.7	72.6	82.4
Y	766	877	725	660	699	733	597	581	643	617	687	649	641	669	666	573
Zr	934	769	796	813	1020	1010	895	924	939	914	921	861	783	832	718	759
Nb	858	570	475	557	586	720	577	562	451	439	462	445	404	425	691	473
Cs	—	1.35	—	—	1.29	0.294	0.355	0.905	—	0.679	—	0.107	—	—	—	0.984
Ba	—	4.14	—	—	—	5.64	—	—	—	—	0.966	—	—	—	—	—
La	1120	1090	885	868	943	1000	846	828	850	822	835	765	858	802	1320	823
Ce	4020	4130	3230	3060	3490	1370	3120	3020	966	3020	3070	2930	2810	2980	4310	3230
Pr	590	633	506	458	528	535	476	469	475	458	486	469	447	453	595	510
Nd	2610	2800	2140	2020	2300	2320	2050	2030	2070	2030	2070	1950	1960	1910	2170	2320
Sm	460	517	389	352	405	416	352	355	364	346	359	362	323	343	371	428
Eu	58.2	72.7	67.0	58.4	74.9	76.1	65.4	65.7	68.4	65.9	60.0	59.0	56.9	60.6	50.8	69.8
Gd	298	345	247	233	269	257	226	219	233	237	244	238	216	226	231	260
Tb	32.1	39.0	30.0	26.9	29.8	29.5	25.6	25.2	26.9	27.7	25.2	26.5	23.8	26.5	22.4	28.5
Dy	175	195	154	140	141	150	133	130	145	135	145	148	139	134	126	134
Ho	26.3	30.6	23.3	23.7	23.4	24.9	21.3	21.5	23.5	20.9	22.3	22.4	24.5	23.1	21.0	21.2
Er	69.5	74.0	64.3	52.4	61.4	65.2	52.0	52.1	55.7	51.1	53.0	52.5	54.6	54.6	50.0	48.9
Tm	8.21	9.29	6.96	7.33	6.83	7.90	5.53	6.07	6.67	6.79	7.00	6.55	6.49	6.13	6.13	5.92
Yb	45.1	51.1	43.5	40.8	35.7	44.3	30.5	33.8	36.4	32.1	38.2	39.1	33.7	39.8	35.4	32.8
Lu	4.55	5.52	5.03	4.84	3.90	4.10	3.99	3.09	3.89	3.48	4.27	4.40	4.64	4.47	4.27	3.78
Hf	39.7	36.9	38.5	38.8	45.2	39.2	39.9	43.3	41.8	38.3	35.2	35.3	38.3	41.3	32.1	34.3
Ta	55.0	36.9	31.5	29.1	30.3	42.1	31.6	31.1	25.5	23.3	25.5	22.9	23.2	25.8	28.1	30.7
W	2.43	1.86	1.97	2.87	1.91	2.02	1.63	1.54	1.70	1.35	1.49	1.40	1.23	1.62	2.59	1.24
Tl	—	2.44	—	—	—	0.558	—	—	—	—	—	—	0.722	—	—	—
Pb	2.14	1.85	4.66	1.42	—	2.34	2.53	0.939	1.62	2.52	0.449	—	1.80	2.19	5.48	2.23
Th	103	98.4	86.5	78.8	95.4	82.6	78.5	69.0	76.0	75.7	72.0	79.2	69.7	75.7	118	80.1
U	18.6	15.8	17.3	17.0	15.2	16.1	15.0	14.2	14.5	13.1	12.7	12.6	15.5	14.3	18.6	15.9

Table S4: Major and trace element compositions of titanite. Oxides are in wt%, trace elements are in μg/g.

	TtnA-53	TtnA-54	TtnA-55	TtnA-56
SiO$_2$	28.95	28.81	28.44	31.38
TiO$_2$	38.84	38.51	38.51	35.20
Al$_2$O$_3$	1.92	1.87	2.04	2.01
FeO	0.48	0.49	0.49	0.56
MnO	0.05	0.05	0.04	0.04
MgO	0.01	0.01	0.01	0.02
CaO	28.24	28.58	28.39	28.62
Na$_2$O	0.02	0.01	0.02	0.00
K$_2$O	0.00	0.00	—	0.01
P$_2$O$_5$	0.16	0.18	0.15	0.16
Li	—	—	—	—
Sc	5.33	—	2.70	—
V	210	220	202	183
Cr	—	7.39	—	17.2
Co	—	—	—	—
Ni	—	—	—	—
Cu	167	49.1	—	362
Zn	13.2	—	—	—
Ga	3.42	2.97	2.67	3.99
Rb	2.79	2.41	—	—
Sr	77.8	77.4	70.5	63.1
Y	746	895	1200	1240
Zr	763	799	667	645
Nb	433	529	615	577
Cs	0.326	—	—	—
Ba	—	—	—	—
La	924	1080	1390	1440
Ce	3450	3930	5230	5540
Pr	543	612	813	849
Nd	2350	2590	3630	3670
Sm	410	482	697	741
Eu	72.3	69.9	70.5	75.4
Gd	268	307	453	416
Tb	30.9	37.5	50.5	54.4
Dy	156	189	277	279
Ho	25.9	31.9	42.4	44.3
Er	57.8	79.9	93.0	102.0
Tm	7.01	9.62	10.9	13.2
Yb	42.7	53.7	65.1	69.5
Lu	5.01	6.07	6.63	8.38
Hf	35.8	37.3	27.8	34.9
Ta	27.0	33.9	42.3	39.2
W	1.30	1.77	1.69	2.16
Tl	—	—	0.01	—
Pb	4.48	3.12	2.72	3.73
Th	85.5	107	123	128
U	15.0	22.1	22.5	21.9

Table S5: Major and trace element compositions of titanite. Oxides are in wt%, trace elements are in $\mu g/g$.

	TtnB-01	TtnB-02	TtnB-03	TtnB-04	TtnB-05	TtnB-06	TtnB-07	TtnB-08	TtnB-09	TtnB-10	TtnB-11	TtnB-12	TtnB-13	TtnB-14	TtnB-15	TtnB-16
SiO_2	30.62	29.35	29.13	28.79	29.06	28.92	29.18	29.02	28.76	28.79	28.85	28.85	29.30	28.13	28.02	28.58
TiO_2	36.51	38.40	38.50	38.72	38.18	38.27	38.16	38.26	38.43	38.45	38.28	38.14	38.19	39.10	38.74	38.83
Al_2O_3	2.49	2.17	1.75	1.74	2.16	2.39	2.28	2.17	2.12	2.05	2.03	2.06	2.07	1.93	1.78	1.85
FeO	0.51	0.53	0.58	0.60	0.61	0.78	0.71	0.73	0.77	0.73	0.72	0.71	0.68	0.64	0.65	0.64
MnO	0.04	0.05	0.04	0.04	0.04	0.04	0.04	0.04	0.04	0.04	0.04	0.04	0.04	0.04	0.06	0.07
MgO	0.01	0.01	0.01	0.00	0.01	0.04	0.01	0.01	0.03	0.01	0.01	0.01	0.01	0.01	0.03	0.02
CaO	27.72	28.16	28.02	27.95	28.63	28.27	28.43	28.51	28.50	28.66	28.79	28.81	28.37	28.50	28.69	28.05
Na_2O	0.20	0.01	—	0.02	0.03	—	0.01	0.02	0.04	0.02	—	0.02	0.02	0.01	0.02	—
K_2O	0.04	—	—	0.00	0.00	0.01	0.00	—	0.01	0.01	—	0.01	—	0.00	0.01	—
P_2O_5	0.24	0.16	0.10	0.13	0.13	0.25	0.10	0.17	0.22	0.13	0.17	0.29	0.13	0.08	0.22	0.15
Li	13.4	—	—	—	—	—	—	—	—	—	—	—	—	—	—	4.60
Sc	—	—	—	—	—	—	—	—	40.9	—	—	—	—	—	—	—
V	222	253	220	185	266	428	405	352	314	329	327	335	504	433	406	402
Cr	12.2	3.22	—	—	2.31	22.5	—	—	—	18.3	6.49	—	10.8	—	19.3	11.2
Co	—	—	0.01	—	—	0.06	—	0.01	0.03	—	—	—	—	—	—	—
Ni	—	—	0.23	—	—	—	—	—	—	—	—	—	—	—	—	—
Cu	184	—	—	471	—	—	—	—	83.7	74.5	—	—	—	—	66.7	237
Zn	—	—	—	18.9	12.4	5.20	—	4.73	5.24	2.03	—	—	9.50	15.5	—	—
Ga	4.16	3.23	2.79	2.62	3.57	3.26	3.77	3.00	3.65	3.44	2.54	3.43	3.55	3.89	2.68	3.04
Rb	2.55	—	—	2.25	—	—	1.25	1.85	—	—	—	1.35	—	—	—	—
Sr	107	80.3	74.4	69.2	84.4	76.0	77.2	73.0	76.0	73.8	77.3	77.1	81.0	71.2	61.3	60.3
Y	1020	620	1010	1020	616	865	912	850	783	753	775	747	1020	1240	1420	1380
Zr	586	840	657	640	778	705	765	752	823	907	869	870	722	671	653	699
Nb	529	492	542	660	418	377	477	554	664	696	700	618	508	449	549	561
Cs	0.137	—	0.755	—	—	—	0.482	0.367	—	0.111	0.150	—	—	—	—	—
Ba	0.400	—	—	—	—	—	—	—	—	—	—	—	—	—	—	2.85
La	1160	801	1420	1420	791	622	631	643	646	668	678	659	705	1190	1360	1430
Ce	4390	3010	5500	5520	3020	2330	2470	2440	2490	2500	2560	2480	2690	3990	4690	4670
Pr	671	450	835	847	458	360	362	357	355	363	366	363	411	597	692	702
Nd	2920	1920	3590	3790	1940	1480	1550	1500	1490	1510	1530	1460	1710	2430	2880	2930
Sm	533	325	649	686	334	269	273	264	251	269	267	267	314	448	497	524
Eu	69.1	57.2	80.4	78.3	58.3	55.2	61.0	54.2	60.1	60.5	62.4	58.5	65.2	63.9	73.3	80.6
Gd	344	222	387	406	223	216	226	214	206	196	183	194	255	340	369	366
Tb	43.8	26.2	44.0	46.9	23.8	26.1	28.1	29.0	27.5	24.4	24.0	24.4	32.3	38.6	48.6	49.9
Dy	223	135	232	226	125	171	169	150	154	151	154	153	206	248	297	284
Ho	34.4	21.3	32.7	37.7	22.8	27.9	30.0	28.4	27.3	27.2	27.3	28.0	36.8	40.5	51.5	48.6
Er	81.2	55.6	80.0	90.9	52.6	69.8	82.4	78.9	67.9	69.7	64.4	66.4	90.5	113	127	121
Tm	9.84	5.69	9.13	9.94	6.02	10.1	10.8	9.13	8.92	8.05	7.79	9.08	11.2	14.4	15.5	13.5
Yb	55.6	38.1	48.8	56.7	32.7	49.8	64.3	57.5	48.2	52.2	47.5	53.1	63.5	78.7	79.2	81.1
Lu	6.16	4.24	5.18	6.06	3.73	5.77	6.55	6.12	5.52	6.07	6.12	6.39	7.27	9.28	8.38	9.63
Hf	26.6	32.2	33.1	31.8	36.1	28.2	33.5	35.1	32.5	35.7	38.5	37.0	30.6	34.5	29.5	33.3
Ta	31.8	26.8	24.2	44.1	20.9	19.6	24.0	25.4	32.3	32.6	35.8	32.7	24.9	27.0	30.8	32.3
W	1.89	1.59	1.65	1.41	1.33	1.36	1.32	1.70	2.06	1.79	1.86	1.79	1.53	1.42	1.38	1.64
Tl	—	—	—	—	—	—	—	—	—	—	—	—	—	—	—	—
Pb	3.76	1.56	6.09	5.02	1.88	2.17	2.66	1.15	3.61	3.79	3.21	2.72	1.03	7.82	3.10	3.14
Th	97.8	64.4	122	126	66.6	47.6	46.6	51.0	48.8	52.9	45.4	46.8	49.0	81.4	94.3	111
U	20.2	15.9	16.5	16.5	13.4	12.7	16.3	13.4	15.5	15.7	16.4	13.8	16.5	19.1	22.7	26.6

Table S6: Major and trace element compositions of titanite. Oxides are in wt%, trace elements are in μg/g.

	TtnB-17	TtnB-18	TtnB-19	TtnB-20	TtnB-21	TtnB-22	TtnB-23	TtnB-24	TtnB-25	TtnB-26	TtnB-27	TtnB-28	TtnB-29	TtnB-30	TtnB-31
SiO_2	28.43	28.94	27.51	27.87	27.29	28.04	27.28	27.20	27.20	26.95	26.98	26.63	26.62	26.44	25.41
TiO_2	39.04	38.62	39.31	39.45	39.87	39.28	39.23	39.89	39.46	39.48	40.02	39.90	39.46	37.97	40.94
Al_2O_3	1.80	1.76	1.70	1.77	1.75	1.74	1.96	2.11	2.20	2.01	2.05	2.07	2.11	3.21	1.86
FeO	0.67	0.61	0.62	0.63	0.62	0.61	0.62	0.62	0.66	0.66	0.59	0.54	0.50	0.48	0.45
MnO	0.06	0.06	0.07	0.07	0.07	0.06	0.04	0.03	0.04	0.03	0.04	0.04	0.04	0.04	0.04
MgO	0.03	0.01	0.02	0.02	0.02	0.01	0.01	0.01	0.01	0.01	0.01	0.01	0.01	0.01	0.01
CaO	28.25	28.33	28.76	28.11	28.28	27.89	29.11	28.86	29.25	29.49	28.57	29.33	30.05	30.49	29.63
Na_2O	—	—	0.01	0.01	0.02	0.03	0.01	0.00	—	0.01	—	0.00	0.00	0.01	0.01
K_2O	—	—	—	0.01	—	0.04	—	0.00	—	0.01	—	0.00	0.00	0.01	—
P_2O_5	0.18	—	0.15	0.18	0.18	0.50	0.17	0.16	0.15	0.20	0.17	0.15	0.06	0.14	0.11
Li	—	—	—	—	—	16.7	2.10	—	—	—	—	—	5.14	—	—
Sc	—	38.7	21.0	7.50	5.59	—	—	—	—	24.0	—	—	—	—	—
V	417	415	372	414	391	389	240	241	161	156	200	242	273	264	226
Cr	—	—	18.6	12.4	12.3	4.77	3.02	3.06	—	6.61	4.78	23.2	7.26	5.32	5.15
Co	—	—	—	—	—	—	—	—	—	—	—	—	—	—	—
Ni	—	—	—	—	—	—	—	—	—	—	—	—	—	—	—
Cu	573	—	—	—	71.5	—	—	52.4	203	—	63.1	—	—	—	—
Zn	20.6	—	—	27.4	—	—	1.41	8.69	5.11	—	7.51	3.96	0.705	1.75	2.06
Ga	3.00	2.85	2.71	3.12	3.25	1.62	1.67	3.14	3.08	2.51	2.60	3.10	2.93	4.20	2.27
Rb	—	—	1.63	0.0949	1.21	4.55	—	—	—	—	—	0.170	—	0.0292	—
Sr	60.3	61.6	60.8	61.3	66.0	55.8	80.3	85.1	74.5	74.2	74.6	83.0	80.3	88.6	84.6
Y	1330	369	1340	1400	1380	1440	879	620	527	557	815	578	517	663	995
Zr	732	729	691	753	796	649	1050	1130	964	852	822	793	933	870	697
Nb	552	512	585	615	656	565	747	711	954	839	665	495	504	428	559
Cs	1.44	—	—	—	—	0.0830	0.571	0.226	0.666	—	—	—	—	0.207	0.816
Ba	—	—	—	—	—	—	—	—	—	—	—	—	—	—	—
La	1470	1450	1530	1500	1470	—	1160	736	661	809	1100	882	785	809	1100
Ce	2060	4930	5060	5070	5090	5530	4090	2620	2370	2940	4220	3710	2900	3130	4150
Pr	702	711	700	734	724	779	613	367	335	409	674	551	425	457	619
Nd	2850	2650	2980	2980	3070	3260	2530	1500	1320	1610	2740	2310	1830	2000	2770
Sm	539	533	518	534	546	583	454	262	219	256	523	407	312	380	505
Eu	82.1	81.8	77.2	82.9	81.9	73.8	82.3	65.0	50.6	54.3	70.1	70.1	65.6	70.6	75.3
Gd	393	373	370	392	413	436	298	182	133	171	333	250	202	252	351
Tb	49.7	50.1	47.3	49.7	51.7	52.1	38.7	23.2	17.8	19.8	34.7	25.3	22.6	28.2	41.2
Dy	275	256	262	290	297	298	202	133	100	121	170	137	116	150	225
Ho	44.2	44.4	43.3	49.8	51.2	50.5	32.6	21.3	17.4	18.9	29.4	21.1	18.1	24.2	32.4
Er	115	119	124	126	121	118	78.2	55.8	39.3	43.7	68.3	48.0	46.3	59.8	91.4
Tm	14.6	13.4	17.0	14.0	13.7	13.9	9.10	6.00	4.97	5.93	6.88	5.44	5.81	7.42	10.1
Yb	79.4	70.3	76.9	87.7	85.4	88.3	49.4	34.8	29.6	35.1	44.7	34.2	30.6	43.2	54.5
Lu	9.54	8.20	9.41	9.22	8.65	9.45	4.63	3.54	3.22	3.29	4.54	3.79	3.30	4.60	6.65
Hf	34.2	27.4	31.7	31.5	33.5	30.9	40.9	46.7	38.3	36.6	37.2	39.1	37.6	39.1	29.4
Ta	34.3	34.0	33.5	32.1	36.9	38.3	40.2	35.0	46.6	46.8	40.6	24.9	22.1	23.5	37.2
W	1.50	1.53	1.58	1.69	1.39	1.41	1.32	1.53	1.69	1.78	1.49	1.50	1.59	1.62	1.96
Tl	0.30	—	—	—	—	—	—	—	—	—	—	—	—	—	—
Pb	—	5.99	3.77	4.21	2.47	6.74	3.54	3.24	4.21	—	7.05	2.38	0.97	1.17	1.22
Th	111	99.8	102	117	111	137	69.4	37.0	43.6	70.6	121	101	75.6	80.0	112
U	26.9	22.5	25.2	26.9	24.9	26.0	16.8	12.4	12.4	17.2	19.9	16.2	15.7	16.2	24.0

Table S7: Major and trace element compositions of clinopyroxene. Oxides are in wt%, trace elements are in $\mu g/g$.

	CpxA-01	CpxA-03	CpxA-04	CpxA-05	CpxA-06	CpxA-07	CpxA-08	CpxA-09	CpxA-10	CpxA-11	CpxA-12	CpxA-13	CpxA-14	CpxA-15
SiO_2	50.08	50.35	50.10	49.99	50.61	50.15	49.69	49.76	50.74	49.75	49.43	49.97	50.50	49.69
TiO_2	0.05	0.05	0.06	0.02	0.02	0.04	0.03	0.07	0.03	0.08	0.05	0.07	—	0.03
Al_2O_3	0.47	0.56	0.54	0.35	0.38	0.37	0.38	0.53	0.48	0.44	0.40	0.54	0.33	0.28
FeO	17.23	17.39	18.12	17.78	17.89	18.24	18.46	18.78	18.77	18.31	18.49	18.38	18.30	18.24
MnO	0.35	0.35	0.38	0.36	0.36	0.39	0.39	0.42	0.41	0.40	0.40	0.41	0.40	0.39
MgO	8.04	8.02	7.54	7.88	7.28	7.86	7.72	7.24	7.46	7.34	7.52	7.38	7.63	7.72
CaO	23.38	22.91	22.51	22.95	23.14	22.49	22.69	22.63	21.76	23.11	23.20	22.75	22.48	23.17
Na_2O	—	—	0.25	0.21	—	0.22	0.21	0.23	0.20	0.24	0.21	0.23	—	0.17
K_2O	—	0.01	0.01	—	—	0.01	0.00	0.01	0.01	0.00	—	0.01	—	—
P_2O_5	0.30	0.28	0.34	0.35	0.24	0.16	0.32	0.25	0.08	0.27	0.23	0.19	0.23	0.23
Li	—	—	—	—	—	—	—	—	—	—	—	—	—	—
Sc	17.3	20.2	65.9	26.8	36.8	11.4	18.5	14.5	21.6	25.5	21.1	50.0	66.2	30.3
V	92.7	82.7	72.9	84.8	90.7	78.4	79.5	66.6	66.6	77.3	65.9	60.4	69.0	62.6
Cr	14.5	19.1	—	28.9	—	—	—	—	—	—	11.2	—	—	8.47
Co	22.9	19.3	18.8	18.4	23.6	24.3	20.3	23.2	23.7	21.8	23.0	23.8	19.0	20.0
Ni	146	—	4.15	—	—	—	—	—	2.77	—	—	2.05	5.61	—
Cu	—	—	651	347	—	54.1	133	29.9	—	—	62.9	—	529	148
Zn	386	381	262	402	426	370	361	352	338	317	338	370	277	364
Ga	3.58	3.44	4.19	2.88	3.18	3.87	3.57	3.41	2.38	3.07	3.22	3.23	2.97	2.58
Rb	—	1.66	6.00	11.9	1.75	1.30	—	—	—	0.293	0.190	—	—	0.990
Sr	36.1	47.5	34.9	26.1	26.1	28.7	26.6	38.9	31.3	32.7	30.5	34.9	25.4	27.3
Y	3.42	5.03	5.59	3.85	4.19	5.24	4.95	8.21	3.78	5.68	3.36	4.46	2.88	1.87
Zr	18.8	16.3	15.4	5.74	13.7	16.7	17.5	14.0	7.77	9.97	13.3	11.2	9.67	5.20
Nb	—	—	—	—	—	—	—	—	—	—	—	—	—	—
Cs	1.38	—	0.800	—	—	1.74	—	—	1.97	—	—	0.213	0.706	—
Ba	3.52	—	—	—	—	—	—	—	—	—	—	—	—	—
La	2.44	3.31	4.40	0.847	0.623	1.09	1.13	4.67	2.08	4.63	2.66	2.50	0.551	0.456
Ce	8.77	11.6	14.5	4.51	3.54	5.25	5.43	17.8	7.72	16.6	9.55	9.58	3.03	2.26
Pr	1.43	1.85	2.07	0.635	0.674	0.893	0.892	2.91	1.24	2.44	1.40	1.42	0.493	0.363
Nd	4.65	6.97	7.90	2.87	3.27	4.00	4.32	11.7	5.03	7.68	6.52	4.99	2.53	1.60
Sm	0.892	1.07	1.47	0.487	0.574	0.850	0.819	1.69	0.804	1.37	1.02	1.04	0.484	0.340
Eu	0.0695	0.131	0.121	—	—	0.0794	0.0966	0.145	—	0.136	0.0778	0.114	0.0281	0.0105
Gd	0.600	0.754	1.04	0.477	0.561	0.794	0.759	1.32	0.944	1.17	0.791	0.663	0.437	0.263
Tb	0.0602	0.0882	0.139	0.0556	0.0648	0.107	0.0801	0.198	0.108	0.113	0.105	0.0839	0.0560	0.0161
Dy	0.505	0.658	0.933	0.450	0.507	0.697	0.738	1.38	0.653	0.827	0.613	0.591	0.427	0.271
Ho	0.0837	0.144	0.166	0.0927	0.0893	0.106	0.154	0.262	0.115	0.143	0.113	0.0990	0.0755	0.0282
Er	0.234	0.420	0.514	0.395	0.310	0.418	0.548	0.910	0.407	0.477	0.348	0.312	0.325	0.0802
Tm	0.0218	0.0597	0.0935	0.0362	0.0400	0.0558	0.0663	0.142	0.0524	0.0843	0.0193	0.0473	0.0244	0.0141
Yb	0.444	0.509	0.938	0.604	0.649	0.640	0.922	1.30	0.736	0.794	0.513	0.567	0.513	0.233
Lu	0.131	0.143	0.238	0.148	0.204	0.203	0.222	0.355	0.233	0.235	0.166	0.131	0.131	0.102
Hf	0.406	0.564	0.393	0.278	0.536	0.491	0.393	0.499	0.216	0.425	0.319	0.475	0.331	0.153
Ta	—	—	—	—	—	—	—	—	—	—	—	—	—	—
W	—	—	—	—	—	—	—	—	—	—	—	—	—	—
Tl	—	—	—	—	—	—	—	—	—	—	—	0.01	—	—
Pb	—	—	12.5	—	4.33	—	—	1.29	3.41	—	1.04	—	6.30	2.90
Th	—	—	—	—	—	—	—	—	—	—	—	—	—	—
U	—	—	—	—	—	—	—	—	—	—	—	—	—	—

Table S8: Major and trace element compositions of clinopyroxene. Oxides are in wt%, trace elements are in μg/g.

SiO_2	46.00	46.25	46.27	47.03	45.75	45.36	46.91	47.95	48.23
TiO_2	0.03	0.05	0.01	0.03	0.03	0.02	0.02	0.04	0.04
Al_2O_3	0.37	0.44	0.40	0.46	0.42	0.31	0.36	0.42	0.58
FeO	18.65	17.51	17.26	17.95	17.80	18.63	18.44	17.96	17.38
MnO	0.39	0.34	0.37	0.33	0.37	0.33	0.36	0.38	0.36
MgO	8.11	8.72	9.02	8.21	9.01	8.76	8.30	7.83	8.46
CaO	26.06	26.29	26.24	25.58	26.23	26.25	25.20	24.98	24.39
Na_2O	0.12	0.13	0.09	0.13	0.11	0.10	0.15	0.15	0.23
K_2O	0.00	0.00	0.00	0.01	—	—	—	0.00	0.01
P_2O_5	0.22	0.20	0.29	0.22	0.20	0.19	0.19	0.23	0.26
Li	—	—	—	—	—	—	—	—	—
Sc	43.8	35.3	42.7	39.0	70.7	32.2	41.2	29.2	—
V	96.0	86.4	76.7	86.5	92.6	80.8	86.1	85.3	83.9
Cr	5.56	—	—	—	11.1	—	—	—	—
Co	17.7	13.0	14.7	15.4	17.4	13.7	16.1	17.0	15.7
Ni	—	—	—	—	—	—	—	—	—
Cu	18.9	58.6	—	—	—	—	—	—	—
Zn	220	236	202	231	258	238	236	284	289
Ga	2.09	2.21	1.34	2.02	2.26	1.55	2.18	2.82	1.80
Rb	—	—	—	—	—	—	—	—	0.142
Sr	30.5	34.6	28.3	28.4	36.9	29.0	28.9	31.7	42.6
Y	2.57	3.44	2.40	3.15	3.02	2.63	2.74	3.07	4.46
Zr	4.48	8.50	6.35	5.57	11.5	3.97	7.67	8.30	10.4
Nb	—	—	—	—	—	—	—	—	—
Cs	—	—	1.60	—	—	0.490	—	—	—
Ba	—	—	—	—	—	—	—	—	—
La	0.644	1.35	0.448	0.706	1.67	0.256	0.499	1.33	5.01
Ce	3.19	6.03	3.37	3.68	6.39	3.07	2.84	5.90	15.30
Pr	0.564	0.802	0.585	0.572	1.00	0.493	0.480	0.969	2.11
Nd	2.26	4.08	2.38	2.34	3.04	2.21	1.91	3.50	7.02
Sm	0.337	0.407	0.0607	0.251	0.350	0.136	0.239	0.670	0.848
Eu	0.0203	0.0280	—	0.0667	0.00695	0.0111	0.00436	0.0552	0.0931
Gd	0.238	0.267	0.170	0.333	0.0351	0.146	0.0560	0.370	0.756
Tb	0.00650	0.0316	0.0201	—	—	—	0.0249	0.0557	0.0497
Dy	0.231	0.348	0.265	0.204	0.096	0.150	0.115	0.241	0.616
Ho	0.0290	0.0198	—	0.0612	0.00666	0.00822	0.0479	0.0469	0.136
Er	0.139	0.188	0.142	0.126	0.274	0.117	0.0653	0.274	0.324
Tm	—	—	0.0168	0.0165	—	0.00759	0.00228	0.0214	0.0404
Yb	0.286	0.351	0.303	0.160	0.445	0.486	0.320	0.266	0.680
Lu	0.0397	0.0633	0.0553	0.0324	0.0849	0.0500	0.138	0.104	0.181
Hf	0.332	0.173	0.0285	0.0718	0.0968	—	0.0776	0.238	0.541
Ta	—	—	—	—	—	—	—	—	—
W	—	—	—	—	—	—	—	—	—
Tl	—	—	—	—	—	0.03	—	—	—
Pb	1.60	2.41	3.36	—	3.66	—	1.37	2.34	10.3
Th	—	—	—	—	—	—	—	—	0.00934
U	—	—	—	—	—	—	—	—	—

Table S9: Major and trace element compositions of plagioclase. Oxides are in wt%, trace elements are in μg/g.

	PlA-01	PlA-02	PlA-03	PlA-04	PlA-05	PlA-06	PlA-07	PlA-08	PlA-09	PlA-10
SiO_2	60.47	60.37	60.39	60.21	59.86	59.28	59.82	59.42	59.41	59.60
TiO_2	—	0.00	—	0.00	—	—	0.00	0.00	—	0.00
Al_2O_3	24.74	25.07	25.01	25.11	25.23	25.51	25.34	25.91	25.68	25.48
FeO	0.01	0.04	0.03	0.03	0.04	0.06	0.05	0.05	0.05	0.04
MnO	0.00	0.00	0.00	0.00	0.00	0.00	0.00	0.00	0.00	0.00
MgO	0.00	0.00	—	0.00	0.00	0.00	0.00	0.00	0.00	0.00
CaO	5.63	5.89	6.17	6.14	6.18	6.70	6.44	6.44	6.53	6.44
Na_2O	8.52	8.05	7.84	7.94	7.37	7.31	7.69	7.47	7.58	7.57
K_2O	0.12	0.14	0.11	0.12	0.79	0.65	0.16	0.24	0.26	0.31
P_2O_5	0.36	0.29	0.29	0.28	0.29	0.28	0.29	0.27	0.28	0.33
Li	—	—	—	—	—	—	—	—	—	—
Sc	9.70	0.364	—	7.28	2.86	—	2.66	—	4.18	—
V	—	—	—	—	—	—	—	—	—	—
Cr	—	0.209	31.2	2.48	—	—	0.680	—	—	—
Co	—	—	—	—	—	—	—	—	—	—
Ni	—	—	—	—	—	—	—	—	—	—
Cu	—	—	—	—	7.98	—	47.8	—	—	64.6
Zn	5.09	7.41	14.2	9.31	—	8.81	11.1	11.0	10.3	17.4
Ga	24.8	24.9	25.1	29.5	39.7	33.6	31.7	31.3	31.3	33.7
Rb	—	—	—	—	12.9	2.76	—	0.308	—	2.46
Sr	1230	1230	1290	1260	1330	1440	1440	1330	1470	1450
Y	0.255	0.246	0.248	—	0.247	0.245	0.237	0.255	0.261	0.235
Zr	—	—	—	—	—	—	—	—	—	0.07
Nb	—	—	—	—	—	—	—	—	—	—
Cs	—	—	—	—	—	—	—	—	0.174	0.290
Ba	16.4	37.4	32.8	34.7	659	298	136	145	209	280
La	0.202	0.817	0.748	0.773	1.80	2.36	1.20	2.65	1.94	1.10
Ce	0.268	0.670	0.583	0.596	1.39	2.15	1.24	3.00	1.90	1.20
Pr	0.0340	0.0465	0.0300	0.0122	0.0475	0.102	0.0436	0.187	0.0902	0.0316
Nd	0.190	0.0934	—	—	—	0.210	0.0781	0.193	0.0777	0.0859
Sm	0.0141	—	—	—	—	—	—	—	—	—
Eu	0.234	0.361	0.463	0.531	0.578	0.442	0.474	0.776	0.717	0.675
Gd	0.0162	—	—	—	—	—	—	—	—	—
Tb	—	—	—	—	—	—	—	—	—	—
Dy	—	—	—	—	—	—	—	—	—	—
Ho	—	—	—	—	—	—	—	—	—	—
Er	—	—	—	—	—	—	—	—	—	—
Tm	—	—	—	—	—	—	—	—	—	—
Yb	—	—	—	—	—	—	—	—	—	—
Lu	—	—	—	—	—	—	—	—	—	—
Hf	—	—	—	—	—	—	—	—	—	—
Ta	—	—	—	—	—	—	—	—	—	—
W	—	—	—	—	—	—	—	—	—	—
Tl	—	0.01	—	—	—	—	—	—	—	—
Pb	11.1	9.97	4.40	11.3	9.80	11.3	9.47	10.1	7.44	9.62
Th	—	—	—	—	—	—	—	—	—	—
U	—	—	—	—	—	—	—	—	—	—

Table S10: Major and trace element compositions of plagioclase. Oxides are in wt%, trace elements are in μg/g.

	PlB-01	PlB-02	PlB-03	PlB-04	PlB-05	PlB-06	PlB-07	PlB-08	PlB-09	PlB-10
SiO_2	61.42	59.83	59.46	59.45	59.98	58.76	59.07	58.71	59.26	59.08
TiO_2	0.00	—	0.00	—	0.00	0.00	—	—	—	0.00
Al_2O_3	24.58	25.52	25.71	25.67	25.04	26.16	25.85	26.15	25.77	25.78
FeO	0.01	0.05	0.05	0.06	0.05	0.06	0.06	0.05	0.07	0.06
MnO	0.00	0.00	0.00	0.00	0.00	0.00	0.00	0.00	0.00	0.00
MgO	—	0.00	0.00	0.00	0.00	0.00	0.00	0.00	0.00	0.00
CaO	5.45	6.24	6.53	6.57	6.59	6.75	6.81	6.84	6.81	7.01
Na_2O	7.97	7.75	7.51	7.50	7.57	7.49	7.41	7.47	7.28	7.30
K_2O	0.12	0.17	0.29	0.30	0.31	0.32	0.33	0.31	0.31	0.29
P_2O_5	0.28	0.26	0.27	0.25	0.27	0.25	0.26	0.25	0.29	0.27
Li	—	—	—	—	—	—	—	—	—	—
Sc	—	10.9	—	2.63	—	8.03	15.3	11.6	—	—
V	—	—	—	—	—	—	—	—	—	—
Cr	2.79	—	6.49	14.7	—	—	—	—	—	0.933
Co	—	—	—	—	—	—	—	—	—	—
Ni	—	—	0.317	—	—	—	—	—	—	—
Cu	50.2	134	—	—	—	—	—	63.9	—	—
Zn	6.99	6.52	9.37	14.0	11.8	12.2	14.0	6.71	12.2	9.35
Ga	30.4	27.3	30.7	30.8	30.9	28.8	32.4	31.2	30.6	31.5
Rb	0.237	0.794	0.127	—	—	0.714	0.307	—	0.331	—
Sr	1170	1300	1310	1320	1380	1390	1420	1440	1420	1450
Y	0.305	0.249	0.255	0.232	0.232	0.253	0.236	0.243	0.252	0.259
Zr	—	—	—	—	—	—	—	—	—	—
Nb	—	—	—	—	—	—	—	—	—	—
Cs	—	—	0.119	0.234	—	—	0.969	0.324	—	—
Ba	11.7	76.6	170	223	248	254	276	257	312	269
La	0.127	2.39	4.02	2.66	1.98	2.80	2.74	2.87	1.85	2.82
Ce	0.379	1.92	4.02	3.38	1.84	2.67	2.44	2.56	1.97	3.22
Pr	0.0585	0.0565	0.229	0.171	0.102	0.145	0.128	0.119	0.134	0.240
Nd	0.185	0.165	0.323	0.247	0.241	0.271	0.226	0.356	0.235	0.227
Sm	—	—	—	—	—	—	—	—	—	—
Eu	0.177	0.733	0.717	0.683	0.569	0.730	0.698	0.647	0.676	0.732
Gd	—	—	—	—	—	—	—	—	—	—
Tb	—	—	—	—	—	—	—	—	—	—
Dy	—	—	—	—	—	—	—	—	—	—
Ho	—	—	—	—	—	—	—	—	—	—
Er	—	—	—	—	—	—	—	—	—	—
Tm	—	—	—	—	—	—	—	—	—	—
Yb	—	—	—	—	—	—	—	—	—	—
Lu	—	—	—	—	—	—	—	—	—	—
Hf	—	—	—	—	—	—	—	—	—	—
Ta	—	—	—	—	—	—	—	—	—	—
W	—	—	—	—	—	—	—	—	—	—
Tl	—	—	—	—	—	—	—	—	—	—
Pb	17.5	8.42	9.16	11.3	10.8	12.6	14.0	11.2	10.9	10.3
Th	—	—	—	—	—	—	—	—	—	—
U	—	—	—	—	—	—	—	—	—	—

Table S11: Major and trace element compositions of alkali feldspar. Oxides are in wt%, trace elements are in μg/g.

	AfsA-01	AfsA-02	AfsA-03	AfsA-04	AfsA-05	AfsA-06	AfsA-07	AfsA-08	AfsA-09	AfsA-10
SiO$_2$	63.68	63.85	64.21	64.02	63.82	64.19	64.91	64.41	63.81	64.37
TiO$_2$	0.02	0.00	—	—	0.00	—	0.00	—	0.00	0.00
Al$_2$O$_3$	19.30	19.27	19.26	19.35	19.44	19.18	18.96	19.57	19.98	19.37
FeO	0.01	0.01	0.01	0.01	0.01	0.01	0.01	0.01	0.01	0.01
MnO	0.00	0.00	0.00	0.00	0.00	0.00	0.00	0.00	0.00	0.00
MgO	—	—	—	—	0.00	0.00	—	—	0.00	0.00
CaO	0.03	0.03	0.14	0.07	0.03	0.04	0.09	0.05	0.05	0.09
Na$_2$O	0.70	0.81	1.03	0.94	0.92	1.02	1.04	—	1.04	1.10
K$_2$O	15.42	15.16	14.53	14.76	14.97	14.65	14.12	15.03	14.29	14.23
P$_2$O$_5$	0.29	0.28	0.31	0.26	0.28	0.33	0.25	0.26	0.28	0.27
Li	—	—	—	—	—	—	—	—	—	—
Sc	—	—	6.41	—	1.55	—	19.7	—	2.06	3.95
V	—	—	—	—	—	—	—	—	—	—
Cr	—	—	7.54	3.80	0.271	—	2.46	—	—	0.889
Co	—	—	—	—	—	—	—	—	—	—
Ni	—	—	—	—	—	—	—	—	—	—
Cu	—	43.4	—	—	40.3	—	138	224	36.2	36.5
Zn	2.81	1.80	—	—	0.932	—	—	2.57	—	2.27
Ga	66.4	67.0	62.5	70.7	65.2	67.8	71.5	75.2	62.1	67.0
Rb	295	288	283	284	282	267	273	291	293	274
Sr	1010	1270	891	1060	989	1010	1030	1130	926	924
Y	0.313	0.253	0.268	0.260	0.255	0.254	0.251	0.269	0.247	—
Zr	—	—	—	—	—	—	—	—	—	—
Nb	—	—	—	—	—	—	—	—	—	—
Cs	7.05	5.62	6.03	5.85	5.71	5.56	5.53	4.98	5.64	5.33
Ba	3420	3400	3150	3770	3320	3630	3750	4040	3420	3630
La	0.628	0.609	0.474	0.754	0.603	0.760	0.863	8.72	0.907	0.858
Ce	0.228	0.100	0.0663	—	—	0.0616	—	5.43	0.0671	—
Pr	0.0120	—	—	—	—	—	—	0.202	—	—
Nd	0.162	—	—	—	—	—	—	0.408	—	—
Sm	0.0145	—	—	—	—	—	—	—	—	—
Eu	0.758	0.620	0.502	0.761	0.772	0.646	0.607	0.734	0.465	0.641
Gd	—	—	0.0224	—	—	—	—	—	—	—
Tb	—	—	—	—	—	—	—	—	—	—
Dy	—	—	—	—	—	—	—	—	—	—
Ho	—	—	—	—	—	—	—	—	—	—
Er	—	—	—	—	—	—	—	—	—	—
Tm	—	—	—	—	—	—	—	—	—	—
Yb	—	—	—	—	—	—	—	—	—	—
Lu	—	—	—	—	—	—	—	—	—	—
Hf	—	—	—	—	—	—	—	—	—	—
Ta	0.00797	0.0112	0.00644	0.0108	—	0.00857	0.00807	0.00226	0.0103	0.00267
W	—	—	—	—	—	—	—	—	—	—
Tl	1.64	1.27	1.25	1.21	1.25	1.17	1.29	1.05	1.36	1.21
Pb	37.8	47.0	32.7	40.9	36.7	33.1	37.9	40.3	32.6	34.8
Th	—	—	—	—	—	—	—	—	—	—
U	—	—	—	—	—	—	—	0.00377	—	—

Table S12: Major and trace element compositions of alkali feldspar. Oxides are in wt%, trace elements are in μg/g.

	AfsA-11	AfsA-12	AfsA-13	AfsA-14	AfsA-15	AfsA-16	AfsA-17	AfsA-18	AfsA-19	AfsA-20
SiO_2	64.13	63.85	64.12	63.94	63.86	63.93	63.89	63.63	63.24	63.36
TiO_2	0.00	0.00	—	0.00	0.01	0.00	0.00	0.00	0.00	—
Al_2O_3	19.17	19.47	19.49	19.84	19.78	19.99	19.88	20.23	20.23	20.22
FeO	0.01	0.01	0.01	0.01	0.01	0.01	0.01	0.01	0.01	0.01
MnO	—	—	0.00	0.00	0.00	0.00	0.00	0.00	0.00	0.00
MgO	0.00	0.00	0.00	0.00	0.00	—	0.00	0.00	0.00	0.00
CaO	0.06	0.06	0.05	0.11	0.12	0.13	0.07	0.15	0.08	0.06
Na_2O	0.88	1.01	0.83	1.03	1.02	1.10	0.97	1.07	1.05	1.01
K_2O	14.88	14.69	14.58	14.22	14.42	14.10	14.38	14.14	14.48	14.45
P_2O_5	0.26	0.25	0.27	0.27	0.23	0.21	0.26	0.25	0.27	0.23
Li	—	—	—	—	—	—	—	—	—	—
Sc	—	—	15.2	1.88	4.01	7.91	1.41	—	—	43.8
V	—	—	—	—	—	—	0.11	—	—	—
Cr	—	—	—	2.50	—	—	—	0.376	—	10.1
Co	—	—	—	—	—	—	—	—	—	—
Ni	—	—	—	—	—	—	—	—	—	—
Cu	24.3	92.3	309	22.8	—	—	62.2	13.1	180	—
Zn	0.373	5.90	—	1.40	1.60	—	—	0.331	—	—
Ga	71.9	75.3	69.8	70.9	64.6	61.8	60.2	59.3	71.2	76.5
Rb	283	282	299	272	280	286	286	287	282	294
Sr	1080	1050	1090	991	1010	948	1000	972	969	1040
Y	0.261	—	—	0.260	0.261	0.255	—	0.259	0.257	0.256
Zr	—	—	—	—	—	—	—	—	—	—
Nb	—	—	—	—	—	—	—	—	—	—
Cs	5.15	5.00	5.81	4.81	5.08	5.59	5.40	5.38	5.10	8.04
Ba	3970	4140	3840	3690	3520	3320	3260	3240	4080	4370
La	0.840	0.920	0.814	0.654	1.93	1.81	0.608	0.690	0.763	1.09
Ce	—	—	—	—	0.481	0.466	—	—	—	0.0688
Pr	—	—	—	—	0.0177	0.0318	—	—	—	—
Nd	—	—	—	—	0.0795	—	—	—	—	—
Sm	—	—	—	—	—	—	—	—	—	—
Eu	0.399	0.468	0.315	0.322	0.310	0.300	0.186	0.218	0.445	0.669
Gd	—	—	—	—	—	—	—	—	—	—
Tb	—	—	—	—	—	—	—	—	—	—
Dy	—	—	—	—	—	—	—	—	—	—
Ho	—	—	—	—	—	—	—	—	—	—
Er	—	—	—	—	—	—	—	—	—	—
Tm	—	—	—	—	—	—	—	—	—	—
Yb	—	—	—	—	—	—	—	—	—	—
Lu	—	—	—	—	—	—	—	—	—	—
Hf	—	—	—	—	—	—	—	—	—	—
Ta	0.0139	0.0117	0.0207	0.00252	0.0144	0.0132	—	0.0128	—	0.00940
W	—	—	—	—	—	—	—	—	—	—
Tl	1.10	1.19	1.10	1.16	1.28	1.10	1.24	1.20	1.18	1.24
Pb	36.2	35.9	38.2	34.1	36.5	38.3	36.4	35.5	36.4	39.1
Th	—	—	—	—	—	—	—	—	—	—
U	—	—	—	—	—	—	—	—	—	—

Table S13: Crystallization temperature of titanite estimated from the Zr-in-titanite thermometry (Hayden et al., 2008).

| | | $a_{TiO_2} = 1$ | | $a_{TiO_2} = 0.5$ | |
	Zr (μg/g)	0.4 GPa	0.7 GPa	0.4 GPa	0.7 GPa
TtnA-01	656	780	810	740	770
TtnA-03	940	800	840	760	790
TtnA-04	674	780	820	740	780
TtnA-05	639	780	810	740	770
TtnA-06	645	780	810	740	770
TtnA-07	808	790	830	750	790
TtnA-08	821	790	830	750	790
TtnA-09	832	790	830	750	790
TtnA-10	678	780	820	740	780
TtnA-11	781	790	830	750	780
TtnA-12	772	790	820	750	780
TtnA-13	799	790	830	750	790
TtnA-14	720	780	820	740	780
TtnA-15	790	790	830	750	780
TtnA-16	816	790	830	750	790
TtnA-18	686	780	820	740	780
TtnA-19	719	780	820	740	780
TtnA-20	733	780	820	740	780
TtnA-21	735	780	820	740	780
TtnA-22	746	790	820	750	780
TtnA-23	698	780	820	740	780
TtnA-24	628	770	810	740	770
TtnA-25	633	780	810	740	770
TtnA-26	687	780	820	740	780
TtnA-27	674	780	820	740	780
TtnA-28	993	800	840	760	800
TtnA-29	669	780	820	740	780
TtnA-30	651	780	810	740	770
TtnA-31	537	770	800	730	760
TtnA-32	906	800	840	760	790
TtnA-33	1010	800	840	760	800
TtnA-34	844	790	830	750	790
TtnA-35	934	800	840	760	790
TtnA-36	769	790	820	750	780
TtnA-37	796	790	830	750	790
TtnA-38	813	790	830	750	790
TtnA-39	1020	800	840	760	800
TtnA-40	1010	800	840	760	800
TtnA-41	895	800	830	760	790
TtnA-42	924	800	840	760	790
TtnA-43	939	800	840	760	790
TtnA-44	914	800	840	760	790
TtnA-45	921	800	840	760	790
TtnA-46	861	790	830	750	790
TtnA-47	783	790	830	750	780
TtnA-48	832	790	830	750	790
TtnA-49	718	780	820	740	780
TtnA-52	759	790	820	750	780
TtnA-53	763	790	820	750	780
TtnA-54	799	790	830	750	790
TtnA-55	667	780	820	740	770
TtnA-56	645	780	810	740	770

Table S14: Crystallization temperature of titanite estimated from the Zr-in-titanite thermometry (Hayden et al., 2008).

| | Zr (μg/g) | $a_{TiO_2} = 1$ | | $a_{TiO_2} = 0.5$ | |
		0.4 GPa	0.7 GPa	0.4 GPa	0.7 GPa
TtnB-01	586	770	810	730	770
TtnB-02	840	790	830	750	790
TtnB-03	657	780	810	740	770
TtnB-04	640	780	810	740	770
TtnB-05	778	790	830	750	780
TtnB-06	705	780	820	740	780
TtnB-07	765	790	820	750	780
TtnB-08	752	790	820	750	780
TtnB-09	823	790	830	750	790
TtnB-10	907	800	840	760	790
TtnB-11	869	790	830	750	790
TtnB-12	870	790	830	750	790
TtnB-13	722	780	820	740	780
TtnB-14	671	780	820	740	780
TtnB-15	653	780	810	740	770
TtnB-16	699	780	820	740	780
TtnB-17	732	780	820	740	780
TtnB-18	729	780	820	740	780
TtnB-19	691	780	820	740	780
TtnB-20	753	790	820	750	780
TtnB-21	796	790	830	750	790
TtnB-22	649	780	810	740	770
TtnB-23	1050	810	840	760	800
TtnB-24	1130	810	850	770	810
TtnB-25	964	800	840	760	800
TtnB-26	852	790	830	750	790
TtnB-27	822	790	830	750	790
TtnB-28	793	790	830	750	780
TtnB-29	933	800	840	760	790
TtnB-30	870	790	830	750	790
TtnB-31	697	780	820	740	780

Reference

Figure 2

Hida Belt

Cho, D. L., Lee, T. H., Takahashi, Y., Kato, T., Yi, K., Lee, S., Cheong, A. C. S. 2021. Zircon U–Pb geochronology and Hf isotope geochemistry of magmatic and metamorphic rocks from the Hida Belt, southwest Japan. Geoscience Frontiers, 12, 101145.

Harada, H., Tsujimori, T., Kunugiza, K., Yamashita, K., Aoki, S., Aoki, K., Takayanagi, H., Iryu, Y. 2021. The $\delta^{13}C$–$\delta^{18}O$ variations in marble in the Hida Belt, Japan. Island Arc, 30, e12389.

Horie, K., Takehara, M., Suda, Y., Hidaka, H. 2013. Potential Mesozoic reference zircon from the Unazuki plutonic complex: geochronological and geochemical characterization. Island Arc, 22, 292–305.

Horie, K., Tsutsumi, Y., Cho, M., Morishita, Y., Hidaka, H. 2010. Crystallization of REE minerals and redistribution of U, Th, and REE at contact boundary between granite and gabbro during hydrothermal alteration. Physics and Chemistry of the Earth, Parts A/B/C, 35, 284–291.

Horie, K., Tsutsumi, Y., Takehara, M., Hidaka, H. 2018. Timing and duration of regional metamorphism in the Kagasawa and Unazuki areas, Hida metamorphic complex, southwest Japan. Chemical Geology, 484, 148–167.

Horie, K., Yamashita, M., Hayasaka, Y., Katoh, Y., Tsutsumi, Y., Katsube, A., Hidaka, H., Kim, H., Cho, M. 2010. Eoarchean–Paleoproterozoic zircon inheritance in Japanese Permo-Triassic granites (Unazuki area, Hida Metamorphic Complex): Unearthing more old crust and identifying source terrranes. Precambrian Research, 183, 145–157.

25   Koizumi, S., Otoh, S. 2020. The Permian–Triassic plutonic and metamorphic rocks in the

26   Saragawa–Bandojima area, Katsuyama City, Fukui Prefecture, central Japan.

27   Katsuyama City Geopark Academic Research Encouragement Project Academic

28   Research Report, pp18 (in Japanese with English abstract).

29   Sakoda, M., Kano, T., Fanning, C. M., Sakaguchi, T. 2006. SHRIMP U−Pb zircon age of the

30   Inishi migmatite around the Kamioka mining area, Hida metamorphic complex, Central

31   Japan. Resource Geology, 56, 17−26.

32   Sano, Y., Hidaka, H., Terada, K., Shimizu, H., Suzuki, M. 2000. Ion microprobe U–Pb zircon

33   geochronology of the Hida gneiss: Finding of the oldest minerals in

34   Japan. Geochemical Journal, 34, 135–153.

35   Takahashi, Y., Cho, D. L., Kee, W. S. 2010. Timing of mylonitization in the Funatsu shear

36   zone within Hida Belt of southwest Japan: Implications for correlation with the shear

37   zones around the Ogcheon Belt in the Korean Peninsula. Gondwana Research, 17, 102–

38   115.

39   Takahashi, Y., Cho, D. L., Mao, J., Zhao, X., Yi, K. 2018. SHRIMP U–Pb zircon ages of the

40   Hida metamorphic and plutonic rocks, Japan: Implications for late Paleozoic to

41   Mesozoic tectonics around the Korean Peninsula. Island Arc, 27, e12220.

42   Takehara, M., Horie, K. 2019. U–Pb zircon geochronology of the Hida gneiss and granites in

43   the Kamioka area, Hida Belt. Island Arc, 28, e12303.

44   Takeuchi, M., Shibata, K., Jia, S., Yamamoto, K. 2019. U–Pb zircon ages of granitic rocks

45   from Kagasawa, Hida Mountains. The Journal of Geological Society of Japan, 125,

46   453–459 (in Japanese with English abstract).

47   Zhao, X., Mao, J., Ye, H., Liu, K., Takahashi, Y. 2013. New SHRIMP U–Pb zircon ages of

48   granitic rocks in the Hida Belt, Japan: Implications for tectonic correlation with

49   Jiamushi massif. Island Arc, 22, 508–521.

50

51

Far Eastern Russia

Khanka terrane

Han, S., Yang, Y., Bo, J., Zhang, G., Khomich, V. G., Huang, Y., Yang, Y. Wang, X. 2020. Late Neoarchean magmatic record of the Jiamusi–Khanka Block, Northeast China: New clues from amphibolite zircon U–Pb geochronology and Lu–Hf isotopes. Geological Journal, 55, 3401–3415.

Khanchuk, A. I., Sakhno, V. G., Alenicheva, A. A. 2010. First SHRIMP U–Pb zircon dating of magmatic complexes in the southwestern Primor'e region. Doklady Earth Sciences, 431, 424–428.

Khanchuk, A. I., Vovna, G. M., Kiselev, V. I., Mishkin, M. A., Lavrik, S. N. 2010. First results of zircon LA-ICP-MS U–Pb dating of the rocks from the Granulite complex of Khanka massif in the Primorye region. Doklady Earth Sciences, 434, 1164–1167.

Tsutsumi, Y., Yokoyama, K., Kasatkin, S. A., Golozubov, V. V. 2014. Zircon U–Pb age of granitoids in the Maizuru Belt, southwest Japan and the southernmost Khanka Massif, Far East Russia. Journal of Mineralogical and Petrological Sciences, 109, 97–102.

Xu, T., Xu, W. L., Wang, F., Ge, W. C., Sorokin, A. A. 2018. Geochronology and geochemistry of early Paleozoic intrusive rocks from the Khanka Massif in the Russian Far East: Petrogenesis and tectonic implications. Lithos, 300–301, 105–120.

Yang, H., Ge, W., Zhao, G., Yu, J., Zhang, Y. 2015. Early Permian–Late Triassic granitic magmatism in the Jiamusi–Khanka Massif, eastern segment of the Central Asian Orogenic Belt and its implications. Gondwana Research, 27, 1509–1533.

73   Zhou, J. B., Wilde, S. A., Zhao, G. C., Zhang, X. Z., Zheng, C. Q., Wang, H., Zeng, W. S.

74   2010. Pan-African metamorphic and magmatic rocks of the Khanka Massif, NE China:

75   further evidence regarding their affinity. Geological Magazine, 147, 737–749.

76

77   *Bureya terrane*

78   Dong, Y., He, Z. H., Ren, Z. H., Ge, W. C., Yang, H., Ji, Z., He, Y. 2018. Formation of the

79   Permian Taipinggou igneous rocks, north of Luobei (Northeast China): implications for

80   the subduction of the Mudanjiang Ocean beneath the Bureya–Jiamusi Massif.

81   International Geology Review, 60, 1195-1212.

82   Sorokin, A. A., Ovchinnikov, R. O., Xu, W., Kovach, V. P., Yang, H., Kotov, A. B.,

83   Ponomarchuk, V. A., Travin, A. V., Plotkina, Y. V. 2019. Ages and nature of the

84   protolith of the Tulovchikha metamorphic complex in the Bureya Massif, Central Asian

85   orogenic belt, Russia: evidence from U–Th–Pb, Lu–Hf, Sm–Nd, and $^{40}Ar/^{39}Ar$ data.

86   Lithos, 332–333, 340–354.

87

88   *Jiamusi terrane*

89   Bi, J. H., Ge, W. C., Yang, H., Zhao, G. C., Xu, W. L., Wang, Z. H. 2015. Geochronology,

90   geochemistry and zircon Hf isotopes of the Dongfanghong gabbroic complex at the

91   eastern margin of the Jiamusi Massif, NE China: Petrogensis and tectonic implications.

92   Lithos, 234–235, 27–46.

93   Bi, J. H., Ge, W. C., Yang, H., Wang, Z. H., Xu, W. L., Yang, J. H., Xing, D. H. Chen, H. J.

94   2016. Geochronology and geochemistry of late Carboniferous–middle Permian I-and

95   A-type granites and gabbro–diorites in the eastern Jiamusi Massif, NE China:

96   Implications for petrogenesis and tectonic setting. Lithos, 266–267, 213–232.

97   Cui, P. L., Sun, J. G., Han, S. J., Zhang, P., Zhang, Y., Bai, L. A., Gu, A. L. 2013. Zircon U–

98   Pb–Hf isotopes and bulk-rock geochemistry of gneissic granites in the northern Jiamusi

99   Massif, Central Asian Orogenic Belt: implications for Middle Permian collisional

100   orogeny and Mesoproterozoic crustal evolution. International Geology Review, 55,

101   1109–1125.

102   Wilde, S. A., Wu, F., Zhang, X. 2003. Late Pan-African magmatism in northeastern China:

103   SHRIMP U–Pb zircon evidence from granitoids in the Jiamusi Massif. Precambrian

104   Research, 122, 311–327.

105   Yang, H., Ge, W. C., Bi, J. H., Wang, Z. H., Tian, D. X., Dong, Y., Chen, H. J. 2018. The

106   Neoproterozoic-early Paleozoic evolution of the Jiamusi Block, NE China and its East

107   Gondwana connection: Geochemical and zircon U–Pb–Hf isotopic constraints from the

108   Mashan Complex. Gondwana Research, 54, 102–121.

109   Yang, H., Ge, W. C., Dong, Y., Bi, J. H., Wang, Z., Ji, Z. 2017a. Record of Permian–Early

110   Triassic continental arc magmatism in the western margin of the Jiamusi Block, NE

111   China: Petrogenesis and implications for Paleo-Pacific subduction. International

112   Journal of Earth Sciences, 106, 1919–1942.

113   Yang, H., Ge, W. C., Zhao, G. C., Bi, J. H., Wang, Z. H., Dong, Y., Xu, W. L. 2017. Zircon

114   U–Pb ages and geochemistry of newly discovered Neoproterozoic orthogneisses in the

115   Mishan region, NE China: Constraints on the high-grade metamorphism and tectonic

116   affinity of the Jiamusi–Khanka Block. Lithos, 268–271, 16–31.

117   Yang, H., Ge, W. C., Zhao, G. C., Dong, Y., Bi, J. H., Wang, Z. H., Yu, J. J., Zhang, Y. L.

118   2014. Geochronology and geochemistry of Late Pan-African intrusive rocks in the

119   Jiamusi–Khanka Block, NE China: petrogenesis and geodynamic implications. Lithos,

120   208–209, 220–236.

121 Yang, H., Ge, W. C., Zhao, G. C., Yu, J., Zhang, Y. 2015. Early Permian–Late Triassic

122   granitic magmatism in the Jiamusi–Khanka Massif, eastern segment of the Central

123   Asian Orogenic Belt and its implications. Gondwana Research, 27, 1509–1533.

124

125

126 **North China Craton**

127 *Ordos Block*

128 Hu, J. M., Liu, X. S., Li, Z. H., Zhao, Y., Zhang, S. H., Liu, X. C., Qu, H. J., Chen, H. 2013.

129   SHRIMP U–Pb zircon dating of the Ordos Basin basement and its tectonic significance.

130   Chinese Science Bulletin, 58, 118–127.

131 Wan, Y., Xie, H., Yang, H., Wang, Z., Liu, D., Kröner, A., Wilde, S. A., Geng, Y., Sun, L.,

132   Ma, M., Liu, S., Dong, C., Du, L. 2013. Is the Ordos block Archean or

133   Paleoproterozoic in age? Implications for the Precambrian evolution of the North China

134   Craton. American Journal of Science, 313, 683–711.

135 Wang, W., Zhao, Y., Liu, X., Hu, J., Wei, C., Xiao, W., Du, J., Wang, S., Zhan, L. 2019.

136   Metamorphism of diverse basement gneisses of the Ordos Basin: Record of multistage

137   Paleoproterozoic orogenesis and constraints on the evolution of the western North

138   China Craton. Precambrian Research, 328, 48–63.

139 Zhang, C., Diwu, C., Kröner, A., Sun, Y., Luo, J., Li, Q., Gou, L., Lin, H., Wei, X. Zhao, J.

140   2015. Archean-Paleoproterozoic crustal evolution of the Ordos Block in the North

141   China Craton: Constraints from zircon U–Pb geochronology and Hf isotopes for

142   gneissic granitoids of the basement. Precambrian Research, 267, 121–136.

143

144 *Yinshan Block*

145 Dong, X. J., Xu, Z. Y., Liu, Z. H., Sha, Q. 2012. Zircon U–Pb geochronology of Archean

146   high-grade metamorphic rocks from Xi Ulanbulang area, central Inner Mongolia.

147   Science China Earth Sciences, 55, 204–212.

148 Jian, P., Kröner, A., Windley, B. F., Zhang, Q., Zhang, W., Zhang, L. 2012. Episodic mantle

149   melting-crustal reworking in the late Neoarchean of the northwestern North China

150   Craton: Zircon ages of magmatic and metamorphic rocks from the Yinshan Block.

151   Precambrian Research, 222–223, 230–254.

152 Ma, X., Fan, H. R., Santosh, M., Guo, J. 2014. Chronology and geochemistry of Neoarchean

153   BIF-type iron deposits in the Yinshan Block, North China Craton: Implications for

154   oceanic ridge subduction. Ore Geology Reviews, 63, 405–417.

155 Ma, X., Guo, J., Liu, F., Qian, Q., Fan, H. 2013. Zircon U–Pb ages, trace elements and Nd–

156   Hf isotopic geochemistry of Guyang sanukitoids and related rocks: Implications for the

157   Archean crustal evolution of the Yinshan Block, North China Craton. Precambrian

158   Research, 230, 61–78.

159 Ma, X., Zhong, Y. 2018. Geochemistry and chronology of a diorite pluton in the Yinshan

160   Block, implications for crustal growth and evolution of North China Craton. Geological

161   Journal, 53, 2849–2862.

162 Ouyang, D., Guo, J., Liou, P., Huang, G. 2020. Petrogenesis and tectonic implications of 2.45

163   Ga potassic A-type granite in the Daqingshan area, Yinshan Block, North China

164   Craton. Precambrian Research, 336, 105435.

165

166 *Khondalite Belt*

167 Dong, C. Y., Wan, Y. S., Wilde, S. A., Xu, Z. Y., Ma, M. Z., Xie, H. Q., Liu, D. 2014.

168   Earliest Paleoproterozoic supracrustal rocks in the North China Craton recognized from

169   the Daqingshan area of the Khondalite Belt: Constraints on craton evolution.

170   Gondwana Research, 25, 1535–1553.

171   Dong, C. Y., Wan, Y. S., Xu, Z. Y., Liu, D., Yang, Z. S., Ma, M. Z., Xie, H. Q. 2013.

172   SHRIMP zircon U–Pb dating of late Paleoproterozoic kondalites in the Daqing

173   Mountains area on the North China Craton. Science China Earth Sciences, 56, 115–

174   125.

175   Gou, L., Zi, J. W., Dong, Y., Liu, X., Li, Z., Xu, X., Zhang, C., Liu, L., Long, X., Zhao, Y.

176   2019. Timing of two separate granulite-facies metamorphic events in the Helanshan

177   complex, North China Craton: Constraints from monazite and zircon U–Pb dating of

178   pelitic granulites. Lithos, 350–351, 105216.

179   Li, X. P., Yang, Z., Zhao, G., Grapes, R., Guo, J. 2011. Geochronology of khondalite-series

180   rocks of the Jining Complex: confirmation of depositional age and tectonometamorphic

181   evolution of the North China craton. International Geology Review, 53, 1194–1211

182   Liu, S. J., Dong, C. Y., Xu, Z. Y., Santosh, M., Ma, M. Z., Xie, H. Q., Liu, D. Wan, Y. S.

183   2013. Palaeoproterozoic episodic magmatism and high-grade metamorphism in the

184   North China Craton: evidence from SHRIMP zircon dating of magmatic suites in the

185   Daqingshan area. Geological Journal, 48, 429–455.

186   Ma, M. Z., Wan, Y. S., Santosh, M., Xu, Z. Y., Xie, H. Q., Dong, C. Y., Liu, D. Guo, C.

187   2012. Decoding multiple tectonothermal events in zircons from single rock samples:

188   SHRIMP zircon U–Pb data from the late Neoarchean rocks of Daqingshan, North

189   China Craton. Gondwana Research, 22, 810–827.

190   Santosh, M., Wilde, S. A., Li, J. H. 2007. Timing of Paleoproterozoic ultrahigh-temperature

191   metamorphism in the North China Craton: evidence from SHRIMP U–Pb zircon

192   geochronology. Precambrian Research, 159, 178–196.

193   Wan, Y., Song, B., Liu, D., Wilde, S. A., Wu, J., Shi, Y., Yin, X. Zhou, H. 2006. SHRIMP

194   U–Pb zircon geochronology of Palaeoproterozoic metasedimentary rocks in the North

195   China Craton: evidence for a major Late Palaeoproterozoic tectonothermal event.

196   Precambrian Research, 149, 249–271.

197   Wan, Y., Xu, Z., Dong, C., Nutman, A., Ma, M., Xie, H., Liu, S., Liu, D., Wang, H., Cu, H.

198   2013. Episodic Paleoproterozoic (∼2.45, ∼1.95 and ∼1.85 Ga) mafic magmatism and

199   associated high temperature metamorphism in the Daqingshan area, North China

200   Craton: SHRIMP zircon U–Pb dating and whole-rock geochemistry. Precambrian

201   Research, 224, 71–93.

202   Wang, W., Gao, S., Liu, X., Hu, J., Zhao, Y., Wei, C., Xiao, W., Guo, H., Gong, W. 2017.

203   Prolonged anatexis of Paleoproterozoic metasedimentary basement: First evidence from

204   the Yinchuan Basin and new constraints on the evolution of the Khondalite Belt, North

205   China Craton. Precambrian Research, 302, 74–93.

206   Wang, X., Li, X. P., Zhang, J., Schertl, H. P. 2020. Geochemistry, geochronology and

207   evolution of Paleoproterozoic granitoid gneisses in the Khondalite Belt, North China

208   Craton. Precambrian Research, 338, 105590.

209

210   *Trans-North China Orogen*

211   Liao, Y., Wei, C. 2019. Ultrahigh-temperature mafic granulite in the Huai'an Complex, North

212   China Craton: Evidence from phase equilibria modelling and amphibole thermometers.

213   Gondwana Research, 76, 62–76.

214   Liu, H., Li, X. P., Kong, F. M., Santosh, M., Wang, H. 2019. Ultra-high temperature

215   overprinting of high pressure pelitic granulites in the Huai'an complex, North China

216   Craton: Evidence from thermodynamic modeling and isotope geochronology.

217   Gondwana Research, 72, 15–33.

218 Liu, S., Zhang, J., Li, Q., Zhang, L., Wang, W., Yang, P. 2012. Geochemistry and U–Pb

219   zircon ages of metamorphic volcanic rocks of the Paleoproterozoic Lüliang Complex

220   and constraints on the evolution of the Trans-North China Orogen, North China Craton.

221   Precambrian Research, 222–223, 173–190.

222 Wang, J., Yang, C., Wyman, D. A., Song, H., Du, L. 2020. Petrogenesis and tectonic

223   implications of the 2.1–2.0 Ga granitoids in Fuping Complex, North China Craton:

224   Constraints from petrology, geochemistry and zircon U–Pb–Hf isotopes. Precambrian

225   Research, 339, 105611.

226 Zhao, D., Sun, M., Ding, A. 2020. Zircon U–Pb ages and Hf isotopes of the Huai'an gneisses

227   from the Tianzhen-Xinpingbu area: Implications for the tectonic evolution of the Trans-

228   North China Orogen. Precambrian Research, 337, 105530.

229 Zhao, G., Wilde, S. A., Cawood, P. A., Sun, M. 2002. SHRIMP U–Pb zircon ages of the

230   Fuping Complex: implications for late Archean to Paleoproterozoic accretion and

231   assembly of the North China Craton. American Journal of Science, 302, 191–226.

232 Zhao, G., Wilde, S. A., Sun, M., Li, S., Li, X., Zhang, J. 2008. SHRIMP U–Pb zircon ages of

233   granitoid rocks in the Lüliang Complex: implications for the accretion and evolution of

234   the Trans-North China Orogen. Precambrian Research, 160, 213–226.

235

236 *Eastern Block*

237 Chen, Y., Zhang, J., Liu, J., Han, Y., Yin, C., Qian, J., Liu, X. 2020. Crustal growth and

238   reworking of the eastern North China Craton: Constraints from the age and

239   geochemistry of the Neoarchean Taishan TTG gneisses. Precambrian Research, 343,

240   105706.

241 Geng, Y., Liu, F., Yang, C. 2006. Magmatic event at the end of the Archean in eastern Hebei

242   Province and its geological implication. Acta Geologica Sinica, 80, 819–833.

243   Han, Y. S., Santosh, M., Samuel, V. O. 2018. The Fangmayu Alaskan-type ultramafic

244   intrusion: Implications for Paleoproterozoic assembly of the North China Craton.

245   Precambrian Research, 315, 201–221.

246   Liu, D. Y., Nutman, A. P., Compston, W., Wu, J. S., Shen, Q. H. 1992. Remnants of ≥ 3800

247   Ma crust in the Chinese part of the Sino-Korean craton. Geology, 20, 339–342.

248   Liu, D., Wilde, S. A., Wan, Y., Wu, J., Zhou, H., Dong, C., Yin, X. 2008. New U–Pb and Hf

249   isotopic data confirm Anshan as the oldest preserved segment of the North China

250   Craton. American Journal of Science, 308, 200–231.

251   Nutman, A. P., Wan, Y., Du, L., Friend, C. R. L., Dong, C., Xie, H., Wang, W., Sun, H. Liu,

252   D. 2011. Multistage late Neoarchaean crustal evolution of the North China Craton,

253   eastern Hebei. Precambrian Research, 189, 43–65.

254   Shi, Y., Zhao, X. 2017. Early Neoarchean magmatic and Paleoproterozoic metamorphic

255   events in the northern North China Craton: SHRIMP zircon dating and Hf isotopes of

256   Archean rocks from the Miyun area, Beijing. Acta Geologica Sinica, 91, 988–1002.

257   Song, B., Nutman, A. P., Liu, D., Wu, J. 1996. 3800 to 2500 Ma crustal evolution in the

258   Anshan area of Liaoning Province, northeastern China. Precambrian Research, 78, 79–

259   94.

260   Wan, Y., Dong, C., Liu, D., Kröner, A., Yang, C., Wang, W., Du, L., Xie, H., Ma, M. 2012.

261   Zircon ages and geochemistry of late Neoarchean syenogranites in the North China

262   Craton: a review. Precambrian Research, 222–223, 265–289.

263   Wan, Y., Liu, D., Nutman, A., Zhou, H., Dong, C., Yin, X., Ma, M. 2012. Multiple 3.8–3.1

264   Ga tectono-magmatic events in a newly discovered area of ancient rocks (the Shengousi

265   Complex), Anshan, North China Craton. Journal of Asian Earth Sciences, 54–55, 18–

266   30.

267   Wang, Y. F., Li, X. H., Jin, W., Zhang, J. H. 2015. Eoarchean ultra-depleted mantle domains

268   inferred from ca. 3.81 Ga Anshan trondhjemitic gneisses, North China Craton.

269   Precambrian Research, 263, 88–107.

270   Wu, F. Y., Zhang, Y. B., Yang, J. H., Xie, L. W., Yang, Y. H. 2008. Zircon U–Pb and Hf

271   isotopic constraints on the Early Archean crustal evolution in Anshan of the North

272   China Craton. Precambrian Research, 167, 339–362.

273   Yang, J. H., Wu, F. Y., Wilde, S. A., Zhao, G. 2008. Petrogenesis and geodynamics of Late

274   Archean magmatism in eastern Hebei, eastern North China Craton: geochronological,

275   geochemical and Nd–Hf isotopic evidence. Precambrian Research, 167, 125–149.

276   Zhang, H. C. G., Peng, T., Liu, J. H., Wang, J., Chen, Y. C., Zhang, Q. W. L., Wu, C. M.

277   2020. New geochronological evidences of late Neoarchean and late Paleoproterozoic

278   tectono-metamorphic events in the Miyun area, North China Craton. Precambrian

279   Research, 345, 105774.

280

281   *Jiao-Liao-Ji Belt*

282   Cai, J., Liu, F., Liu, P., Wang, F. 2020. Metamorphic *P–T* evolution and tectonic implications

283   of pelitic granulites in the Ji'an area, northeastern Jiao–Liao–Ji Belt, North China

284   Craton. Journal of Asian Earth Sciences, 191, 104197.

285   Dong, Y., Bi, J. H., Xing, D. H., Ge, W. C., Yang, H., Hao, Y. J., Li, Z., Jing, Y. 2019.

286   Geochronology and geochemistry of Liaohe Group and Liaoji granitoid in the Jiao-

287   Liao-Ji Belt, North China Craton: Implications for petrogenesis and tectonic evolution.

288   Precambrian Research, 332, 105399.

289   Liang, Y., Deng, J., Liu, X., Wang, Q., Ma, Y., Gao, T., Zhao, E., Zhou, Z. 2020.

290   Geochronology and geochemistry of the palaeoproterozoic mafic dikes in the Jiaobei

291   terrane: implications for tectonic evolution of the Jiao-Liao-Ji Belt, eastern North China

292   Craton. International Geology Review, 1–18.

293   Liu, J., Zhang, J., Yin, C., Cheng, C., Liu, X., Zhao, C., Chen, Y., Wang, X. 2020.

294   Synchronous A-type and adakitic granitic magmatism at ca. 2.2 Ga in the Jiao–Liao–Ji

295   belt, North China Craton: Implications for rifting triggered by lithospheric

296   delamination. Precambrian Research, 342, 105629.

297   Lu, X. P., Wu, F. Y., Guo, J. H., Wilde, S. A., Yang, J. H., Liu, X. M., Zhang, X. O. 2006.

298   Zircon U–Pb geochronological constraints on the Paleoproterozoic crustal evolution of

299   the Eastern block in the North China Craton. Precambrian Research, 146, 138–164.

300   Luo, Y., Sun, M., Zhao, G., Li, S., Xu, P., Ye, K., Xia, X. 2004. LA-ICP-MS U–Pb zircon

301   ages of the Liaohe Group in the Eastern Block of the North China Craton: constraints

302   on the evolution of the Jiao-Liao-Ji Belt. Precambrian Research, 134, 349–371.

303   Meng, E., Liu, F. L., Liu, P. H., Liu, C. H., Yang, H., Wang, F., Shi, J. R. Cai, J. 2014.

304   Petrogenesis and tectonic significance of Paleoproterozoic meta-mafic rocks from

305   central Liaodong Peninsula, northeast China: evidence from zircon U–Pb dating and in

306   situ Lu–Hf isotopes, and whole-rock geochemistry. Precambrian Research, 247, 92–

307   109.

308   Tam, P. Y., Zhao, G., Liu, F., Zhou, X., Sun, M., Li, S. 2011. Timing of metamorphism in the

309   Paleoproterozoic Jiao-Liao-Ji Belt: new SHRIMP U–Pb zircon dating of granulites,

310   gneisses and marbles of the Jiaobei massif in the North China Craton. Gondwana

311   Research, 19, 150–162.

312   Wan, Y., Song, B., Liu, D., Wilde, S. A., Wu, J., Shi, Y., Yin, X. Zhou, H. 2006. SHRIMP

313   U–Pb zircon geochronology of Palaeoproterozoic metasedimentary rocks in the North

314   China Craton: evidence for a major Late Palaeoproterozoic tectonothermal event.

315   Precambrian Research, 149, 249–271.

316   Wang, C. Y., Meng, E., Yang, H., Liu, C. H., Cai, J., Ji, L., Li, Y. G. 2018. Geochronological

317   and petrogenetic constraints on the regional tectonic evolution of the Guanghua Group

318   in northeastern Jiao-Liao-Ji Belt, China. Precambrian Research, 305, 427–443.

319   Wang, X., Oh, C. W., Lee, B. C., Liu, F. 2020. Paleoproterozoic postcollisional metamorphic

320   and igneous activities in the Jinan area of the Jiao-Liao-Ji Belt in the North China

321   Craton and their tectonic implications. Precambrian Research, 346, 105793.

322   Wang, X., Peng, P., Wang, C., Yang, S., Söderlund, U., Su, X. 2017. Nature of three episodes

323   of Paleoproterozoic magmatism (2180 Ma, 2115 Ma and 1890 Ma) in the Liaoji belt,

324   North China with implications for tectonic evolution. Precambrian Research, 298, 252–

325   267.

326   Zhu, K., Liu, Z., Xu, Z., Wang, X. A., Cui, W., Hao, Y. 2019. Petrogenesis and tectonic

327   implications of two types of Liaoji granitoid in the Jiao–Liao–Ji Belt, North China

328   Craton. Precambrian Research, 331, 105369.

329

330

331   **South China Craton**

332   *Yangtze Block*

333   Chen, Q., Sun, M., Zhao, G., Zhao, J., Zhu, W., Long, X., Wang, J. 2019. Episodic crustal

334   growth and reworking of the Yudongzi terrane, South China: Constraints from the

335   Archean TTGs and potassic granites and Paleoproterozoic amphibolites. Lithos, 326–

336   327, 1–18.

337   Cui, X., Wang, J., Ren, G., Deng, Q., Sun, Z., Ren, F., Chen, F. 2020. Paleoproterozoic

338   tectonic evolution of the Yangtze Block: New evidence from ca. 2.36 to 2.22 Ga

339   magmatism and 1.96 Ga metamorphism in the Cuoke complex, SW China.

340   Precambrian Research, 337, 105525.

341   Guo, J. L., Gao, S., Wu, Y. B., Li, M., Chen, K., Hu, Z. C., Liang, Z. W., Liu, Y. S., Zhou,

342   L., Zong, K. Q., Zhang, W., Chen, H. H. 2014. 3.45 Ga granitic gneisses from the

343   Yangtze Craton, South China: implications for Early Archean crustal growth.

344   Precambrian Research, 242, 82–95.

345   Guo, J. L., Wu, Y. B., Gao, S., Jin, Z. M., Zong, K. Q., Hu, Z. C., Chen, K., Chen, H. H., Liu,

346   Y. S. 2015. Episodic Paleoarchean-Paleoproterozoic (3.3–2.0 Ga) granitoid magmatism

347   in Yangtze craton, South China: implications for late Archean tectonics. Precambrian

348   Research, 270, 246–266.

349   Hu, J., Liu, X., Qu, W., Chen, L. 2019. Mid-Neoproterozoic amphibolite facies

350   metamorphism at the northern margin of the Yangtze craton. Precambrian Research,

351   326, 333–343.

352   Huang, M., Cui, X., Ren, G., Guo, J., Ren, F., Pang, W., Chen, F. 2020. The 2.73 Ga I-type

353   granites in the Lengshui Complex and implications for the Neoarchean tectonic

354   evolution of the Yangtze Craton. International Geology Review, 62, 649–664.

355   Huang, S. F., Wang, W., Zhao, J. H., Zheng, J. P. 2018. Petrogenesis and geodynamic

356   significance of the ~850 Ma Dongling A-type granites in South China. Lithos, 318–

357   319, 176–193.

358   Wang, K., Li, Z. X., Dong, S., Cui, J., Han, B., Zheng, T., Xu, Y. 2018. Early crustal

359   evolution of the Yangtze Craton, South China: New constraints from zircon U–Pb–Hf

360   isotopes and geochemistry of ca. 2.9–2.6 Ga granitic rocks in the Zhongxiang Complex.

361   Precambrian Research, 314, 325–352.

362   Wang, Z., Deng, Q., Duan, T., Yang, F., Du, Q., Xiong, X., Liu, H., Cao, B. 2018. 2.85 Ga

363   and 2.73 Ga A-type granites and 2.75 Ga trondhjemite from the Zhongxiang Terrain:

364   Implications for early crustal evolution of the Yangtze Craton, South China. Gondwana

365   Research, 61, 1–19.

366   Wu, P., Zhang, S. B., Zheng, Y. F., Fu, B., Liang, T. 2019. Amalgamation of South China

367   into Rodinia during the Grenvillian accretionary orogeny: Geochemical evidence from

368   Early Neoproterozoic igneous rocks in the northern margin of the South China Block.

369   Precambrian Research, 321, 221–243.

370   Wu, Y., Gao, S., Zhang, H., Zheng, J., Liu, X., Wang, H., Gong, H., Zhou, LO., Yuan, H.

371   2012. Geochemistry and zircon U–Pb geochronology of Paleoproterozoic arc related

372   granitoid in the Northwestern Yangtze Block and its geological implications.

373   Precambrian Research, 200, 26–37.

374   Zhang, S. B., Zheng, Y. F., Wu, Y. B., Zhao, Z. F., Gao, S., Wu, F. Y. 2006. Zircon U–Pb

375   age and Hf–O isotope evidence for Paleoproterozoic metamorphic event in South

376   China. Precambrian Research, 151, 265–288.

377   Zhou, G., Wu, Y., Wang, H., Qin, Z., Zhang, W., Zheng, J., Yang, S. 2017. Petrogenesis of

378   the Huashanguan A-type granite complex and its implications for the early evolution of

379   the Yangtze Block. Precambrian Research, 292, 57–74.

380

381   *Jiangnan Orogenic Belt*

382   Huang, S. F., Wang, W., Pandit, M. K., Zhao, J. H., Lu, G. M., Xue, E. K. 2019.

383   Neoproterozoic S-type granites in the western Jiangnan Orogenic Belt, South China:

384   Implications for petrogenesis and geodynamic significance. Lithos, 342–343, 45–58.

385   Li, X. H., Li, W. X., Li, Z. X., Lo, C. H., Wang, J., Ye, M. F., Yang, Y. H. 2009.

386   Amalgamation between the Yangtze and Cathaysia Blocks in South China: constraints

387   from SHRIMP U–Pb zircon ages, geochemistry and Nd–Hf isotopes of the Shuangxiwu

388   volcanic rocks. Precambrian Research, 174, 117–128.

389   Lu, K., Li, L., Lin, S., Ren, S., Feng, L., Han, X., Ge, Y., Jiang, J., Wang, L., Wang, B. 2020.

390   Geochronological and geochemical data of paragneiss and amphibolite from the

391   Chencai Group in South China: Implications for petrogenesis and tectonic significance.

392   Geological Journal, 55, 6823–6840.

393 Peng, T., Fan, W., Zhao, G., Peng, B., Xia, X., Mao, Y. 2015. Petrogenesis of the early

394   Paleozoic strongly peraluminous granites in the Western South China Block and its

395   tectonic implications. Journal of Asian Earth Sciences, 98, 399–420.

396 Shu, L., Wang, J., Yao, J. 2019. Tectonic evolution of the eastern Jiangnan region, South

397   China: New findings and implications on the assembly of the Rodinia supercontinent.

398   Precambrian Research, 322, 42–65.

399 Wan, L., Zeng, Z., Asimow, P. D., Zeng, Z., Peng, L., Xu, D., Wei, Y., Liu, W., Lu, C.,

400   Chang, W. 2019. Mid-Neoproterozoic mafic rocks in the western Jiangnan orogen,

401   South China: Intracontinental rifting or subduction? Journal of Asian Earth Sciences,

402   185, 104039.

403 Wang, X. S., Gao, J., Klemd, R., Jiang, T., Zhai, Q. G., Li, J. L., Liang, X. Q. 2019. From arc

404   accretion to continental collision in the eastern Jiangnan Orogen: Evidence from two

405   phases of S-type granites. Precambrian Research, 321, 199–211.

406 Yin, C., Lin, S., Davis, D. W., Xing, G., Davis, W. J., Cheng, G., Xiao, W., Li, L. 2013.

407   Tectonic evolution of the southeastern margin of the Yangtze Block: Constraints from

408   SHRIMP U–Pb and LA-ICP-MS Hf isotopic studies of zircon from the eastern

409   Jiangnan Orogenic Belt and implications for the tectonic interpretation of South

410   China. Precambrian Research, 236, 145–156.

411 Yu, P., Zheng, Y., Zhou, Y., Chen, B., Niu, J., Yang, W. 2018. Zircon U−Pb geochronology

412   and geochemistry of the metabasite and gabbro: Implications for the Neoproterozoic

413   and Paleozoic tectonic settings of the Qinzhou Bay-Hangzhou Bay suture zone, South

414   China. Geological Journal, 53, 2219–2239.

415 Zhang, Y., Wang, Y. 2020. Early Neoproterozoic continental arc system at the central

416   Jiangnan Orogen, South China: Geochronological and geochemical constraints on the

417   key igneous rock-association. Geological Society of America Bulletin, 132, 638–654.

418

419 *Cathaysia Block*

420 Huang, D. L., Wang, X. L., Xia, X. P., Zhang, F. F., Wang, D., Sun, Z. M., Li, J. Y., Yang,

421   Q., Du, D. H., Chen, X. 2020. Crustal anatexis recorded by zircon grains from early

422   Paleozoic granitic rocks in Southeast China. Lithos, 370–371, 105598.

423 Hui, B., Dong, Y., Neubauer, F., He, S., Varga, J. 2020. Detrital zircon U–Pb ages of

424   metasedimentary rocks from the Neoproterozoic Zhoutan Group in the northern

425   Cathaysia Block (South China): Provenance and tectonic implications. International

426   Geology Review, 1–21.

427 Li, Z. X., Li, X. H., Wartho, J. A., Clark, C., Li, W. X., Zhang, C. L., Bao, C. 2010.

428   Magmatic and metamorphic events during the early Paleozoic Wuyi-Yunkai orogeny,

429   southeastern South China: New age constraints and pressure-temperature conditions.

430   Geological Society of America Bulletin, 122, 772–793.

431 Liu, Q., Yu, J. H., O'Reilly, S. Y., Zhou, M. F., Griffin, W. L., Wang, L., Cui, X. 2014.

432   Origin and geological significance of Paleoproterozoic granites in the northeastern

433   Cathaysia Block, South China. Precambrian Research, 248, 72–95.

434 Liu, R., Zhou, H. W., Zhang, L., Zhong, Z. Q., Zeng, W., Xiang, H., Jin, S., Lu, X. Q., Li, C.

435   Z. 2009. Paleoproterozoic reworking of ancient crust in the Cathaysia Block, South

436   China: Evidence from zircon trace elements, U–Pb and Lu–Hf isotopes. Chinese

437   Science Bulletin, 54, 1543–1554.

438   Shu, L. S., Faure, M., Yu, J. H., Jahn, B. M. 2011. Geochronological and geochemical

439   features of the Cathaysia block (South China): new evidence for the Neoproterozoic

440   breakup of Rodinia. Precambrian Research, 187, 263–276.

441   Shu, L. S., Jahn, B. M., Charvet, J., Santosh, M., Wang, B., Xu, X. S., Jiang, S. Y. 2014.

442   Early Paleozoic depositional environment and intraplate tectono-magmatism in the

443   Cathaysia Block (South China): evidence from stratigraphic, structural, geochemical

444   and geochronological investigations. American Journal of Science, 314, 154–186.

445   Wang, D., Zheng, J., Ma, Q., Griffin, W. L., Zhao, H., Wong, J. 2013. Early Paleozoic crustal

446   anatexis in the intraplate Wuyi–Yunkai orogen, South China. Lithos, 175–176, 124–

447   145.

448   Wang, Y., Zhang, A., Fan, W., Zhao, G., Zhang, G., Zhang, Y., Zhang, F., Li, S. 2011.

449   Kwangsian crustal anatexis within the eastern South China Block: geochemical, zircon

450   U–Pb geochronological and Hf isotopic fingerprints from the gneissoid granites of

451   Wugong and Wuyi–Yunkai Domains. Lithos, 127, 239–260.

452   Yang, D. S., Li, X. H., Li, W. X., Liang, X. Q., Long, W. G., Xiong, X. L. 2010. U–Pb and

453         $^{40}Ar–^{39}Ar$ geochronology of the Baiyunshan gneiss (central Guangdong, south China):

454   constraints on the timing of early Palaeozoic and Mesozoic tectonothermal events in the

455   Wuyun (Wuyi-Yunkai) Orogen. Geological magazine, 147, 481–496.

456   Yao, J., Shu, L., Cawood, P. A., Li, J. 2017. Constraining timing and tectonic implications of

457   Neoproterozoic metamorphic event in the Cathaysia Block, South China. Precambrian

458   Research, 293, 1–12.

459   Yu, J. H., O'Reilly, S. Y., Zhou, M. F., Griffin, W. L., Wang, L. 2012. U–Pb geochronology

460   and Hf–Nd isotopic geochemistry of the Badu Complex, Southeastern China:

461   implications for the Precambrian crustal evolution and paleogeography of the Cathaysia

462   Block. Precambrian Research, 222–223, 424–449.

463   Yu, J. H., Wang, L., O'reilly, S. Y., Griffin, W. L., Zhang, M., Li, C., Shu, L. 2009. A

464   Paleoproterozoic orogeny recorded in a long-lived cratonic remnant (Wuyishan

465   terrane), eastern Cathaysia Block, China. Precambrian Research, 174, 347–363.

466   Zhao, L., Zhai, M., Santosh, M., Zhou, X. 2017. Early Mesozoic retrograded eclogite and

467   mafic granulite from the Badu Complex of the Cathaysia Block, South China:

468   Petrology and tectonic implications. Gondwana Research, 42, 84–103.

469   Zhao, L., Zhang, R. C., Zhai, M. G., Zhou, X. W. 2020. Major lithologies of the high-grade

470   Zhoutan terrane within the Cathaysia Block and their tectonic implications for the

471   Neoproterozoic-Paleozoic South China. Lithos, 372–373, 105664.

472   Zhao, L., Zhou, X., Zhai, M., Santosh, M., Geng, Y. 2015. Zircon U–Th–Pb–Hf isotopes of

473   the basement rocks in northeastern Cathaysia block, South China: Implications for

474   Phanerozoic multiple metamorphic reworking of a Paleoproterozoic terrane. Gondwana

475   Research, 28, 246–261.

476

477

478   **Sulu–Dabie Collision Belt**

479   Lei, H., Xu, H., Xiang, H. 2020. Basement evolution of the Sulu orogenic belt: Constraints

480   on zircon U–Pb ages and trace elements from the Weihai gneisses. Geological Journal,

481   55, 2646–2661.

482   Liu, F. L., Liou, J. G. 2011. Zircon as the best mineral for P–T–time history of UHP

483   metamorphism: A review on mineral inclusions and U–Pb SHRIMP ages of zircons

484   from the Dabie–Sulu UHP rocks. Journal of Asian Earth Sciences, 40, 1–39.

485   Liu, F., Robinson, P. T., Gerdes, A., Xue, H., Liu, P., Liou, J. G. 2010. Zircon U–Pb ages,

486   REE concentrations and Hf isotope compositions of granitic leucosome and pegmatite

487   from the north Sulu UHP terrane in China: constraints on the timing and nature of

488   partial melting. Lithos, 117, 247–268.

489   Liu, L., Liu, F., Liu, P., Wang, W., Ji, L., Wang, F., Cai, J. 2018. Petrology, geochemistry

490   and geochronology of the meta-mafic rocks in the North Sulu ultrahigh-pressure belt:

491   Implications for their petrogenetic diversity and complex tectonic evolution.

492   Precambrian Research, 316, 127–154.

493   Wang, S. J., Wang, L., Brown, M., Johnson, T. E., Piccoli, P. M., Feng, P., Wang, Z. L. 2020.

494   Petrogenesis of leucosome sheets in migmatitic UHP eclogites—Evolution from

495   silicate-rich supercritical fluid to hydrous melt. Lithos, 36–361, 105442.

496   Zheng, Y. F., Zhao, Z. F., Wu, Y. B., Zhang, S. B., Liu, X., Wu, F. Y. 2006. Zircon U–Pb

497   age, Hf and O isotope constraints on protolith origin of ultrahigh-pressure eclogite and

498   gneiss in the Dabie orogen. Chemical Geology, 231, 135–158.

499   Zhou, K., Chen, Y. X., Zhang, S. B., Zheng, Y. F. 2020. Zircon evidence for the Eoarchean

500   (~ 3.7 Ga) crustal remnant in the Sulu Orogen, eastern China. Precambrian Research,

501   337, 105529.

502

503

504   **Korean Peninsula**

505   *Gyeonggi massif*

506   Cheong, A. C. S., Jo, H. J., Jeong, Y. J., Li, X. H. 2019. Magmatic response to the interplay

507   of collisional and accretionary orogenies in the Korean Peninsula: Geochronological,

508   geochemical, and O-Hf isotopic perspectives from Triassic plutons. Geological Society

509   of America Bulletin, 131, 609–634.

510   Cho, D. L. 2014. SHRIMP U–Pb zircon geochronology of the Guryong Group in Odesan

511   area, east Gyeonggi Massif, Korea: A new identification of Late Paleozoic strata and its

512   tectonic implication. The Journal of the Petrological Society of Korea, 23, 197–208 (in

513   Korean with English abstract).

514   Cho, M., Kim, H., Lee, Y., Horie, K., Hidaka, H. 2008. The oldest (ca. 2.51 Ga) rock in

515   South Korea: U–Pb zircon age of a tonalitic migmatite, Daeijak Island, western

516   Gyeonggi massif. Geosciences Journal, 12, 1–6.

517   Choi, S. G., Rajesh, V. J., Seo, J., Park, J. W., Oh, C. W., Pak, S. J., Kim, S. W. 2009.

518   Petrology, geochronology and tectonic implications of Mesozoic high Ba–Sr granites in

519   the Haemi area, Hongseong Belt, South Korea. Island Arc, 18, 266–281.

520   Horie, K., Tsutsumi, Y., Kim, H., Cho, M., Hidaka, H., Terada, K. 2009. A U–Pb

521   geochronological study of migmatitic gneiss in the Busan gneiss complex, Gyeonggi

522   massif, Korea. Geosciences Journal, 13, 205–215.

523   Kim, S. W., Kee, W. S., Lee, S. R., Santosh, M., Kwon, S. 2013. Neoproterozoic plutonic

524   rocks from the western Gyeonggi massif, South Korea: implications for the

525   amalgamation and break-up of the Rodinia supercontinent. Precambrian Research, 227,

526   349–367.

527   Kim, S. W., Kwon, S., Koh, H. J., Yi, K., Jeong, Y. J., Santosh, M. 2011. Geotectonic

528   framework of Permo–Triassic magmatism within the Korean Peninsula. Gondwana

529   Research, 20, 865–889.

530   Kim, S. W., Kwon, S., Santosh, M., Williams, I. S., Yi, K. 2011. A Paleozoic subduction

531   complex in Korea: SHRIMP zircon U–Pb ages and tectonic implications. Gondwana

532   Research, 20, 890–903.

533   Kim, S. W., Oh, C. W., Williams, I. S., Rubatto, D., Ryu, I. C., Rajesh, V. J., Kim, C. B.,

534   Guo, L., Zhai, M. 2006. Phanerozoic high-pressure eclogite and intermediate-pressure

535   granulite facies metamorphism in the Gyeonggi Massif, South Korea: implications for

536   the eastward extension of the Dabie–Sulu continental collision zone. Lithos, 92, 357–

537   377.

538   Kim, S. W., Santosh, M., Park, N., Kwon, S. 2011. Forearc serpentinite mélange from the

539   Hongseong suture, South Korea. Gondwana Research, 20, 852–864.

540   Kim, S. W., Williams, I. S., Kwon, S., Oh, C. W. 2008. SHRIMP zircon geochronology, and

541   geochemical characteristics of metaplutonic rocks from the south-western Gyeonggi

542   Block, Korea: implications for Paleoproterozoic to Mesozoic tectonic links between the

543   Korean Peninsula and eastern China. Precambrian Research, 162, 475–497.

544   Lee, B. C., Oh, C. W., Kim, T. S., Yi, K. 2016. The metamorphic evolution from ultrahigh-

545   temperature to amphibolite facies metamorphism in the Odaesan area after the collision

546   between the North and South China Cratons in the Korean Peninsula. Lithos, 256–257,

547   109–131.

548   Lee, B. C., Oh, C. W., Yengkhom, K. S., Yi, K. 2014. Paleoproterozoic magmatic and

549   metamorphic events in the Hongcheon area, southern margin of the Northern Gyeonggi

550   Massif in the Korean Peninsula, and their links to the Paleoproterozoic orogeny in the

551   North China Craton. Precambrian Research, 248, 17–38.

552   Lee, B. Y., Oh, C. W., Lee, S. H., Seo, J., Yi, K. 2020. Ages and tectonic settings of the

553   Neoproterozoic igneous rocks in the Gyeonggi Massif of the southern Korean

554   Peninsula and the correlation with the Neoproterozoic igneous rocks in China. Lithos,

555   370–371, 105625.

556   Lee, S. R., Cho, M., Cheong, C. S., Kim, H., Wingate, M. T. D. 2003. Age, geochemistry,

557   and tectonic significance of Neoproterozoic alkaline granitoids in the northwestern

558   margin of the Gyeonggi massif, South Korea. Precambrian Research, 122, 297–310.

559   Lee, S. R., Cho, M., Yi, K., Stern, R. A. 2000. Early Proterozoic granulites in central Korea:

560   tectonic correlation with Chinese cratons. The Journal of Geology, 108, 729–738.

561   Oh, C. W., Imayama, T., Jeon, J., Yi, K. 2017. Regional Middle Paleozoic metamorphism in

562   the southwestern Gyeonggi Massif, South Korea: its implications for tectonics in

563   Northeast Asia. Journal of Asian Earth Sciences, 145, 542–564.

564   Oh, C. W., Imayama, T., Lee, S. Y., Yi, S. B., Yi, K., Lee, B. C. 2015. Permo-Triassic and

565   Paleoproterozoic metamorphism related to continental collision in Yangpyeong, South

566   Korea. Lithos, 216–217, 264–284.

567   Oh, C. W., Kim, S. W., Williams, I. S. 2006. Spinel granulite in Odesan area, South Korea:

568   Tectonic implications for the collision between the North and South China blocks.

569   Lithos, 92, 557–575.

570   Oh, C. W., Lee, J. Y., Yengkhom, K. S., Lee, B. C., Ryu, H. I. 2018. Neoproterozoic igneous

571   activity and Permo-Triassic metamorphism inthe Gapyeong area within the Gyeonggi

572   Massif, South Korea, and theirimplication for the tectonics of northeastern

573   Asia. Lithos, 322, 1–19.

574   Park, S. I., Kim, S. W., Kwon, S., Thanh, N. X., Yi, K., Santosh, M. 2014. Paleozoic

575   tectonics of the southwestern Gyeonggi massif, South Korea: Insights from

576   geochemistry, chromian-spinel chemistry and SHRIMP U–Pb geochronology.

577   Gondwana Research, 26, 684–698.

578   Seo, J., Choi, S. G., Oh, C. W. 2010. Petrology, geochemistry, and geochronology of the

579   post-collisional Triassic mangerite and syenite in the Gwangcheon area, Hongseong

580   Belt, South Korea. Gondwana Research, 18, 479–496.

581   Song, Y. S., Park, K. H., Seo, J. H., Jo, H. J., Yi, K. W. 2011. SHRIMP zircon ages of the

582   basement gneiss complex in the Pyeongchang-Wonju area, Gyeonggi Massif, Korea.

583   The Journal of the Petrological Society of Korea, 20, 99–114 (in Korean with English

584   abstract).

585 Williams, I. S., Cho, D. L., Kim, S. W. 2009. Geochronology, and geochemical and Nd–Sr

586 isotopic characteristics, of Triassic plutonic rocks in the Gyeonggi Massif, South

587 Korea: constraints on Triassic post-collisional magmatism. Lithos, 107, 239–256.

588 Yengkhom, K. S., Lee, B. C., Oh, C. W., Yi, K., Kang, J. H. 2014. Tectonic and deformation

589 history of the Gyeonggi Massif in and around the Hongcheon area, and its implications

590 in the tectonic evolution of the North China Craton. Precambrian Research, 240, 37–59.

591 Yi, S. B., Oh, C. W., Lee, S. Y., Choi, S. G., Kim, T., Yi, K. 2016. Triassic mafic and

592 intermediate magmatism associated with continental collision between the North and

593 South China Cratons in the Korean Peninsula. Lithos, 246–247, 149–164.

594 Zhai, M., Ni, Z., Oh, C. W., Guo, J., Choi, S. G. 2005. SHRIMP zircon age of a Proterozoic

595 rapakivi granite batholith in the Gyeonggi massif (South Korea) and its geological

596 implications. Geological Magazine, 142, 23–30.

597

598 *Yeongnam massif*

599 Cheong, A. C. S., Jo, H. J., Jeong, Y. J., Li, X. H. 2019. Magmatic response to the interplay

600 of collisional and accretionary orogenies in the Korean Peninsula: Geochronological,

601 geochemical, and O-Hf isotopic perspectives from Triassic plutons. Geological Society

602 of America Bulletin, 131, 609–634.

603 Cho, D. L., Lee, B. C., Oh, C. W. 2020. Petrogenesis of paleoproterozoic (2.02–1.96 Ga)

604 metagranitoids in the southwestern Yeongnam Massif, Korean Peninsula, and their

605 significance for the tectonic history of northeast Asia: Insights from zircon U–Pb–Hf

606 isotope and whole-rock geochemical compositions. Precambrian Research, 340,

607 105631.

608   Kim, N., Cheong, C. S., Park, K. H., Kim, J., Song, Y. S. 2012. Crustal evolution of

609   northeastern Yeongnam Massif, Korea, revealed by SHRIMP U–Pb zircon

610   geochronology and geochemistry. Gondwana Research, 21, 865–875.

611   Kim, N., Cheong, C. S., Yi, K., Song, Y. S., Park, K. H., Geng, J. Z., Li, H. K. 2014. Zircon

612   U–Pb geochronological and Hf isotopic constraints on the Precambrian crustal

613   evolution of the north-eastern Yeongnam Massif, Korea. Precambrian Research,

614   242, 1–21.

615   Kim, S. W., Kwon, S., Koh, H. J., Yi, K., Jeong, Y. J., Santosh, M. 2011a. Geotectonic

616   framework of Permo–Triassic magmatism within the Korean Peninsula. Gondwana

617   Research, 20, 865–889.

618   Lee, B. C., Oh, C. W., Cho, D. L., Yi, K. 2019. Paleoproterozoic (2.0–1.97 Ga) subduction-

619   related magmatism on the north–central margin of the Yeongnam Massif, Korean

620   Peninsula, and its tectonic implications for reconstruction of the Columbia

621   supercontinent. Gondwana Research, 72, 34–53.

622   Lee, B. C., Oh, C. W., Wang, X. 2020. Paleoproterozoic (ca. 1.87–1.69 Ga) arc-related

623   tectonothermal events on northcentral Yeongnam Massif, South Korea and its

624   tectonic implications: Insights from metamorphism, geochemistry and

625   geochronology. Precambrian Research, 338, 105562.

626   Lee, B. C., Park, J. H., Oh, C. W., Yi, K. 2017. Metamorphic and magmatic evolution of the

627   Paleoproterozoic gneisses in the Sancheong area, Yeongnam Massif, South Korea,

628   and their implications to the tectonics in the Northeast Asia. Precambrian Research,

629   298, 439–461.

630   Lee, Y., Cho, M. 2020. Fluid-present partial melting of Paleoproterozoic Okbang amphibolite

631   in the Yeongnam Massif, Korea. Lithosphere, 2020, 1–26.

632 Lee, Y., Cho, M., Cheong, W., Yi, K. 2014. A massif-type (~ 1.86 Ga) anorthosite complex

633   in the Yeongnam Massif, Korea: late-orogenic emplacement associated with the

634   mantle delamination in the North China Craton. Terra Nova, 26, 408−416.

635 Lee, Y., Cho, M., Cheong, W., Yi, K. 2018. Prolonged high-temperature, low-pressure

636   metamorphism associated with~ 1.86 Ga Sancheong–Hadong anorthosite in the

637   Yeongnam Massif, Korea: Paleoproterozoic hot orogenesis in the North China

638   Craton. Precambrian Research, 307, 175–200.

639 Lee, Y., Cho, M., Yi, K. 2017. In situ U–Pb and Lu–Hf isotopic studies of zircons from the

640   Sancheong–Hadong AMCG suite, Yeongnam Massif, Korea: Implications for the

641   petrogenesis of ~1.86 Ga massif-type anorthosite. Journal of Asian Earth Sciences,

642   138, 629–646.

643 Oh, C., Lee, B., Lee, S., Kim, M., Lee, B., Choi, S. 2016. The tectonic evolution and

644   important geoheritages in the Jinan and Muju area, Jeollabuk-do. Journal of the

645   Geological society of Korea, 52, 709–738 (in Korean with English abstract).

646 Oh, C. W., Lee, B. C., Yi, K. 2013. The origin and age of the orbicular granite gneiss in

647   Wangjungri, Muju. The Journal of the Petrological Society of Korea, 22, 117–135

648   (in Korean with English abstract).

649 Song, Y. S., Lee, H. S., Park, K. H., Fitzsimons, I. C. W., Cawood, P. A. 2015. Recognition

650   of the Phanerozoic "Young granite gneiss" in the central Yeongnam massif.

651   Geosciences Journal, 19, 1–16.

652

653

654

655 **Figure 8**

656

657 Cho, D. L., Lee, T. H., Takahashi, Y., Kato, T., Yi, K., Lee, S., Cheong, A. C. S. 2021.

658   Zircon U–Pb geochronology and Hf isotope geochemistry of magmatic and

659   metamorphic rocks from the Hida Belt, southwest Japan. Geoscience Frontiers, 12,

660   101145.

661 Horie, K., Takehara, M., Suda, Y., Hidaka, H. 2013. Potential Mesozoic reference zircon

662   from the Unazuki plutonic complex: geochronological and geochemical

663   characterization. Island Arc, 22, 292–305.

664 Horie, K., Tsutsumi, Y., Takehara, M., Hidaka, H. 2018. Timing and duration of regional

665   metamorphism in the Kagasawa and Unazuki areas, Hida metamorphic complex,

666   southwest Japan. Chemical Geology, 484, 148–167.

667 Horie, K., Yamashita, M., Hayasaka, Y., Katoh, Y., Tsutsumi, Y., Katsube, A., Hidaka, H.,

668   Kim, H., Cho, M. 2010. Eoarchean–Paleoproterozoic zircon inheritance in Japanese

669   Permo-Triassic granites (Unazuki area, Hida Metamorphic Complex): Unearthing more

670   old crust and identifying source terrranes. Precambrian Research, 183, 145–157.

671 Koizumi, S., Otoh, S. 2020. The Permian–Triassic plutonic and metamorphic rocks in the

672   Saragawa–Bandojima area, Katsuyama City, Fukui Prefecture, central Japan.

673   Katsuyama City Geopark Academic Research Encouragement Project Academic

674   Research Report, pp18 (in Japanese with English abstract).

675 Sakoda, M., Kano, T., Fanning, C. M., Sakaguchi, T. 2006. SHRIMP U−Pb zircon age of the

676   Inishi migmatite around the Kamioka mining area, Hida metamorphic complex, Central

677   Japan. Resource Geology, 56, 17−26.

678 Takahashi, Y., Cho, D. L., Kee, W. S. 2010. Timing of mylonitization in the Funatsu shear

679   zone within Hida Belt of southwest Japan: Implications for correlation with the shear

680   zones around the Ogcheon Belt in the Korean Peninsula. Gondwana Research, 17, 102–

681   115.

682   Takahashi, Y., Cho, D. L., Mao, J., Zhao, X., Yi, K. 2018. SHRIMP U–Pb zircon ages of the

683   Hida metamorphic and plutonic rocks, Japan: Implications for late Paleozoic to

684   Mesozoic tectonics around the Korean Peninsula. Island Arc, 27, e12220.

685   Takehara, M., Horie, K. 2019. U–Pb zircon geochronology of the Hida gneiss and granites in

686   the Kamioka area, Hida Belt. Island Arc, 28, e12303.

687   Yamada, R., Sawada, H., Aoyama, S., Ouchi, W., Niki, S., Nagata, M., Takahashi, T., Hirata,

688   T. 2021. Zircon U-Pb ages and whole–rock geochemistry from the Hida granites:

689   implications for the geotectonic history and the origin of Mesozoic granites in the Hida

690   belt, Japan. Journal of Mineralogical and Petrological Sciences, 116, 61–66.

691   Zhao, X., Mao, J., Ye, H., Liu, K., Takahashi, Y. 2013. New SHRIMP U–Pb zircon ages of

692   granitic rocks in the Hida Belt, Japan: Implications for tectonic correlation with

693   Jiamushi massif. Island Arc, 22, 508–521.

694